

Collective behavior of asperities before large stick-slip events

Weiwei Shu¹, Olivier Lengliné², and Jean Schmittbuhl³

¹EOST/ITES, Université de Strasbourg/CNRS

²Université de Strasbourg, IPGS, CNRS

³CNRS/Université de Strasbourg

March 13, 2023

Abstract

The multi-scale roughness of a fault interface is responsible for multiple asperities that establish a complex and discrete set of real contacts. Since asperities control the initiation and evolution of the fault slip, it is important to explore the intrinsic relationships between the collective behavior of local asperities and the frictional stability of the global fault. Here we propose a novel analog experimental approach, which allows us to capture the temporal evolution of the slip of each asperity on a faulting interface. We find that many destabilizing events at the local asperity scale occurred in the frictional strengthening stage which is conventionally considered as the stable regime of a fault. We compute the interseismic coupling to evaluate the slipping behaviors of asperities during the fault-strengthening stage. We evidence that the interseismic coupling can be affected by the elastic interactions between asperities through the embedding soft matrix. Scaling laws of natural slow slip events are reproduced by our setup in particular the moment-duration scaling. We also evidence an unexpected persistency of a disordering of the asperities through the seismic cycles despite the relaxation effects of the large slip events.

Collective behavior of asperities before large stick-slip events

Weiwei Shu¹, Olivier Lengliné¹, Jean Schmittbuhl¹

¹EOST/ITES, Université de Strasbourg/CNRS, France

Key Points:

- We propose a novel direct-shear setup to observe the collective behavior of asperities along an analog fault interface during stick-slips
- Scaling laws, that mimic those of slow slip events, are observed in our experiments and originate during the fault-strengthening phase
- Large scale quenched topography of the asperities along the interface has a direct impact on the interseismic coupling

Corresponding author: Weiwei Shu, w.shu@unistra.fr

Abstract

The multi-scale roughness of a fault interface is responsible for multiple asperities that establish a complex and discrete set of real contacts. Since asperities control the initiation and evolution of the fault slip, it is important to explore the intrinsic relationships between the collective behavior of local asperities and the frictional stability of the global fault. Here we propose a novel analog experimental approach, which allows us to capture the temporal evolution of the slip of each asperity on a faulting interface. We find that many destabilizing events at the local asperity scale occurred in the frictional strengthening stage which is conventionally considered as the stable regime of a fault. We compute the interseismic coupling to evaluate the slipping behaviors of asperities during the fault-strengthening stage. We evidence that the interseismic coupling can be affected by the elastic interactions between asperities through the embedding soft matrix. Scaling laws of natural slow slip events are reproduced by our setup in particular the moment-duration scaling. We also evidence an unexpected persistency of a disordering of the asperities through the seismic cycles despite the relaxation effects of the large slip events.

Plain Language Summary

Earthquakes are the results of a slip along a rough fault on which a complex and discrete set of asperities establish the interfacial contacts and control the frictional stability of the fault. We propose a novel experimental setup capable of measuring directly the subtle motion of individual asperities on an analog faulting interface. By capturing the temporal evolution of the slip of each asperity, we link the mechanical behavior of the global fault with the collective behavior of local asperities. Many destabilizing events at the local asperity scale are found during the globally stable stage of the fault. We prove that the interseismic coupling of asperities is affected by the normal load, the peak height of asperities, and the interactions between asperities. The spatiotemporal interactions of asperities are quantified as slip episodes to mimic the ruptures including both stable and unstable slips. With the catalog of slip episodes, we reproduce the significant characteristics and scaling laws observed in natural faults, such as the magnitude-frequency distribution and the moment-duration scaling. Such upscaling suggests that our results can be extrapolated to natural faults and provide insights into fault physics and mechanics.

1 Introduction

Crustal fault interfaces display geological heterogeneities at various scales (Faulkner et al., 2003; Chester et al., 1993; Ben-Zion & Sammis, 2003). In particular, exhumed fault surfaces exhibit a complex topography characterized by height variations at all scales (Candela et al., 2009, 2012; Power et al., 1987; Schmittbuhl et al., 1993, 1995; Scholz, 2019). Supposing that the roughness of these interfaces is similar to those of active faults at depth, it implies that the frictional interface is formed by a complex set of junctions across the two opposite surfaces in contact (Schmittbuhl et al., 2006; Pohrt & Popov, 2012). These junctions are commonly known as asperities (Bhushan, 1998). They have been characterized at the laboratory scale as microcontacts (Dieterich & Kilgore, 1994) where the resistance to an imposed shear stress is shown to be governed by the initiation and evolution of the fault slip (Scholz, 2019).

The presence of these asperities on the fault is supported by the observation of small repeating earthquakes, supposedly representing cohesive zones that fail periodically under constant loading (Nadeau & Johnson, 1998). The role of such asperities in the behavior of earthquakes has long been recognized. For example, it is suggested that small and scattered asperities on a subduction interface may lead only to a minor release of the seismic moment (Ruff & Kanamori, 1983). On the other hand, a great earthquake may involve the simultaneous rupture of multiple asperities, such as the 1960 M_W 9.5 Chile earthquake (Moreno et al., 2009) or the 2004 M_W 9.2 Sumatra-Andaman earthquake (Subarya et al., 2006). Such examples have been interpreted in a framework drawing a strong link between the rupture synchronization of asperities and the magnitude of the impending earthquake (Lay & Kanamori, 1981; Lay et al., 1982). This synchronization of asperities actually emphasizes a strong time-and-space dependent mechanism for the underlying physics and corresponding mechanical response of fault slip. The role of asperities on the behavior of the faulting interface is not limited to dynamic rupture events. Indeed, the interseismic phase is also strongly impacted by the presence of such strong contact areas. This notably arises as locked patches can create stress shadows which lead to reduced interseismic slip rates on the surroundings of the asperity (Bürgmann et al., 2005) and thus a spatial modulation of the interseismic coupling (Perfettini et al., 2010).

Numerical models have addressed the behavior of a fault interface comprising multiple asperities. A number of simulations represent the interface notably in the context of the rate-and-state friction framework (Dieterich, 1979; Ruina, 1983; Marone, 1998) and asperities are presented as distinct patches spatially distributed over the fault plane with distinct frictional parameters (Barbot et al., 2012; Dublanche et al., 2013; Luo & Ampuero, 2018; Li & Rubin, 2017). In these numerical models, the asperities are usually considered as velocity weakening patches and are therefore defined to be potentially unstable. These models indicate that the mechanical response of a fault is evidently affected by the interactions of discrete asperities surrounded by aseismic creep areas. For instance, a variable density of asperities (Dublanche et al., 2013), which is the ratio between the total area covered by asperities and the total area of the fault plane is proposed and utilized to explain at which condition the fault will be ruptured entirely or locally. Incorporating roughness on the fault plane (as fluctuations of the normal stress), Cattania and Segall (2021) show that this heterogeneity modulates the slip stability across the fault. Finally, Romanet et al. (2018) demonstrate that the sliding diversity of a fault can be obtained from geometrical complexities alone, without the need for the complexity of the friction law. All these numerical approaches, therefore, point to the importance of these asperities and their interactions in controlling fault mechanics. However, these models are severely limited by the computational cost of simulating heterogeneities with a variable size over a large time and space domain and inherently only describe a limited aspect of the ongoing physics.

At the laboratory scale, numerous experiments on rock samples have also shown that fault roughness plays a crucial role in fault slip behavior (Goebel et al., 2017; Harbord et al., 2017; Morad et al., 2022; Zhou et al., 2021) as it controls actual stress conditions at contacting asperities (Aubry et al., 2020). These results imply that the stress heterogeneity at local asperities is significant for influencing fault slip behavior. However, these experiments usually analyze the effects of asperities by comparing the initial and final roughness of the fault interface as the nontransparent rock slabs cannot provide the possibility to capture what is happening on the interface during the fault slip process. On the contrary, some other experiments take advantage of the transparency of analog materials (e.g., Poly-methyl-methacrylate, PMMA) to optically observe the asperities distributed on the interface (Lengliné et al., 2012; Jestin et al., 2019; Selvadurai & Glaser, 2015, 2017), which provides a possibility for the direct monitoring of the

107 faulting interface. Although the contacts were captured during these experiments, it was
 108 not possible to track the slip at each point during shearing.

109 Here we present a novel experimental setup that aims at capturing the slip as a func-
 110 tion of time for each asperity on a sheared interface. Our experimental setup is much
 111 simpler than a complex fault zone system, which has no mineralogy, no fluid, and no chem-
 112 ical transformation, but the fundamental process of interest, the relationship between
 113 the collective behavior of local asperities and the stability regime of the global fault sys-
 114 tem, remains similar. Specifically, this novel experimental approach allows a thick trans-
 115 parent PMMA plate to slide slowly on a customized surface with height variations, on
 116 which asperities are modeled by numerous identical spherical PMMA beads embedded
 117 in a softer polymer base. Thanks to a high-resolution camera, our setup is capable of
 118 measuring directly the subtle motion of local asperities on the interface during the whole
 119 slipping process, which helps to understand the time-and-space dependent behavior of
 120 each single asperity. The mechanical response of the global fault system is well recorded
 121 and explained through the collective behavior of local asperities. The link between the
 122 fault topography and the interseismic coupling is also investigated. In addition, the spatio-
 123 temporal interactions of asperities are quantified as collective slip episodes mimicking
 124 fault ruptures including both stable and unstable slips. To give some geophysical impli-
 125 cations, the effective upscaling from the analog interface to natural faults is demonstrated
 126 by reproducing significant characteristics and scaling-laws observed in natural fault sys-
 127 tems.

128 **2 Experimental Setup**

129 We build an analog model of a shear interface that aims at reproducing the typ-
 130 ical mechanical structure of a natural fault core. We consider that a fault zone consists
 131 of several key elements. At the interface, the roughness of the fault topography creates
 132 contacts on a number of discrete sites, i.e. asperities, that are here modeled as PMMA
 133 beads. The core of the fault, which consists generally in a heavily fractured medium (Chester
 134 & Chester, 1998; Schulz & Evans, 2000) is represented in our setup with a soft material
 135 surrounding the PMMA beads. At a greater distance from the fault, the number of dam-
 136 age decreases (Ben-Zion & Sammis, 2003; Mitchell & Faulkner, 2009; Stierman, 1984),
 137 and the fault becomes stiffer which translates in our setup in a rigid base attached to
 138 the soft material (Figure 1). The asperities are in contact with a top rigid block and es-

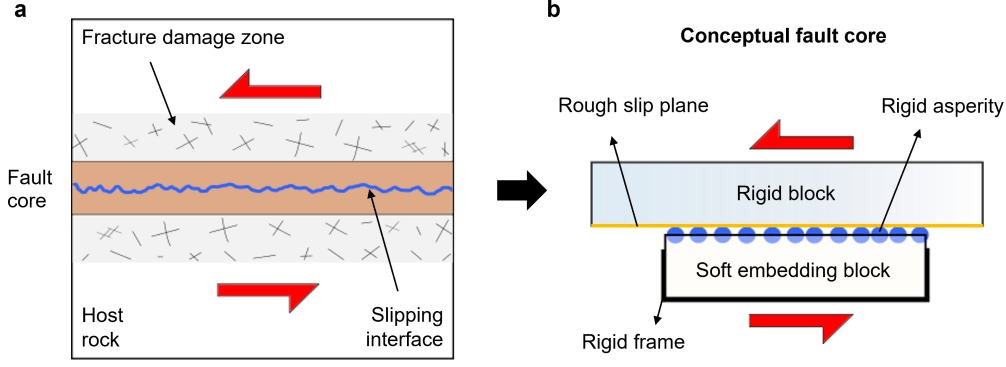


Figure 1. a: Sketch of a typical natural fault zone showing a rough frictional slipping interface subjected to shear. b: Conceptual model of the analog shear interface derived from the natural fault core structure. The rigid asperities embedded in the soft thick block establish a rough slip plane beneath the top rigid block.

establish a rough slip plane, while the soft embedding block fixed within the bottom rigid frame is easily deformed. This thick, rough, and deformable interface allows us to study the interactions of asperities and their collective behavior with respect to the frictional stability of the fault interface.

2.1 Sample Preparation and Characterization

To prepare such a model of multi-asperity contact, numerous identical spherical PMMA beads (a total number of 175) with a radius R of 3 mm are embedded in a soft block. The soft block is composed of silicone (BLUESIL RTV 3428 A&B product from the Elkem company), with dimensions $10 \times 10 \times 3.0$ cm. The preparation of the sample consists in first pouring a thin layer (of the thickness of a bead radius) of edible gelatin mixed with water at the bottom of a mold. Then PMMA beads are dropped randomly in this layer all over the interface. After the gelatin layer solidifies, we then pour the liquid silicon into the mold to cover the beads and wait for at least 24 hours at room temperature for its solidification. Finally, we take out the upside-down sample and remove the mixture of gelatin and water. Following the procedures above, we customize an experimental sample and its picture is displayed in Figure 2. The resulting sample is made such that all beads have nearly the same height while being scattered randomly over the sample. Physical characteristics of the silicone are derived from the technical datasheet,

the relation of Gent (1958) for converting durometer values to Young’s modulus, and laboratory measurements of the P-wave velocity of the material. We obtain a P-wave velocity for this material of 1000 m/s, an S-wave velocity of 19 m/s, a Young’s modulus of 1.1 MPa, and a density of 1100 kg/m³.

In order to precisely describe the so-formed interface and get the summit heights of all the beads, we measure a high-resolution topographical map for the interface. The data are acquired by a digital microscope profiler (RH-2000, HIROX) and a non-contact Nano Point Scanner (NPS, HIROX). The system uses a white light confocal LED beam with grids of 28 μm and 100 μm in the x - and y -directions, respectively. The topographical map of the interface is shown in Figure 3a, where the blueish part indicates the embedding silicone block while the discrete circles represent the asperities with different heights. We determine the peak heights of all the asperities (Figure 3b) and statistically analyze their distribution (Figure 3c). The peak heights of asperities (relative to the average silicone upper face level) range from 1.31 mm to 3.15 mm, with most of them within the peak height interval [1.4, 2.6]. The average peak height is 2.02 mm and the standard deviation of the peak heights is 0.39 mm, which indicates a small variance in the peak heights of asperities. We notice that there is a large-scale trend across the entire sample of this peak bead height. This is most likely due to the non-perfect planarity of the gelatin layer. Removing this large-scale trend, we observe that the height difference between neighboring asperities is low. In addition, we compute the average peak height difference between two asperities as a function of the distance in x and y direction (Figure 3d). We find a pattern highlighting the large scale variation of the peak height but no other correlation of the peak heights emerges.

2.2 Mechanical Loading

To simulate a large-scale, far-field, loading imposed on a fault, the shear of the whole analog interface system is induced by imposing a small displacement rate to the PMMA plate under well-controlled normal loads (Figure 2). PMMA has been widely used, as an analog material, to simulate numerous mechanical processes taking place within the Earth. In particular, frictional processes taking place on natural faults have been investigated using this material, such as fault creep and nucleation phases (e.g., McLaskey & Glaser, 2011; McLaskey et al., 2012; Selvadurai & Glaser, 2015) but also ruptures (e.g., Ben-David et al., 2010; Gvirtzman & Fineberg, 2021; Schmittbuhl & Måløy, 1997). Due

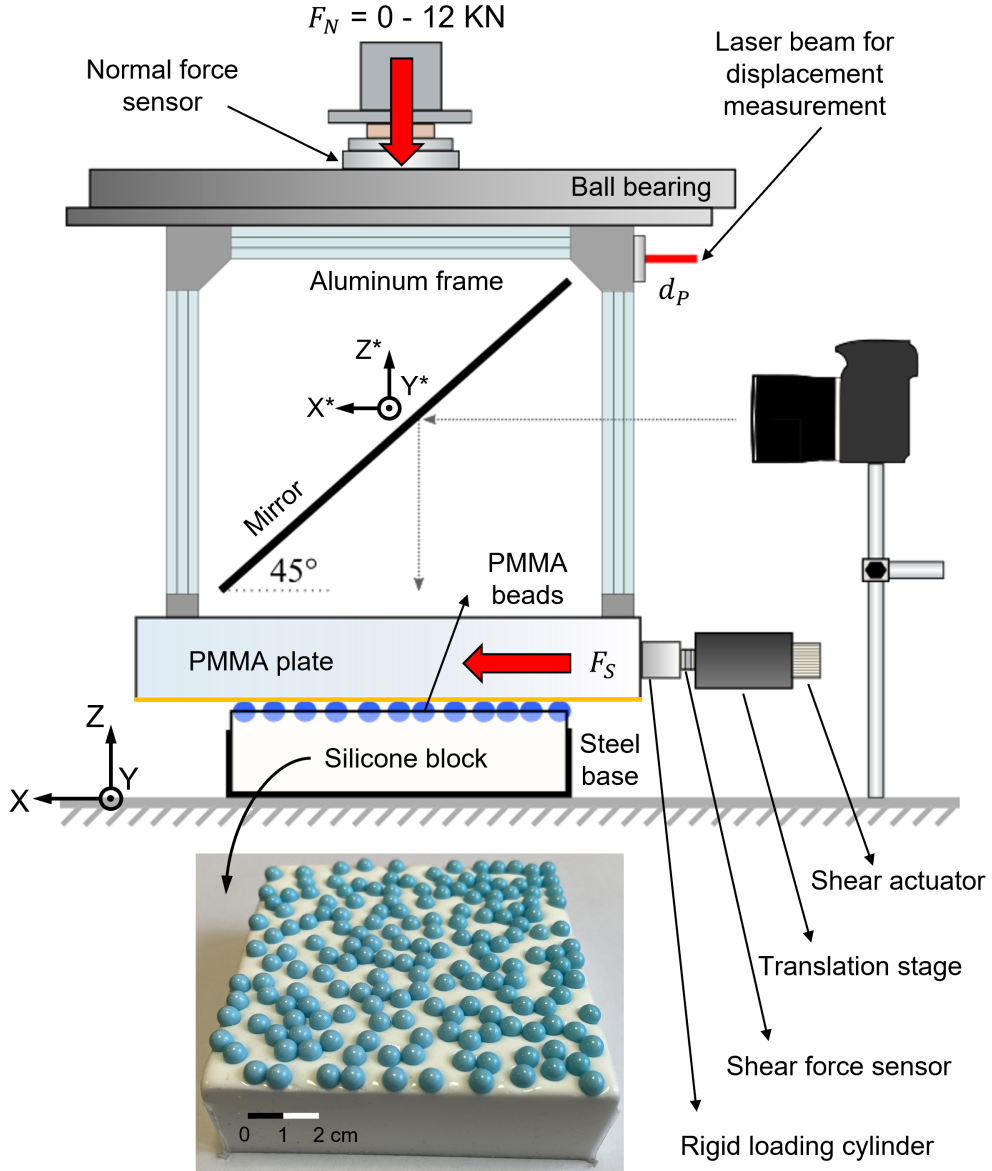


Figure 2. Schematic diagram of the technical experimental setup (side view). The normal force, F_N , and shear force, F_S , are measured by their corresponding sensors. A laser is employed to measure the displacement of the PMMA plate, d_P . A high-resolution camera is utilized with a mirror to monitor the positions of the PMMA beads during the whole shear process. Two axis systems, one attached to the ground and another one attached to the mirror, are represented. The yellow line indicates a rough slip plane established between the PMMA plate and the PMMA beads. The inset shows an image of the PMMA beads embedded in the soft silicone block.

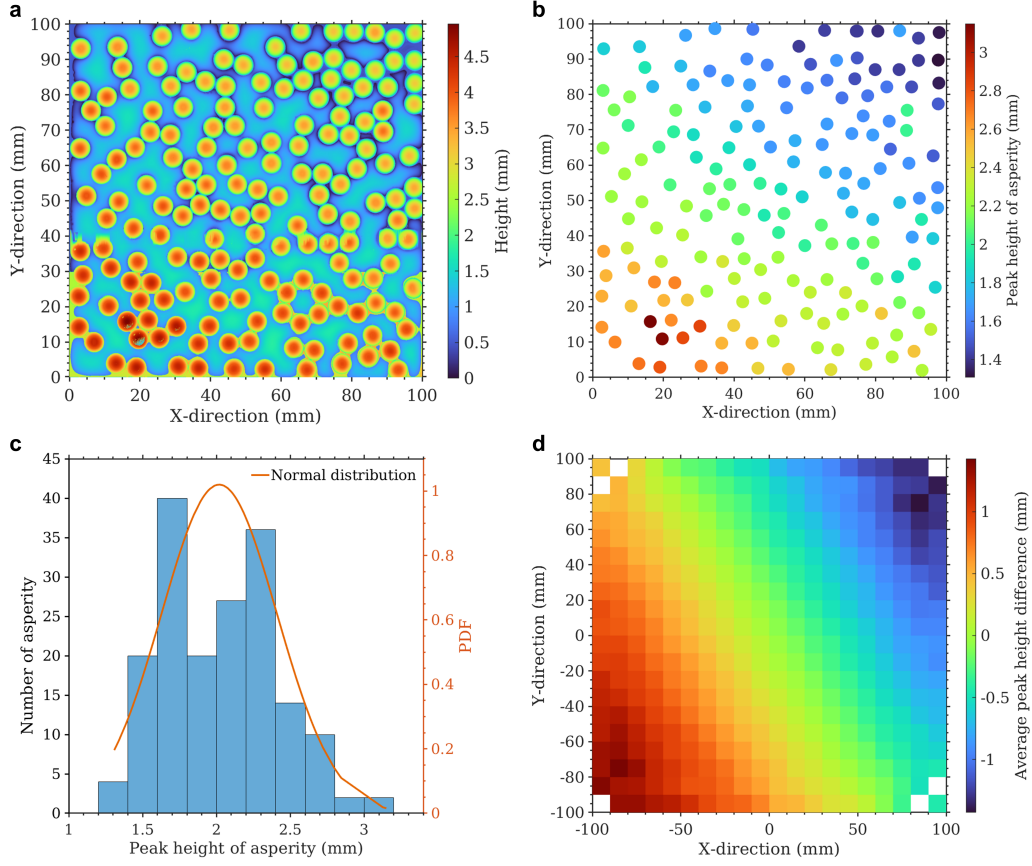


Figure 3. a: Topographical map of the analog fault interface. The blueish part is the embedding silicone block while the colored circles are the asperities created by the PMMA beads. There are a few non-measured points in the bottom-left corner that have little effect on characterizing the interface. b: Peak height of each asperity. The minimum and the maximum are 1.31 mm and 3.15 mm, respectively. c: Distribution of the peak heights of all the asperities. The asperities with peak heights ranging from 1.4 to 2.6 mm account for the majority. A standard deviation of 0.39 mm indicates a small variance in the peak heights. d: Average peak height difference as a function of the x and y direction. This highlights the large scale variation of the peak heights.

to its transparency, the PMMA enables a clear direct observation of the deforming medium (Lengliné et al., 2012; Jestin et al., 2019). The shear modulus of the PMMA is estimated as 2277.1 MPa (Selvadurai & Glaser, 2015).

The normal force F_N is applied by the vertical movement of the rigid load platen driven by a high-precision micro stepper motor (LoadTrac II), and uniformly transferred to the PMMA plate through the ball bearing and the rigid aluminum frame. A sensor of resolution 0.01 N is utilized to record the normal force and maintain a constant normal load throughout the whole duration of an experiment. We run the shear actuator, a combination of servo and stepper motor, with a constant displacement rate V_S to drive the translation stage and the rigid loading cylinder to impose the shear force F_S while maintaining a normal force F_N on the PMMA plate. The loading cylinder is composed of the aluminium alloy 2017A, with a stiffness of 78 N/ μm . The shear force F_S is measured using a sensor placed between the cylinder and the translation stage, with a resolution of 0.01 N. The stiffness of this sensor is 1 N/ μm , thus most of the loading stage deformation is actually taking place within the force sensor. We employ a laser (Keyence IL-S025), range 10 mm and resolution 0.1 μm , to measure the displacement of the PMMA plate, d_P (Figure 2). For all the experiments, we keep the initial value of d_P the same to ensure each fault slip starts from the same position.

Prior to performing the experiments, we fix the PMMA plate to the aluminum frame and attach the silicone block to the rigid steel base and clamp it. We use a digital level to make sure that the whole experimental system, especially the slip plane, is flat horizontal. Each experiment begins at the moment when the shear force starts to increase on the PMMA plate, given the analog fault has been previously loaded by a stable normal load. The duration of each experiment is set to 600 s. We performed 28 experiments by applying various normal loads ranging from 10 N to 1000 N and displacement rates ranging from 5.0 $\mu\text{m/s}$ to 15.0 $\mu\text{m/s}$ (Table S1). We define the x-direction as the sliding direction of the PMMA plate while the direction y is set perpendicular to the x-direction.

To demonstrate the transition from steady slip to stick-slip in our analog fault system, the evolution of the shear force, F_S , under multiple normal loads, F_N , maintaining the same loading rate V_S of 5.0 $\mu\text{m/s}$ is presented in Figure 4. We clearly observe the steady sliding of the interface when the normal load is quite small (e.g., $F_N = 10$ N). On the other hand, multiple stick-slips are observed when the normal load becomes greater

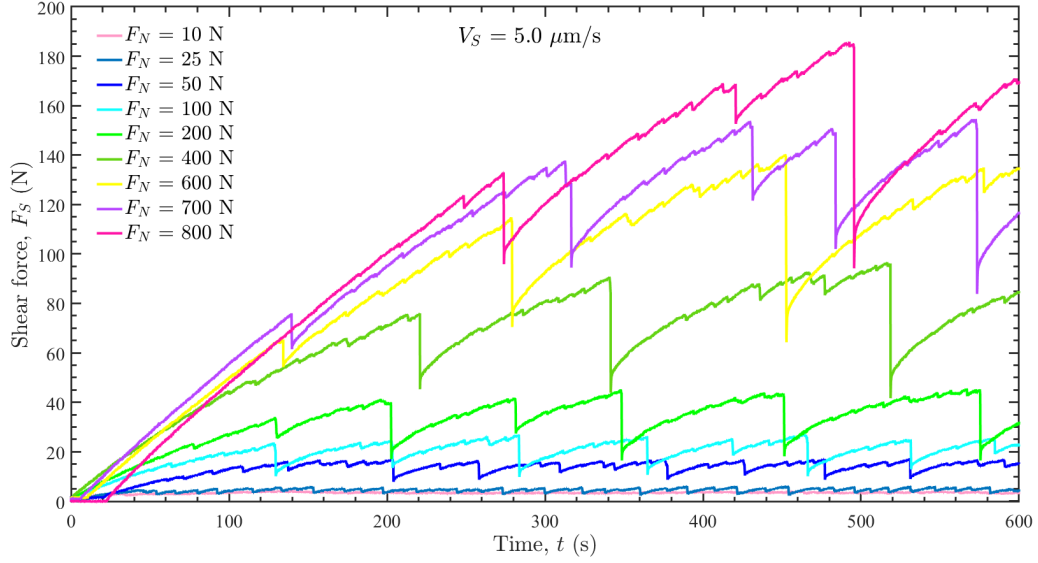


Figure 4. Temporal evolution of the shear force under multiple normal loads. The interface slips steadily when the normal load is quite small while evident stick-slips occur when the normal load becomes greater than 50 N. With the increase of the normal load, the shear force drop also increases.

than 50 N (Figure 4). In addition, the shear force drop of each stick-slip increases with the increase of the normal load.

2.3 Optical Monitoring

To capture the positions of asperities and compute their slips during the experiments, we use a high-resolution camera (Nikon D800) with a lens (Nikon 105mm f/2.8D AF Micro-Nikkor) in automatic focus mode to record videos. A mirror fixed inside the aluminum frame, which is inclined at 45 degrees, reflects the interface and moves with the sliding of the PMMA plate during the experiments (Figure 2). The main settings of the optical system are as follows: aperture size f/14, exposure time 1/30 s, and photosensitivity (ISO) 100. Two LED lights are placed behind the camera to supplement sufficient light for the clear observation of the interface. We record videos of dimensions in 1920×1080 pixels with a sampling rate of 29.97 frames per second. In addition, to synchronize the force measurement and the optical monitoring, we send an electrical synchronization signal and correct the time base of each record.

For each experiment, we extract all pictures taken by the camera between the times t_0 and t_f which are respectively the times at the beginning and the end of an experiment. From this set of pictures, we extract the slip of each individual asperity as a function of time. Denoting $x_i(t)$ and $y_i(t)$ the positions of the center of asperity i in a fixed reference frame (attached to the ground) we can define the displacement, $d_i(t)$, of an asperity along the loading direction in this fixed frame,

$$d_i(t) = x_i(t) - x_i(t_0). \quad (1)$$

Similarly, we define $x_P(t)$ as the position of the center of the mirror in the same fixed frame and then its displacement (which corresponds to the displacement of the PMMA plate as well), is computed as:

$$d_P(t) = x_P(t) - x_P(t_0). \quad (2)$$

The cumulative slip of asperity i at time t is defined as the difference of the displacement between the two sides of the interface (i.e., the asperity and the PMMA plate):

$$u_i(t) = d_i(t) - d_P(t). \quad (3)$$

As the camera and the silicone block are both fixed to the ground while the mirror moves with the sliding PMMA plate, the position of each asperity, i , on pictures taken by the camera is relative to the moving frame of the mirror and is noted $(x_i^*(t), y_i^*(t))$. It follows that the displacement of an asperity in this moving frame is simply $d_i^*(t) = x_i^*(t) - x_i^*(t_0)$. From the definition of the cumulative slip introduced before, this displacement, $d_i^*(t)$, corresponds exactly to the cumulative slip, $u_i(t)$ of asperity i . Consequently, the cumulative slip of each asperity is obtained by tracking the evolution of its position, $x_i^*(t)$, between time t_0 and time t_f .

We developed a two steps procedure for tracking the evolution of the position $x_i^*(t)$ of each asperity i in the moving frame of the mirror. In the first step, we applied the circular Hough transform algorithm implemented within MATLAB for automatically detecting circular objects (Yuen et al., 1990; Davies, 2005). From the first and last pictures at times t_0 and t_f respectively, we extract the initial position $x_i^*(t_0)$ and final position $x_i^*(t_f)$ of asperity i . We also estimate the initial position of the beads, $y_i^*(t_0)$ in the direction perpendicular to the slip direction.

The initial positions of asperities detected at time t_0 are shown in Figure 5. The asperities marked by red circles, with a total number of $N = 144$, are retained in our

analysis while the asperities with blue markers are excluded from the subsequent image analysis because they are located too close to one of the image edges. We note the value of N may change with different experiments mainly due to the field view of the camera, but it fluctuates around 140. In addition, we obtain the radius R , which is 36 pixels, and compute the scaling of the image from the known radius of the PMMA beads ($R = 3$ mm), 12 pixels/mm. Based on the initial and final positions of asperities, we are able to estimate the total slip $u_i^*(t_f) = x_i^*(t_f) - x_i^*(t_0)$ of each asperity. Due to the constant loading rate, a simple linear trend between these two positions gives an approximate position, $x_i^*(t)$ of asperity i at each time step. This provides a first order estimate of each asperity location during the experiment. In the second step, in order to obtain the most accurate locations, we applied an image correlation technique (Sutton et al., 2009) to refine these first measurements.

To quantify the slip of each asperity, a square window for image correlation with a size of $\sqrt{2}R$ is defined at the center of each asperity based on our previous estimates of $x_i^*(t)$ and $y_i^*(t_0)$. We extract the image defined by the square correlation window of each asperity at all frames. For each asperity, we compute the FFT (fast Fourier transform)-based two-dimensional cross-correlation between the extracted window defined at time t_k and the window defined at time t_{k-1} . From the correlation map, we isolate the position of the maximum value which gives the displacement of the bead. We then shift the correlation window of the second frame based on this displacement and repeat the procedure until the computed displacement is null. At this last stage, we then extract a sub-sample displacement by interpolating the correlation map around its maximum. The final displacement of the bead between the two time frames is then obtained by summing all displacements computed during this iterative process. Repeating this procedure for all time frames and for each bead we are able to obtain the cumulative slip of each asperity during the whole duration of an experiment. The typical resolution of the resolved displacement in each direction is of the order of 0.01 mm.

Due to the geometry of our experimental setup, the non-parallelism which may result from the non-perfect 45 degree inclination of the mirror and/or the non-parallel view between the camera lens and the slip plane (Figure 2), can create a non-linear scaling along the x axis. In order to eliminate this effect, we correct the cumulative slip of asperity i based on its total slip $u_i(t_f)$, which is supposed to be no greater than the displacement $d_P(t_f)$ of the PMMA plate at time t_f . Given the corrected cumulative slip

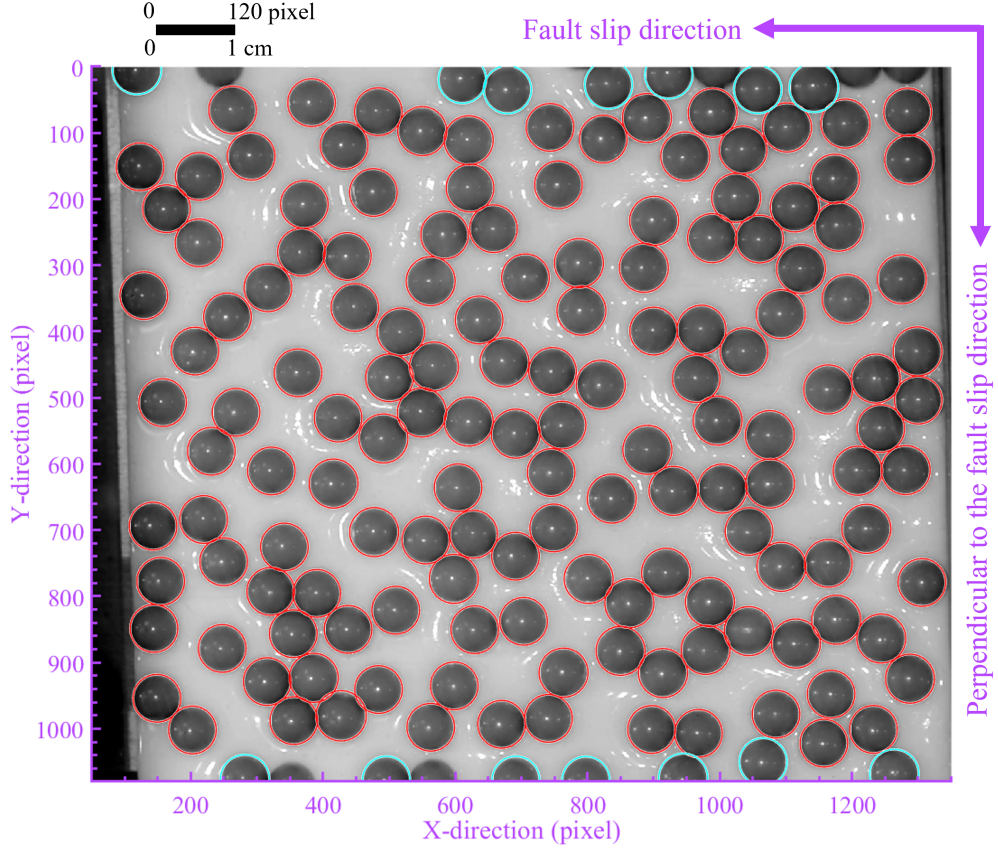


Figure 5. Typical automatic detection results indicating the initial positions of asperities at time t_0 , on the interface within a region of interest of dimensions 1300×1080 pixels (i.e., 108.33×90 mm). The asperities without markers represent the undetected ones while the asperities with blue circles correspond to the excluded ones as their correlation windows exceed the image boundary. A total of $N = 144$ asperities marked by red circles are kept and their positions $x_i^*(t_0)$ are taken as the initial positions for computing the slip through the image correlation.

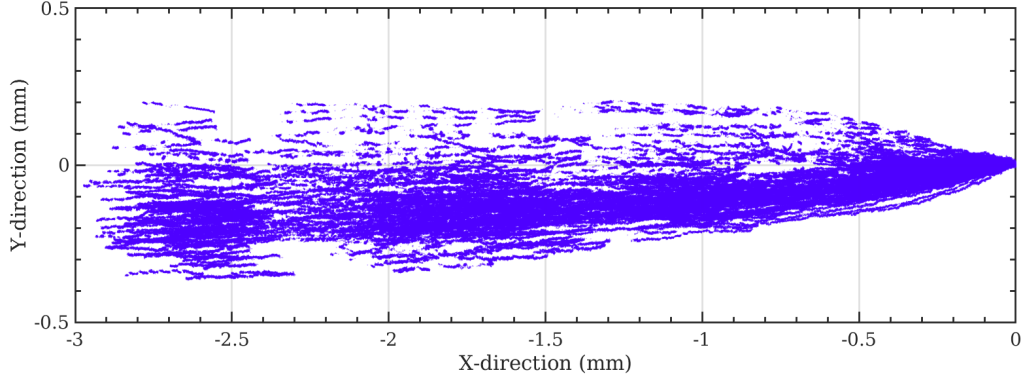


Figure 6. Trajectories of all the asperities during the whole duration of an experiment under a normal load of 400 N and a loading rate of $5 \mu\text{m/s}$. The onset of each trajectory is superimposed to be at the origin $(0,0)$. The prominent gaps correspond to the large stick-slip events.

$u_i(t)$ of asperities, we then update the displacement $d_i(t)$ of asperities following the equation (3).

Finally, we also note that the asperities also exhibit slips perpendicular to the loading direction. These cumulative slips are near-evenly distributed around zero and the maximum cumulative slip is quite small compared to the cumulative slip along the faulting direction. We present the trajectories of all the asperities during the whole experimental duration in Figure 6, where the onset of the trajectory of each asperity is set to be at the origin $(0,0)$. The total slip during this experiment is of the order of the asperity size, $R = 3 \text{ mm}$, and the slip in the x direction is about 10 times larger than that in the y direction. There is a fan shape of the trajectories with a mean y -direction that is close to zero. We observe several prominent gaps that correspond to the large stick-slip events during the faulting. For the other experiments under different loading characteristics, the total slip of asperities in the x direction is dependent on the loading rate and the experimental duration while that in the y direction is generally of the same order of $\sim 0.3 \text{ mm}$.

3 Collective Behavior of Asperities

3.1 Temporal Evolution of the Cumulative Slips of Asperities

To understand the individual behaviors of asperities as well as the relationship between each local asperity and the whole interface, we present the temporal evolution of the cumulative slips of individual asperities. For a better visibility, only 20 asperities, randomly selected out of 144 asperities, are presented in Figure 7. The cumulative slips of the 20 asperities are color-coded by their initial positions $y_i(t_0)$. We also indicate in Figure 7 the loading rate of the interface which is $15.0 \mu\text{m/s}$ here. Any asperity following this trend could be considered then as fully sliding. On the contrary, a fully sticking asperity would accumulate no relative slip with respect to the loading plate. Its behavior would appear as a horizontal line in Figure 7.

The stepping feature of cumulative slip evolution of the asperities in Figure 7 illustrates the repetitive stick-slip events of the interface (20 events in Figure 7a and a zoom on one of them in Figure 7b). These events involve all the asperities of the interface. In the time interval between these whole stick-slip episodes, during the sticking phase, the asperities show distinct behaviors. We observe that all the slipping rates are smaller than that of imposed loading rate (see the slopes of the cumulative slip of the asperities and the PMMA plate) but with a non-horizontal trend, which indicates that, actually, the asperities are slipping at a low rate during the sticking phase, instead of being fully locked.

It is noteworthy that the slips accumulated during each sticking period are not the same for different asperities. This proves that different asperities can slip at different rates, though they are all in the quasi-static regime (i.e. the sticking phase of the interface stick-slip behavior). Another interesting finding is that there are also some small visible slips that occurred at different single asperities during the overall sticking phase and correspond to small stick-slip events at the scale of several asperities. These small episodes contrast with global slip episodes, when all the local asperities slip rapidly in a synchronous way and that we define as a large stick-slip event (LSE). Moreover, the observation that the slips on all asperities after a LSE do not reach the imposed loading slip, indicates that accumulated stress is only partly released during such a whole scale event.

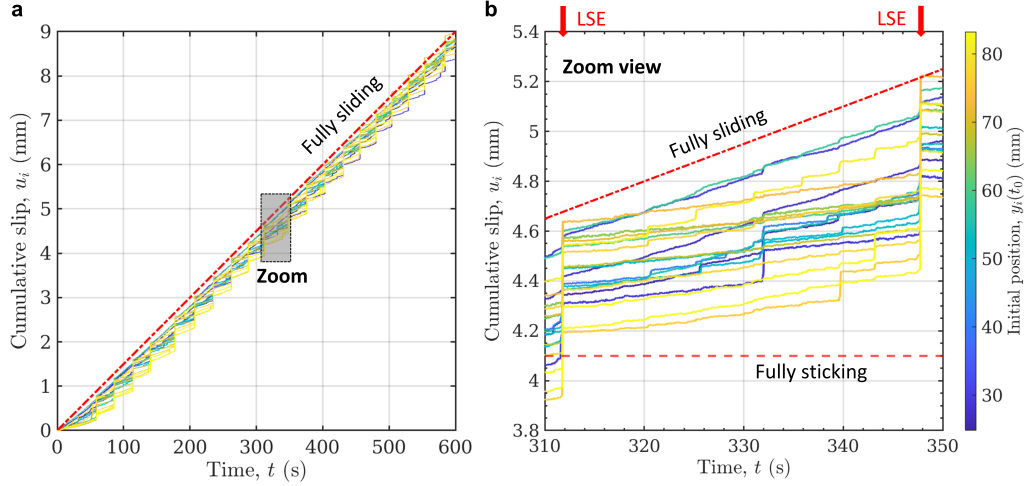


Figure 7. a: Temporal evolution of the cumulative slip in the x direction for 20 asperities during an experiment under a normal load of 200 N and a loading rate of $15.0 \mu\text{m/s}$. The cumulative slips of the 20 asperities are colored-coded by their initial y positions at time t_0 . b: Zoom view of Figure 7a showing the detailed behaviors of asperities during one time interval between two large stick-slip events (LSE) and ranging from 310 s to 350 s. Fully sticking indicates a locked state while fully sliding gives the slope of the imposed displacement rate to the system.

3.2 Slip Velocity of Asperities

Slip velocity reflects the slipping rate of asperities, which is estimated using a given discretization of the time (i.e., time step) during the whole experiment. The slip velocity $v_i(t_k)$ of each asperity i is computed as

$$v_i(t_k) = \frac{s_i(t_k)}{\Delta t} = \frac{u_i(t_k) - u_i(t_{k-1})}{\Delta t}, \quad (4)$$

where $s_i(t_k)$ is the slip of the asperity i at time t_k and Δt is the fixed time step of $1/29.97$ s determined by the sampling rate of the camera, i.e., $t_k - t_{k-1}$. Following the same experimental data used in Figure 7, for illustration, the slip velocity of all the 144 asperities ranging from time 330 s to time 350 s is shown in Figure 8, where the asperities are sorted in ascending order by their initial positions $x_i(t_0)$. A LSE involving the synchronous slipping of all the asperities is observed at the time 348 s. We also observe several small stick-slip events that share the same characteristic, which is the synchronized sliding of only a part of the asperities.

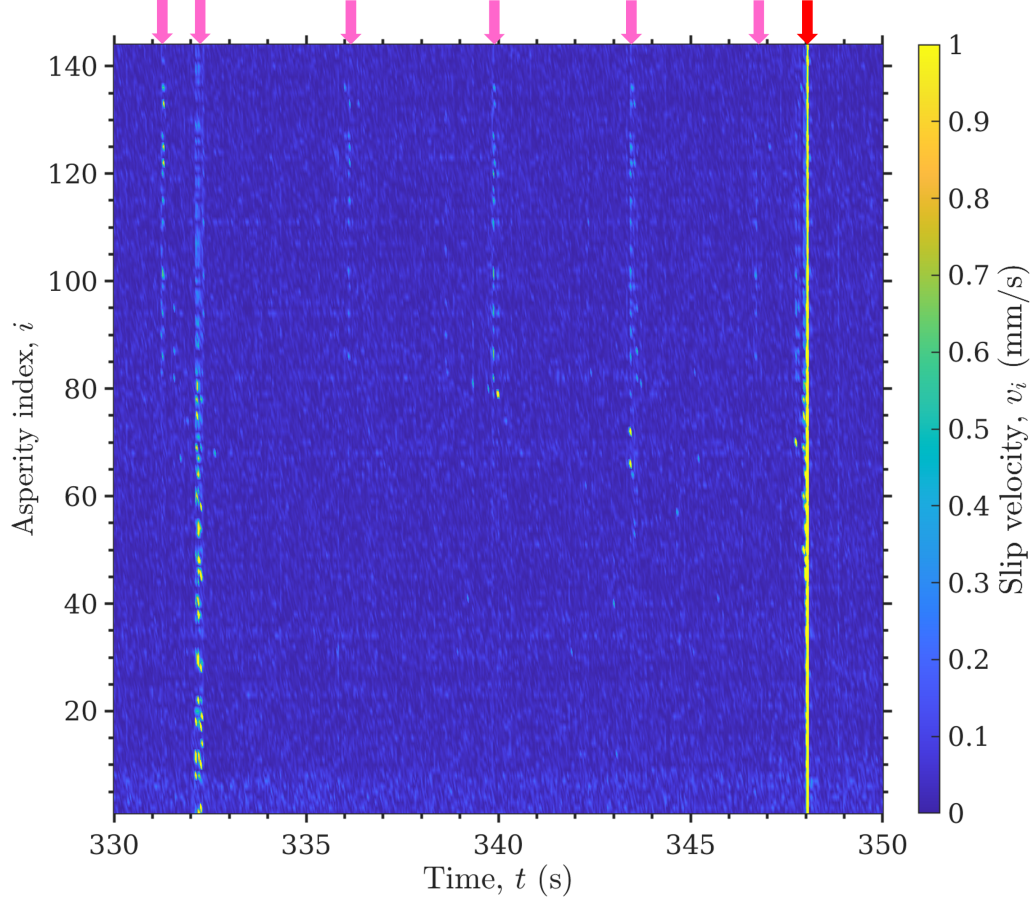


Figure 8. Slip velocity of all the asperities during the time period ranging from 330 s to 350 s of the same experiment shown in Figure 7. The asperities are sorted in ascending order by their initial x positions at time t_0 , $x_i(t_0)$. A large stick-slip event (LSE) indicated by the red arrow occurred at time 348 s observed, where all the asperities are synchronously slipping. During the sticking phase, there are also several small stick-slip events (SEs) which are indicated by the pink arrows involving the slipping of a part of asperities.

3.3 Mechanical Response of the Interface

In order to document the mechanical response of the frictional interface, we analyze how the friction coefficient, $\mu = F_S/F_N$, evolves as a function of slip. We compute the spatial average of the cumulative slip, $\langle u(t) \rangle$, over all asperities, N , following

$$\langle u(t) \rangle = \frac{1}{N} \sum_{i=1}^N u_i(t), \quad (5)$$

which is a global indicator of the collective behavior of all the asperities. As multiple seismic cycles (i.e., large stick-slip events) are produced during a single experiment, we report in Figure 9a the evolution of μ as a function of $\langle u(t) \rangle$, for all the cycles of a single experiment. Each cycle is separated based on the onset of a large scale slip event LSE (observed when μ reaches a local maximum before an abrupt decrease). The value of the friction coefficient mainly ranges between 0.10 and 0.23, which is a low friction coefficient but comparable to the values in other PMMA-PMMA interfaces (Baumberger & Caroli, 2006; Selvadurai & Glaser, 2015). We observe, in each cycle, an overall frictional strengthening stage during the sticking phase and a weakening stage during the slipping phase.

To focus on the sticking phase of the whole faulting process, the variations of friction coefficient, $\Delta\mu$, and of the average cumulative slip, $\Delta\langle u(t) \rangle$, are both computed relative to their respective values at the onset of these large scale slips. We plot the friction coefficient variation, $\Delta\mu$, as a function of the variation of the average cumulative slip of all the asperities, $\Delta\langle u(t) \rangle$, by superimposing all the sticking phases and the slipping phases, where each onset of the slipping phase is set to be $\Delta\mu = 0$ and $\Delta\langle u(t) \rangle = 0$ (Figure 9b). The curves represent the sticking phase while the circles represent only a few time steps after the onset of the LSE. We observe a good similarity between all seismic cycles, proving the repeatability of our observations. We observe that the friction coefficient during the period preceding the large scale event (LSE) is increasing. This strengthening of the interface is occurring while the interface is slipping. We observe that during this overall increase of the friction coefficient, there exist multiple instances where μ actually drops significantly compared to the error of the friction coefficient measurement. The strengthening of the interface (an overall increase of μ) is thus not a homogeneous process and is slip-controlled in a non-linear manner. This shows as well that this strengthening stage, conventionally considered as the stable regime of a fault, actually consists of many small-scale destabilizing events. The rapid slip that occurs dur-

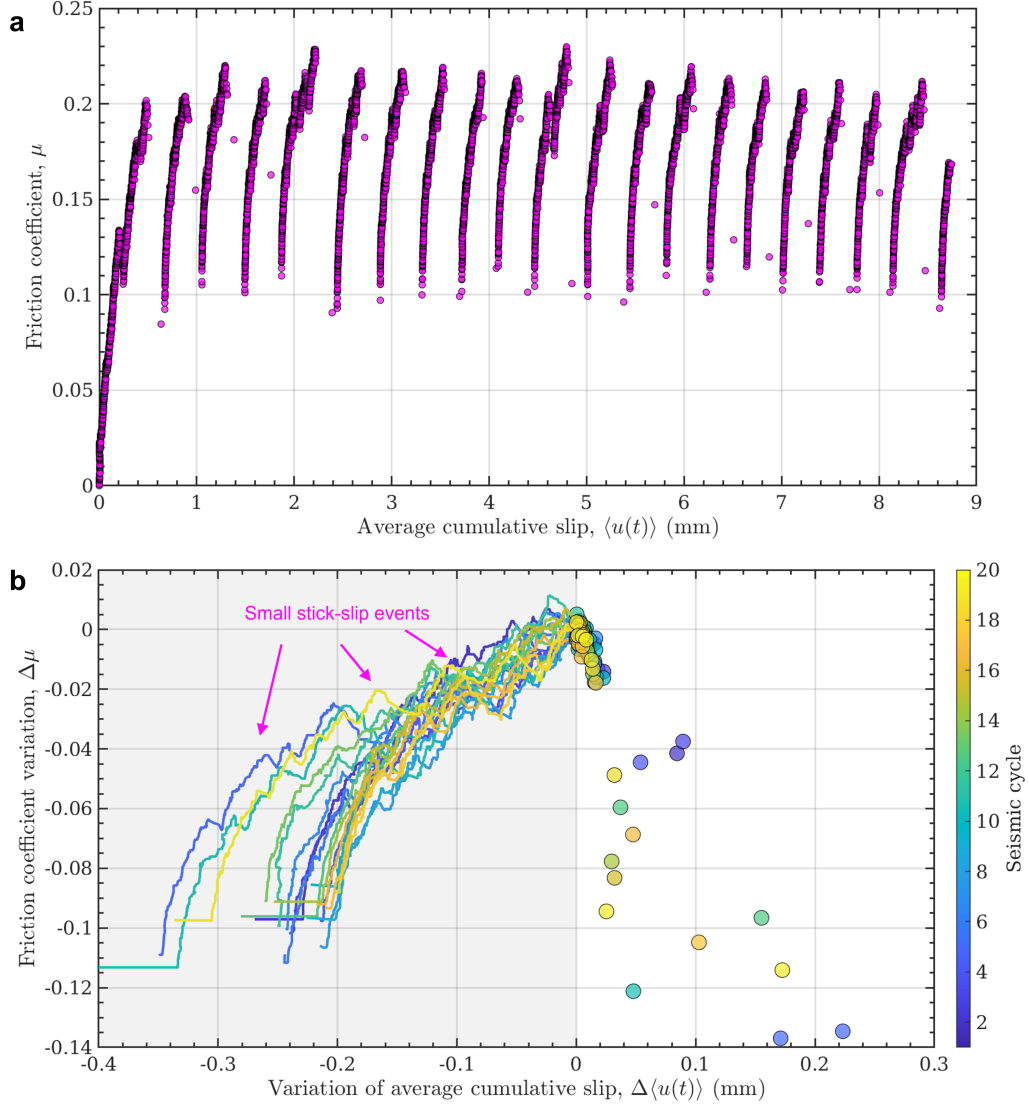


Figure 9. a: Evolution of the friction coefficient, μ , as a function of the average cumulative slip, $\langle u(t) \rangle$, during the same experiment shown in Figure 7 with multiple seismic cycles. b: Friction coefficient variation, $\Delta\mu$, as a function of the variation of the average cumulative slip of all the asperities, $\Delta\langle u(t) \rangle$, for the same experiment shown in Figure 9a. All the seismic cycles represented by different colors are superimposed together by setting the onset of each slipping phase as the origin. The colored curves in the shadow indicate different sticking phases while the circles denote the corresponding slipping phases.

ing a LSE is not well captured by our experiments mainly because of the limited time resolution of the camera that does not allow a sufficient time sampling during this stage. It is also possible that the weakening part is velocity dependent which is not well captured here since Figure 9b represents the friction coefficient as a function of slip with no information on the velocity.

3.4 Topographical Effect on Interseismic Slipping Behaviors

Our results show that many small stick-slip events accompanied by friction coefficient drops are found during every fault strengthening stage (Figure 9). These interseismic, small stick-slip events result from the slip of a limited number of asperities on the interface. In order to identify what controls the number and the amount of these partial slips, we document the interseismic slipping behaviors of the asperity using the interseismic coupling coefficient (Hyndman et al., 1997). We denote the onset times of the j and the $j+1$ large stick-slip events as $t(\text{LSE}(j))$ and $t(\text{LSE}(j+1))$, respectively. To describe the extent of the slipping of the asperity i during the interseismic phase between $t(\text{LSE}(j))$ and $t(\text{LSE}(j+1))$, the interseismic coupling, $\lambda_{i,j+1}$, is computed as

$$\lambda_{i,j+1} = 1 - \frac{u_i(t(\text{LSE}(j+1))) - u_i(t(\text{LSE}(j)))}{d_P(t(\text{LSE}(j+1))) - d_P(t(\text{LSE}(j)))}. \quad (6)$$

We note that λ is in the range $[0, 1]$, where $\lambda = 0$ indicates no coupling or fully sliding while $\lambda = 1$ denotes a fully coupled interface or sticking. For experiments with multiple seismic cycles, we compute the final interseismic coupling for each asperity i by averaging λ_i over all of the interseismic phases.

With the experimental data used in Figure 9, we present the interseismic coupling of these asperities along the interface (Figure 10). We observe a large scale trend of this interseismic coupling that we can link with the same trend observed from the peak height of asperity derived from the topographical map (Figure 3b). A higher peak height of asperity corresponds to a higher interseismic coupling while a smaller peak height is corresponding to a lower interseismic coupling. This can be interpreted in terms of normal stress on the asperity where a higher peak height causes a greater normal stress, and therefore creates the locking of the asperity which increases the interseismic coupling. On the contrary, the asperities with smaller peak heights have a low normal stress and thus cannot accumulate large shear stress (and consequently large slip deficit) and will fail more often during the interseismic phase and have a low coupling, i.e., low values of λ .

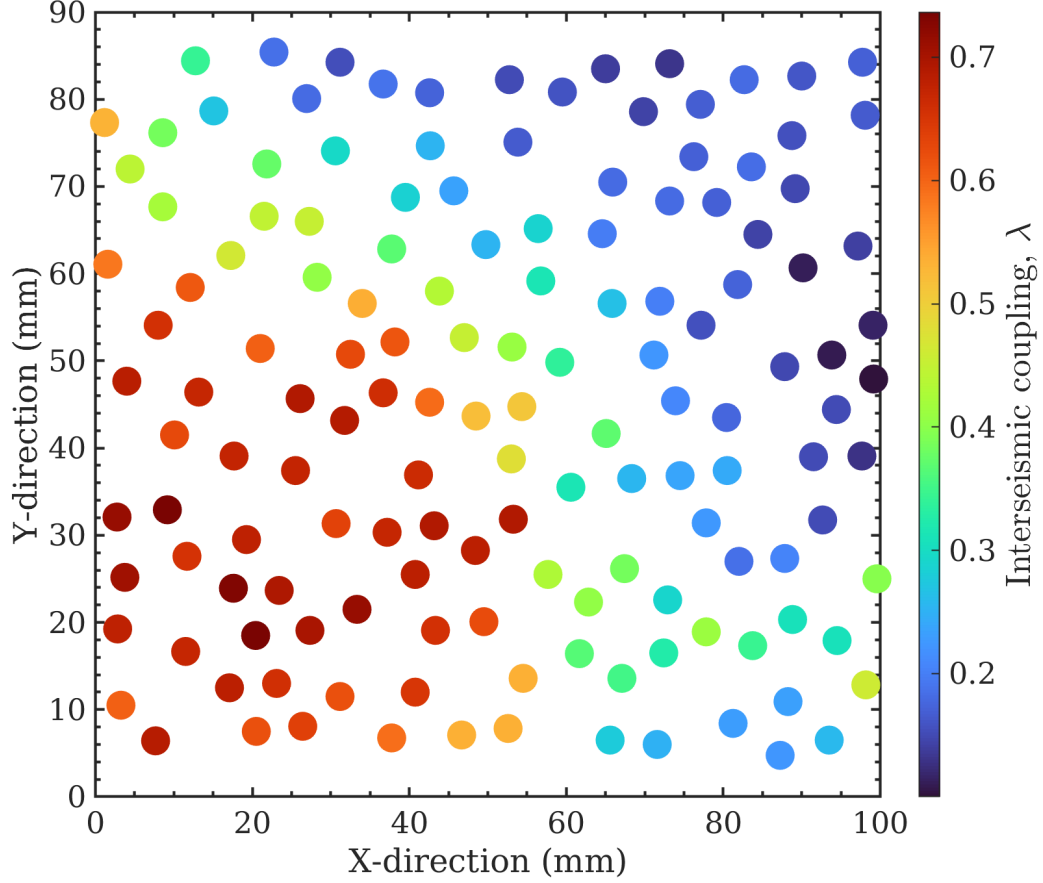


Figure 10. Map of the interseismic coupling of asperities along the interface using the same experimental data shown in Figure 9. A similar pattern between the peak heights of asperity (Figure 3b) and the interseismic coupling is observed, which shows that a larger peak height corresponds to a larger interseismic coupling whereas a smaller peak height corresponds to a lower interseismic coupling.

We also investigate the direct effect of the macroscopic normal load on the interseismic coupling, as shown in Figure 11. For all experiments with the same normal load, we compute the interseismic coupling of each asperity, which is indicated by the color circles. The average evolution of the interseismic coupling with peak heights conceals some scattering. Indeed, we can observe from Figure 11 that for the same normal load and the same asperity height, different values of λ are computed. To present the evolution of the interseismic coupling as a function of the peak height of asperity, we average the interseismic coupling values over peak heights within a bin width of 0.10 mm. It evidences that, when the normal load is low: 10 N and 25 N, all the asperities have a quite small interseismic coupling, a value that is not distinguishable from zero. The interseismic coupling shows no dependency on the peak height. This is consistent with the mechanical response of the fault system shown in Figure 4, where the global fault slips almost steadily under the normal loads of 10 N and 25 N.

As the normal load increases and becomes large enough such that large stick-slips of the whole fault system are observed, we evidence that interseismic coupling is then dependent on the peak height of asperities. The asperities with low peak heights correspond to low normal stresses, thus inducing the small stick-slip events observed in between the large stick-slip events due to a small interseismic coupling. For the same peak height of asperity, the interseismic coupling increases with the increase of normal stress, which strengthens the locking of the asperities. The maximum value of the interseismic coupling is about 0.55 which is significantly lower than 1. This is consistent with the partial slipping of asperities shown in Figure 7b and Figure 8. It is interesting to note a transition of the interseismic coupling, for a given normal load, at a specific peak height threshold. This peak height threshold is decreasing as a function of the increased normal stress (from about 2.67 mm at 50 N to about 1.85 mm at 700 N). The interseismic coupling above this peak height threshold converges for all loading conditions to a constant value of around 0.6. Below the threshold, λ decreases towards 0.

4 Interactions between Asperities during the Strengthening Phase

4.1 Collective Slip Episodes

To investigate the spatiotemporal interactions of asperities, we use a two-step procedure in order to define and characterize slip episodes (SEs). In the first step, we an-

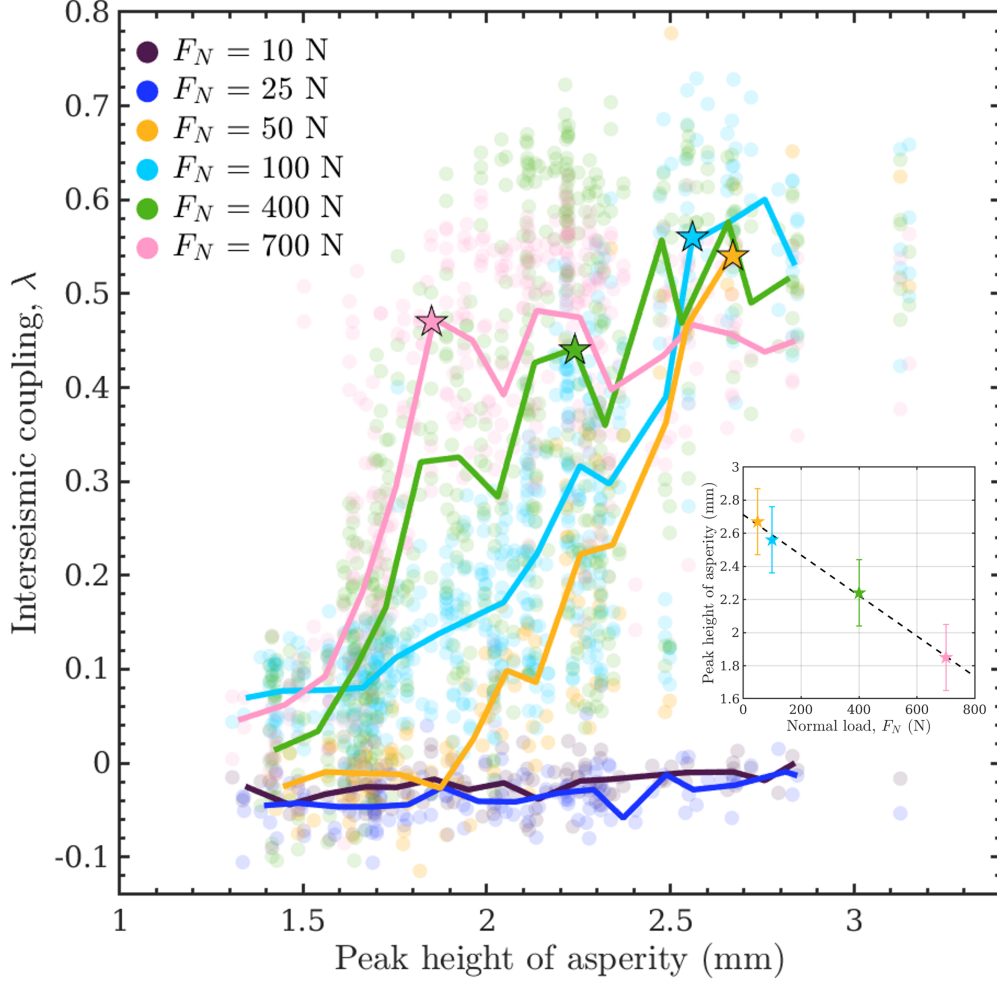


Figure 11. Evolution of the interseismic coupling at different peak heights of asperity under multiple normal loads. The circles with one filled color are the dataset computed for all the experiments under the corresponding normal load. Each curve is obtained by averaging the interseismic coupling over the peak height of asperity with a bin width of 0.10 mm. The inset displays the peak height of asperity at transitions from high to low coupling (stars) as a function of the normal load, where the peak height of asperity decreases with the increase of the normal load.

analyze individually each asperity to isolate individual asperity slips (IASs) from their slip history. In the second step, we identify collective behavior by clustering IASs based on their time and space connection to build slip episodes. The first step is realized by thresholding the velocity $v_i(t)$ for each asperity i . We use a threshold Γ_i specifically for each asperity i , which is determined by considering the median \tilde{v}_i and the median absolute deviation D_i^{med} of the slip velocity $v_i(t)$,

$$\Gamma_i = \tilde{v}_i + c \cdot D_i^{med}, \quad (7)$$

We test several values of the coefficient c in front of D_i^{med} (see Figure S1) and found that the value retained here ($c = 6$) is best able to separate noise from slip event. Following equation (7), we define the IASs as periods with $v_i(t) > \Gamma_i$ while the others with $v_i(t) \leq \Gamma_i$ are taken as minor slip events and possible noise, and are not included in the catalog of IASs. Figure 12 presents the slip events (blue stars) of one single asperity ($i = 98$) for the same experiment displayed in Figure 7 and its corresponding threshold Γ_{98} (thick magenta line). We find a diversity of slip velocities of IASs. To display the IASs with low slip velocities during the interseismic phase, we zoom in on Figure 12 during a time interval between two large stick-slip events, ranging from 310 s to 350 s (the same time period exhibited in Figure 7b). The observation that several IASs with moderate maximum slip velocity are observed for this asperity is actually consistent with the small stick-slip events found during the fault strengthening stage shown in Figure 9. For each experiment, we establish a complete catalog of IASs by computing the slip velocity $v_i(t)$ of all the asperities and the corresponding threshold Γ_i .

To cluster in space and time all the IASs defined at different asperities into collective SEs covering multiple asperities and time steps, we analyze the time and space connections of these IASs. We define a link between a pair of IASs if the two events are separated in time by one or less time step and if they have a spatial connection (i.e., they are nearest neighbor), introducing a two-dimensional Delaunay triangulation, and considering the location of each asperity as a vertex (Lee & Schachter, 1980). The edges of the resulting triangulation give the spatial connection between asperities used to make clusters. Additionally, we assume that an asperity is always spatially linked with itself. The IASs simultaneously connected in time and space scales are clustered as a new SE using a single linkage clustering algorithm (Gan et al., 2020). IASs that are not linked to other neighboring IASs are considered as individual SEs. Figure 13 shows one SE last-

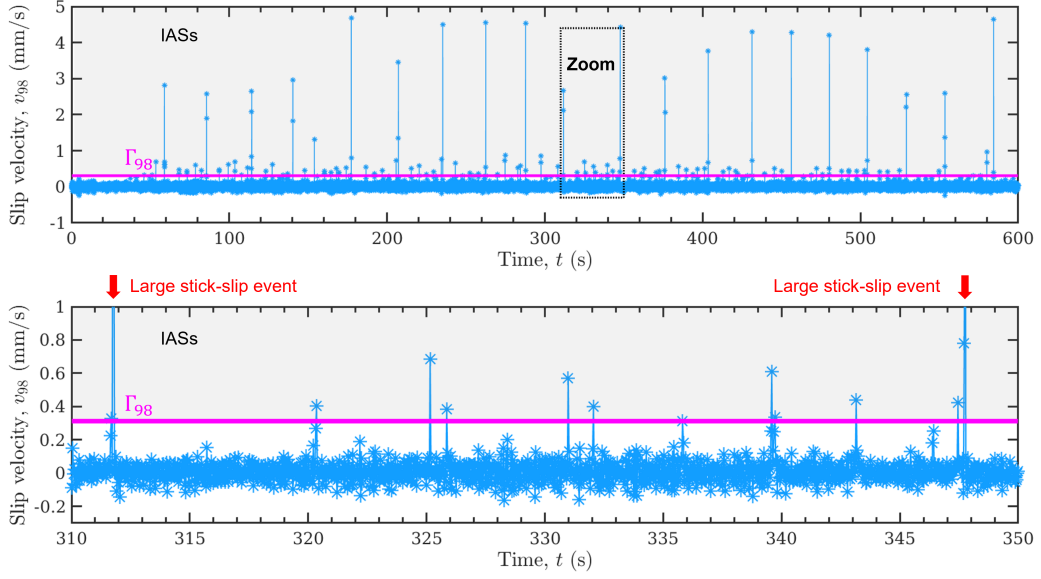


Figure 12. Time-localized slip events produced by a single asperity ($i = 98$) in the same experiment shown in Figure 7. The blue stars and the thick magenta line represent slip events and the corresponding threshold Γ_{98} specifically computed for this asperity. The slip events localized in the shadow region with slip velocity greater than the threshold are defined as IASs while the others indicating minor slip events and noise are removed. A zoom view showing the low amplitude IASs during an interseismic phase ranging from 310 s to 350 s is presented below. Several IASs with low slip velocities are observed.

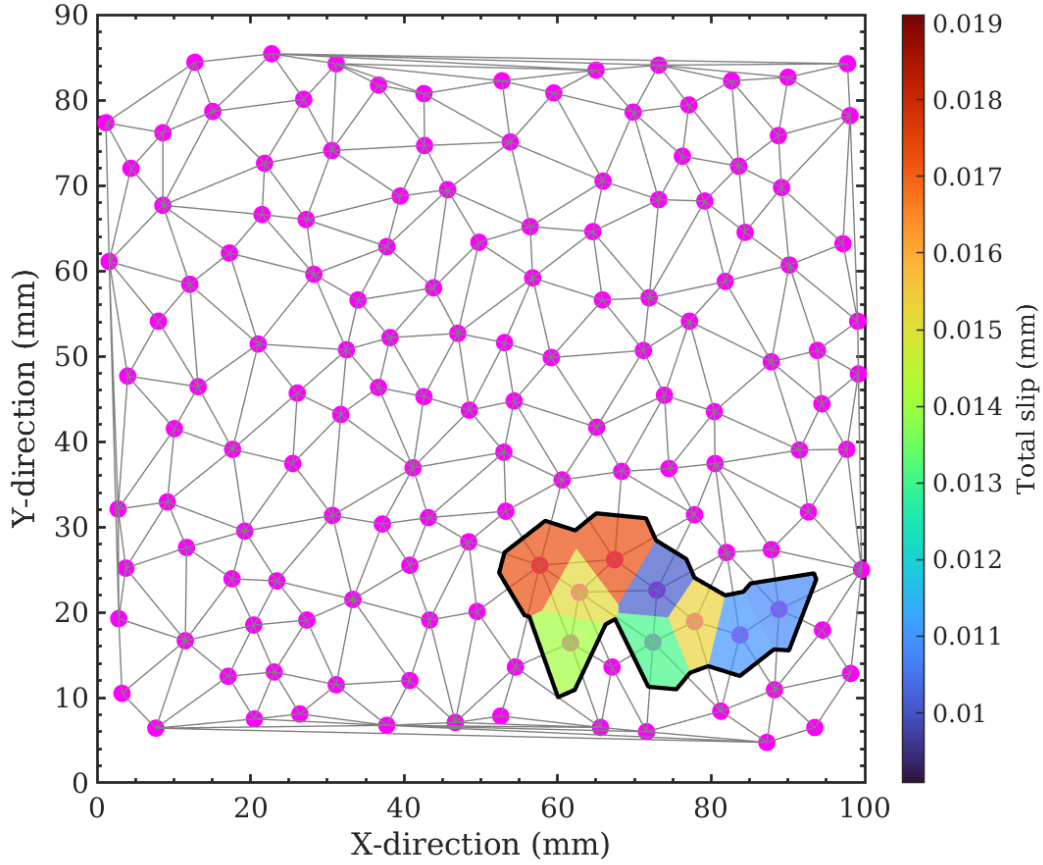


Figure 13. Example of one SE lasting one time step which is composed of nine IASs (polygons with different colors) colored by their total slips. The magenta dots and gray lines indicate the bead locations and the spatial connections all over the interface determined by the Delaunay triangulation, respectively.

ing only one time step, and composed of nine IASs. The polygons with different colors represent the slip area allocated to each IAS and are determined by the Voronoi diagram corresponding to the performed triangulation (Fortune, 1995). We, therefore, are able to build the catalog of spatiotemporal SEs for each experiment.

4.2 Magnitude-Frequency Distribution

In order to characterize the so-formed slip events, we first investigate their magnitude distribution. The magnitude of the slip event is estimated based on the computation of their moment, M_0 . For one SE containing n IASs, its seismic moment is com-

puted as:

$$M_0 = \sum_{i=1}^n G \cdot A_i \cdot s_i, \quad (8)$$

where G is the shear modulus of the PMMA, A_i and s_i are respectively the slip area and the slip of each IAS i that compose this SE. Then, we can calculate the magnitude M of each SE following (Hanks & Kanamori, 1979) as:

$$M = (\log_{10} M_0 - 9.05)/1.5. \quad (9)$$

The magnitude-frequency distributions of the SEs extracted from three experiments, which are under the same normal load of 400 N but with three different loading rates, are presented in Figure 14. The symbols with crosses represent the large stick-slip events that involve all the asperities of the interface and subsequently with a size controlled by the finite size of the interface. As evidenced already for finite systems, the distribution of events is bimodal: exponentially distributed size for the events not reaching the interface and a peak for system-wide events (Fisher et al., 1997). Excluding system-wide events, the observed distributions follow a typical Gutenberg-Richter distribution (Gutenberg & Richter, 1944): $\log_{10} N(m) = a - bm$. For the three experiments under loading rates of 5.0 $\mu\text{m/s}$, 10.0 $\mu\text{m/s}$, and 15.0 $\mu\text{m/s}$ and a normal load $F_N = 400$ N, their b values are 1.21 ± 0.05 , 1.44 ± 0.1 , and 1.35 ± 0.12 , respectively. A gray dashed line showing a reference b value of 1.3 is displayed in Figure 14. We can observe that all these three experiments have a b value nearly similar to this reference. It shows that the b value has no clear dependence on the loading rate of the system. In addition, our experimental results show that the b value is insensitive as well to the imposed normal load (see Table S2).

4.3 Moment-Duration Scaling Relation

For regular earthquakes, a scaling relation between the moment and the duration is commonly observed and takes the form $M_0 \propto T^3$ (Kanamori & Anderson, 1975). This relation can be understood from the representation of an earthquake as a circular crack expanding at a constant speed and with a constant stress drop. Another scaling relation has also been resolved for slow slip events observed in subduction megathrusts which follows the form $M_0 \propto T$ (Gao et al., 2012; Ide et al., 2007).

We represent from our SEs the relation between their duration, T , defined as the time difference between its onset and end, and their moment, M_0 (Figure 15a). The moment-

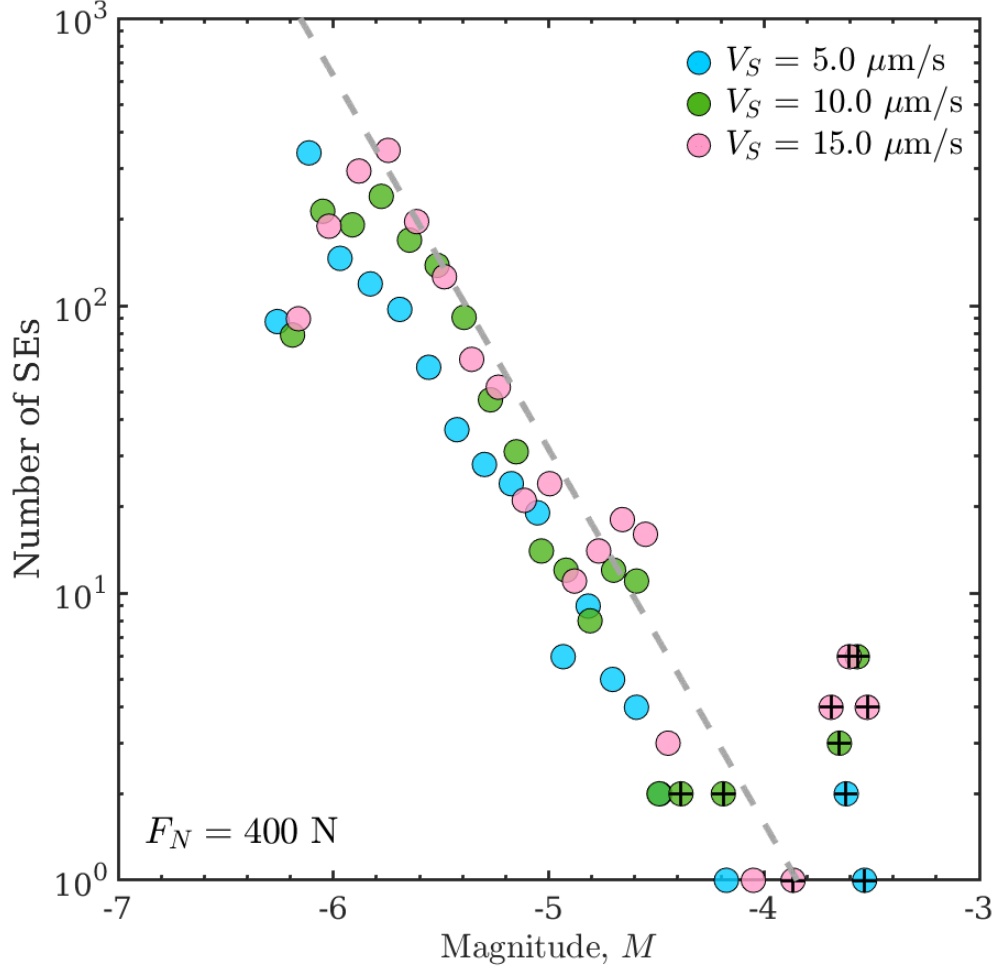


Figure 14. Magnitude-frequency distribution at different loading rates under the same normal load of 400 N. The circle symbols marked by crosses indicate the large stick-slip events at the global fault scale, which are excluded from the computation of the b value. The gray dashed line indicates a reference line with a b value of 1.3.

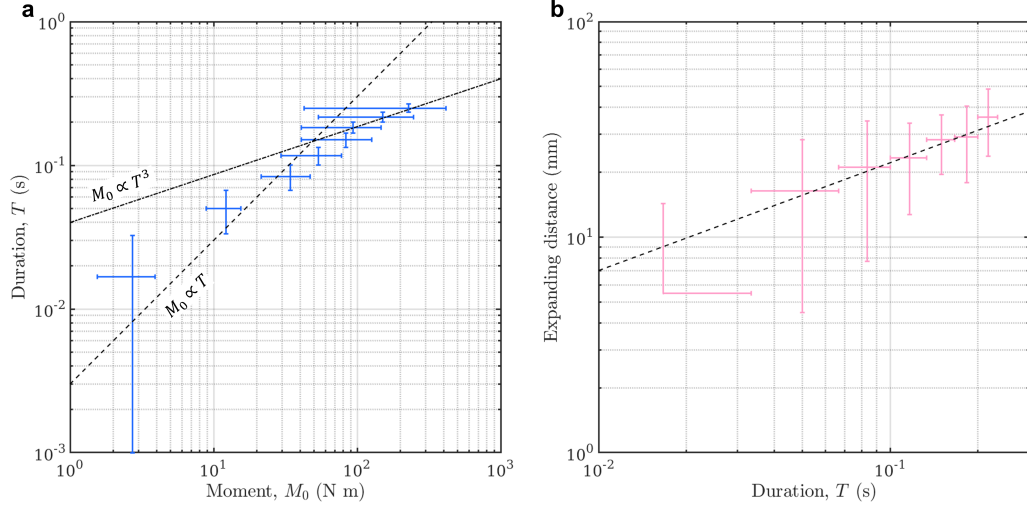


Figure 15. a: Moment-duration scaling relation obtained using SEs from all experiments at various normal loads and loading rates. The black dash-dotted line and dashed line represent the scaling relations of $M_0 \propto T^3$ and $M_0 \propto T$, respectively. The largest slip events, reaching the edge of the sample have been excluded. b: Scaling relation between the expanding distance of SEs and their duration. The black dashed line represents the square-root scaling relation between the expanding distance and the duration.

duration scaling is represented for all experiments with various normal loads and loading rates. In order to retain in this analysis only confined ruptures and not be influenced by the condition at the edge of the sample, the largest slip events reaching the edge of the sample are excluded. We evidence a linear scaling relation close to $M_0 \propto T$ for all the experiments for $M_0 < 100$ N m and a transition to the scaling for earthquakes ($M_0 \propto T^3$) for the largest events.

For each SE, excluding large-scale stick-slip events, we also compute the distance between the first and last slipping asperities. The duration and expanding distance are averaged to present their relation, as shown in Figure 15b. We observe a square-root scaling relation between the expanding distance and the duration.

4.4 Temporal Decay of Slip Episodes

In order to investigate the possible time interaction between our identified SEs, we compute the time correlation between them, $C(t)$ with

$$C(t) = \frac{1}{Tn_t} \sum_{i=1}^{n_t} \sum_{j=i+1}^n \Theta(t_j - t_i \in [t; t+T]), \quad (10)$$

where $\Theta(\mathcal{P})$ of proposition \mathcal{P} is 1 if \mathcal{P} is true and 0 otherwise. In order to take into account the time finiteness of the catalog, the first sum is performed up to n_t which is the largest index i such that $t_n - t_i < t+T$, where T is the duration of the time bin. The equation (10) actually gives the average rate of SEs at time t following a preceding slip event and we represent an example of $C(t)$ computed for an experiment under a normal load of 200 N and a loading rate of 15 $\mu\text{m/s}$ (Figure 16). We observe a rapid decrease of $C(t)$ at a short time range, following a power law decay similar to $1/t$. After a duration of about 1 s, the average rate of SE stabilizes to a background rate of around 2 SEs per second. This indicates that interactions between SE exist for a short time and that they quickly decay. This evolution of the event's rate bares some analogy with Omori's law observed after large earthquakes which gives as well a decay of the earthquake rate following $1/t$ (Utsu et al., 1995).

5 Discussion

5.1 Interseismic Coupling

Our results indicate that the interseismic slip rate relative to the loading rate, i.e. the interseismic coupling, λ , is related at first order to the normal stress imposed on the asperities. The transition from small to high coupling is a function of the normal load (the height of the asperity at this transition is decreasing with normal stress) but the value of the coupling at high or low normal stress is the same for any normal load. This is visible first as a global macroscopic effect affecting all asperities when we change the imposed normal load in our experiments (Figure 11). This can also be observed at the individual asperity scale where we observe that the asperity peak height is correlated with λ . Indeed, considering a simple Hertz contact model, a higher asperity height results in higher normal stress. The distribution of asperity heights in our experiments, therefore, leads to a distribution of normal stresses and a continuum of values of λ (Figure 11).

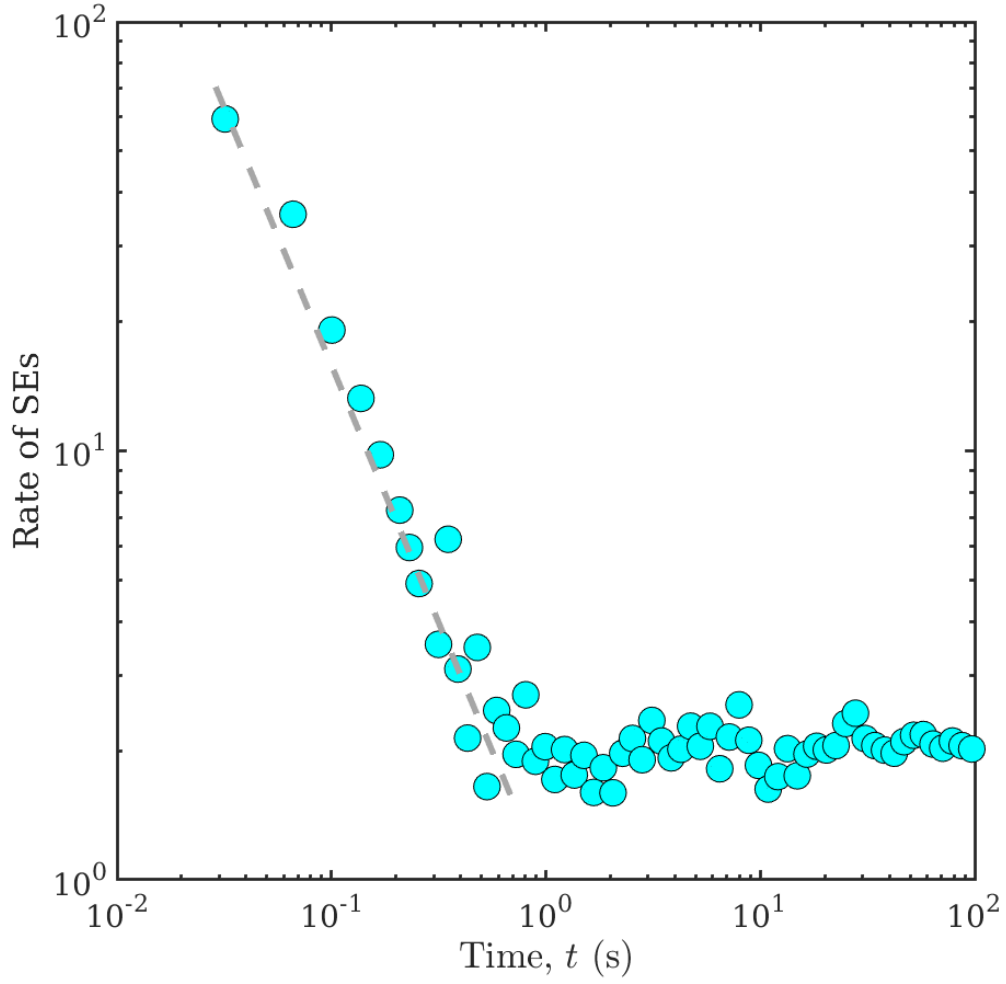


Figure 16. Temporal decay of SEs defined in an experiment under a normal load of 200 N and a loading rate of $15 \mu\text{m/s}$. The rate of SEs first decays rapidly with $1/t$ during about 1 s and then keeps stable as a background value of about 2 SEs per second.

It is tempting to relate the characteristic asperity height in our experiment to the critical reduction in the normal force, ΔF_N^* , that controls the transition from low to high coupling, as identified in the model of Scholz and Campos (1995, 2012). We note however that in this model the transition results from the sole effect of the global normal load since the interface is considered as homogeneous. This approach is thus describing the effective seismic coupling of the interface but not that of the asperities, which we can achieve in our experiments. We interpret that the effective coupling of the interface is a function of the quenched disorder of the fault and then indirectly of the normal stress. If we assume the same height of all the asperities, there would be no variance in interseismic coupling at different asperities at the same time. Similarly, the whole interface would have the same behavior as that of the asperities and lead to little collective effect. We emphasize here that a large scale topography of a fault with variations of the asperity heights can influence the effective seismic coupling of the fault differently from a classical normal stress level effect. This is a collective effect but related to the quenched disorder of the asperities.

Finally, we acknowledge that the definition of interseismic coupling is not completely satisfactory as it fails to capture the variation of the slip velocity inferred on some asperities in between two large scale stick-slip events. Indeed, we highlighted some transient activity and non-steady slipping rate for asperities which indicate that the value we computed only represents an effective behavior of the asperity at the time scale between two large scale stick-slip events.

5.2 Interfacial Elastic Energy

Our results evidence that for an interface composed of multiple asperities, as in our system, local slip events with various sizes (see Figure 14) are taking place at all times. We also note that large scale events that involve slips on all asperities of the interface are also observed. These large scale slip events can only happen when sufficient large stress has been accumulated on the strongest asperities. This requires that asperities at some time are synchronized such that initiating the failure at one location triggers the cascading rupture of all the asperities on the interface, thus generating the large scale stick-slip event. This is equivalent to a collective depinning induced by the long range elastic interactions in a slowly (quasi-static) loaded system.

We quantitatively illustrate such synchronization effect by computing the evolution of the interfacial elastic energy, E_h , and of the bulk elastic energy, E_t , following the definition of Schmittbuhl et al. (1996). The interfacial elastic energy, E_h , is quantified through the sum of the relative distance between two asperities over all the spatial links defined by the two-dimensional Delaunay triangulation:

$$E_h(t) = K_N \sum_{k=1}^D (l_k(t) - l_k(t_0))^2, \quad (11)$$

where l_k is the relative distance computed through the x positions of two asperities linked spatially and D is the number of the spatial links between two asperities defined by the Delaunay triangulation. K_N is the compressive stiffness between asperities, computed through $K_N = E_s \langle d_{asp} \rangle$, where E_s denotes Young's modulus of the silicone block and $\langle d_{asp} \rangle$ is the average distance between asperities which estimated to be 6 mm. The interfacial elastic energy, E_h , actually quantifies the variance of the change of distance between neighboring asperities, thus is related to the elastic force interactions between asperities. The bulk elastic energy, E_t , is the total elastic energy stored on the interface through the global loading, which is characterized by the collective change in the absolute positions of all the asperities along the x direction:

$$E_t(t) = K_S \sum_{i=1}^N (d_i(t))^2, \quad (12)$$

where K_S is the shear stiffness estimated using $K_S = G_s L$. G_s is estimated from Young's modulus of the silicone block, 1.1 MPa, while L is the size of the interface, 10 cm. N is the total number of asperities and d_i the displacement of each asperity.

We present the interfacial elastic energy, E_h , and the bulk elastic energy, E_t , as a function of the PMMA plate displacement, d_P , for different experiments with various normal loads but the same loading rate, as shown in Figure 17. We identify multiple large scale stick-slip events and the corresponding fault strengthening phases from the large abrupt drops of E_t and the slow accumulation of E_t , respectively. We also observe a similar pattern for the evolution of E_h , which is equivalent to the direct measure of the spreading of the x positions of the asperities apart from their initial position where $E_h = 0$. Additionally, we observe a clear dependency of E_h and E_t on the normal load, which is consistent with the mechanical response of the fault system shown in Figure 4. With the increase of normal load, the interfacial elastic energy, E_h , and the bulk elastic energy, E_t , also increase.

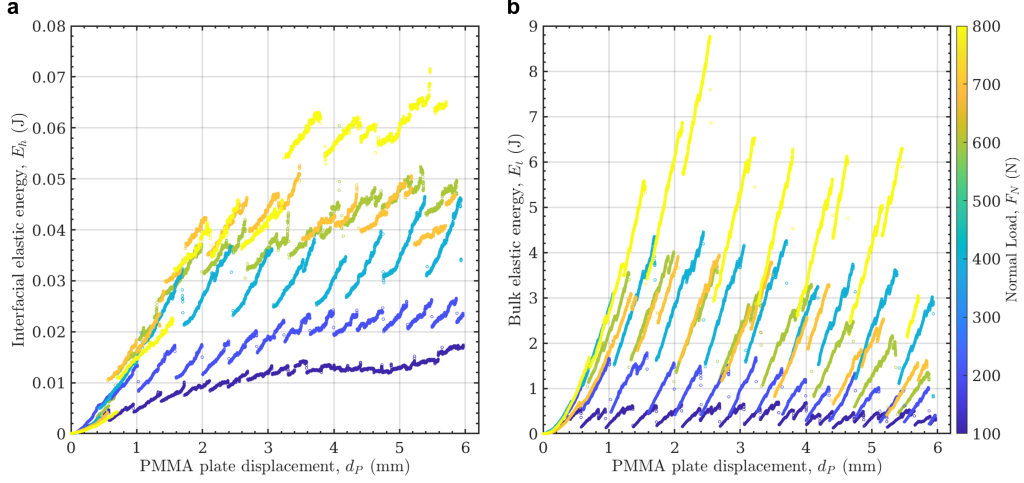


Figure 17. Evolution of (a) the interfacial elastic energy, E_h , and of (b) the bulk elastic energy, E_t , under different normal loads and the same loading rate. Both E_h and E_t accumulate slowly during the fault strengthening phases and drop when a large stick-slip event occurs. Both E_h and E_t show a clear dependency on the normal load.

Such evolution of the elastic energies during successive seismic cycles illustrates the disordering effect of asperities and the build-up of the elastic energy during the strengthening phase. We interpret the rising E_h as the disordering process of asperities, that is the strong perturbation from the initial position which is supposed to be quenched in the system. The sticking phases correspond to a period of increase of E_h during which the asperities increase disordering, while a large scale event corresponds to the rapid decrease of E_h (re-ordering of the asperities). We note that during such a large scale event, while E_t drops significantly and returns to zero, the drop of E_h is only partially such that a disorder, and elastic energy, is still present after a large event. It implies that there is a memory effect over the cycles from the relative positions of the asperities.

We also observe a transient period at the beginning of the shearing where the evolution of E_h is similar for all experiments. As the normal stress is increased a larger level of E_h is reached in the system, so a larger disordering of the asperities. It implies that higher normal stress prevents the interface to come back to its initial state (with low E_h) even during a LSE and so maintains a larger disorder in the system with internal stresses along the interface at any time.

The process of synchronization has been well documented notably in numerical simulations and shows that only for forces larger than a critical force, that constitute a critical point, the system will become unstable and sliding will extend to all sites of the interface (Fisher et al., 1997; Tanguy et al., 1998; Kammer et al., 2015; de Geus et al., 2019; Albertini et al., 2021). This constitutes a depinning transition and this phenomenology leads to stick-slip. In such models, this critical force is linked to a critical length scale, L_c , of an initiating slip pulse, that will invade all the interface if its extension becomes larger than L_c . Most of these results were inferred from a homogeneous fault model. Here, both the evolution of the macroscopic force (Figure 9) and the distribution of slip events in Figure 14 are not in agreement with these predictions. Indeed, we first observe in Figure 9 that the macroscopic force required to propagate a full scale event is not perfectly constant but rather displays some fluctuations from one rupture to the other. Secondly, the distribution of event magnitudes (Figure 14) shows almost no gap between the largest avalanche and the whole interface avalanche. It, therefore, implies that avalanches of all sizes can exist in the system without necessarily leading above a certain size to a complete failure. In such a case one would expect a larger gap in event size between the maximum observed avalanche and the system wide event. Such different nucleation mode can arise in the heterogeneous system as interactions between arrested small events could exist and significantly modifies the process leading to a major rupture (Albertini et al., 2021). Interpreting these results in terms of fault mechanics suggests that creeping faults correspond to the interface with an asperity disorder and a strengthening regime with disordering of the interface by small destabilizing events that increase elastic interaction between asperities but without impacting the global fault loading.

5.3 Slip Intermittency

Our system is driven by a constant displacement rate for each experiment and we measure a macroscopic velocity of the PMMA plate that is indeed constant (except during a large-scale event, where a small but noticeable displacement step is observed). This macroscopic measurement mimics the measure that could be made around natural faults by geodetic instruments located at the surface, and thus necessarily far away from the slipping area at depth. It implies that such kind of measurement actually misses the actual complexity of the slip distribution taking place on the interface at a short time and spatial scale. Some fine measurements of the slip distribution in both time and space for

shallow creeping faults indeed reveal that the long term continuous creeping of faults is actually accommodated during bursts of aseismic slip of various sizes (Jolivet et al., 2013, 2015; Rousset et al., 2016; Khoshmanesh & Shirzaei, 2018). During slow slip events, the analysis of GPS signal in conjunction with the recording of low frequency earthquakes (LFEs) also reveals that the large scale motion along the slab consists in the superposition of numerous small slip episodes each acting for a limited duration (Frank, 2016; Frank & Brodsky, 2019). The analysis of LFEs as a proxy for local slip on the interface reveals as well that these slip episodes span a wide range of sizes and present both temporal and spatial correlation (Lengliné et al., 2017). All these results are well in agreement with the observations performed in this study where the interseismic slip on the fault is characterized by slip events (SEs) of different sizes that act in a close temporal relationship.

The slip events we characterized here are slow events in the sense that their duration with respect to their size is much lower than the Rayleigh wave speed of the material that constitutes the interface. Indeed, supposing a typical PMMA Rayleigh velocity of 1255 m/s (Gvirtzman & Fineberg, 2021), this would imply that in one time frame (1/29.97 s) a dynamic rupture front travels up to 42 m. This is inconsistent with the observations of SEs that last several time frames. If we suppose that most of the stress transfer between asperities is actually mediated by the silicone base embedding the PMMA beads, this gives a Rayleigh wave velocity of the order of 20 m/s, and then the propagation of a rupture front of 66 cm in one time frame. As the largest SEs have a typical duration of 0.3 s and cover a maximum area with a characteristic dimension of half the sample length (5 cm), this suggests that the SEs formed by our criterion actually correspond to slow events. It does not preclude local dynamic rupture to take place during such SEs, but their size might be limited to a single bead contact area (or smaller). This implies that the moment-duration scaling we report in Figure 15 should be interpreted as scaling attached to slow ruptures on the interface. The best-resolved trend shows $M_0 \propto T$ in agreement notably with the observations of (Ide et al., 2007) that show that many slow slip events on subduction zones follow this scaling law. We note however that the scaling in our experiment is only resolved over a restricted range of moments. This calls for future further experiments involving an increase in the number of beads and the sampling rate of the optical device. This moment-duration scaling is also in agreement with the observed evolution of the slip event characteristic distance with the square root

of duration. This, therefore, suggests that the slip events are driven by a diffusion process controlling the propagation of the rupture, similar to slow-slip events tracked with tremor migration (Ide, 2010).

The slip event, SEs are characterized as a single rupture following the clustering procedure we defined. It is not obvious how to select the merging condition which is imposed partially in our case by the acquisition rate of the optical device. However, what is the exact definition and extent of a slip event is not a question limited to our experiment. Indeed, the analysis of earthquakes for example, generally indicates that they are actually composed of several sub-events. The identification of these sub-events, therefore, questioned the definition of the earthquake rupture that consists of several connected local slip episodes. As we discussed above, the same problem of definition arises for a slow slip event which is actually made of a sum of local transient slip episodes connected in time and space. Decreasing the time interval required to merge individual asperity slips into the same cluster would ultimately lead to only isolated local slip events. On the opposite, increasing this time interval would lead to a single slip event comprising all the beads. Finally, we conclude that SEs are thus analyzed at the spatial and temporal scale imposed by our acquisition system which is a constraint imposed as well to observations made on natural fault systems.

5.4 Mechanics of the Strengthening Regime

Our system resolves confined rupture that takes place during the strengthening phase. This contrasts with most frictional setups where only large scale ruptures are analyzed during the weakening phase. Unlike these large scale ruptures that are largely controlled by the machine loading stiffness (Leeman et al., 2016; Wu & McLaskey, 2019), partial ruptures provide the opportunity to study the slip events taking place on an interface without being actually influenced by the loading system. In our system, the events are arrested because of stress heterogeneity that arises notably from the variable asperity heights creating spatial differences in frictional strengths. We stress that the heterogeneous nature of the interface only arises as a result of the topography and the position distribution of the asperities with respect to their initial position (assessed by the interfacial elastic energy E_h), but that there is no variation of the material properties that constitute the interface. In particular, it implies that the complex dynamic that we recovered during our experiment is not the result of a heterogeneous spatial distribution

of the a and b parameters of the rate-and-state friction model as employed in several simulations of faulting (Barbot et al., 2012). We note that such approaches are based on a continuum description of the interface and do not model the failure of individual asperities where locations in between are contact-free and hence have zero frictional strength like in our case.

Our results indicate that the strengthening phase, which could be seen as the preparatory phase of large ruptures, includes a population of events that are multi-scale in size (Gutenberg-Richter relation in Figure 14) and in duration (Figure 15). A similar multi-scale size distribution has also been reported by Nasuno et al. (1998) for the events that occurred during the strengthening phase along a sheared fault gouge layer simulated by spherical glass particles that are similar to our asperities. Such granular layers have also been numerically modeled by Aharonov and Sparks (2004), which evidenced a transition from weak to strong contacts accompanied by accelerating internal stress release of grains before large stick-slip events. It suggests that such a transition of localized contacts during the strengthening phase could be considered as a precursor for the impending large scale stick-slip. Combined with our results, it implies that the preparatory phase of large earthquakes is very long with many foreshocks strongly related to the quenched disorder. This result is highly reproducible with the same disorder in the asperity positions.

5.5 Limitations of the Experimental Setup

Our novel experimental setup builds a heterogeneous shear interface of multi-asperity contacts. An important point resulting from the designed configuration is that the elevated adhesion of the silicone block to the asperities is strong enough such that there is no rolling of asperities caused by the shearing imposed on the PMMA plate. Similarly, we also make sure that the silicone block is at no time in contact with the PMMA plate during the experiment. Indeed, in such a case, the high adhesion of the silicone would cause a local resistance to slip and modify the modeled physical process (from friction to adhesion). This limits the maximum normal load we can impose on the system to approximately 1500 N, at a higher imposed normal load, the silicone block starts to have some local contacts with the PMMA plate.

The sampling rate of the camera employed directly determines the time resolution for tracking the slips of asperities. Thus, the rapid slipping phase involving multiple asperities cannot be analyzed in detail. For example, it is not sampled with a high enough time resolution to capture a clear trend of the decay of the shear force as a function of slip during these episodes (see Figure 9). Furthermore, the precise timing, migration, or interactions of local bead slips during the high slipping phase is not accessible. Finally, as we evidence, the overall rupture during such SEs is slow but it does not preclude that locally during such slow transient, local dynamic rupture occurs such that some proportion of the resolved slip is actually taking place during such dynamic phase and radiate elastic wave. The proportion of the slip taking place on the asperities as dynamic events is presently not measurable but remains to be investigated for future studies.

The derivation of the moment, M_0 , of the slip events required the computation of an area, A_i , attached to each asperity (see Eq. 8). Here we take for each asperity the area returned by the Voronoi cell including the asperity. Such a definition of the slip area attached to an asperity probably over-estimate the real slipping area during an IAS. Indeed, the locked area of an asperity is presumably much lower than a circle of the asperity radius (considering a Hertz contact model) (K. L. Johnson, 1987). Although some slip deficit can extend beyond the fully locked area, it becomes negligible at a distance typically greater than one asperity radius (L. R. Johnson, 2010). It then leads to an over-estimation of the computed moment. However, as the contact area for each asperity should be nearly similar (considering again the Hertz contact model and the low stiffness of the silicone) we can expect that the conclusion of the magnitude distribution presented in Figure 14 would be unchanged if one could obtain a precise measurement of the slipping area of each IAS. We thus acknowledge that the reported moment of slip events should be mostly interpreted relatively than as absolute values. Such complexity of the slip distribution is also observed for natural earthquakes with zones of little or no slip (Freymueller et al., 2021).

Another ambiguity is involved in the calculation of the moment from equation (8). Indeed, the shear modulus used in this equation is taken as the shear modulus of the PMMA. However the PMMA is the dominant material only on one side of the system, the other side is composed of the PMMA beads embedded in the silicone block. Characterizing the shear modulus for such bi-material is not a trivial task and again further warns against a direct interpretation of the absolute values of M_0 .

6 Conclusions

This study analyzes the collective behavior of numerous discrete asperities ($N \approx 140$) modeled on an analog fault interface during multiple seismic cycles. We show that an interface composed of multiple discrete asperities can have a macroscopic behavior that is distinct from that of its individual elements. The asperities present a diversity of slips at various speeds. We evidence the dependency of the interseismic coupling of the interface with the topographical map of the asperity summits and the normal load imposed on the system. We notably show that topographic variations of the asperity summits have a pronounced effect on this coupling. The slip intermittency of the activity of clustered asperities indicates that the interface undergoes local episodes of creep that ultimately lead to the global slip of the interface. The analysis of the evolution of the elastic energy along the interface helps to track the disordering of the asperities with respect to their initial position. We show that this energy is typically higher for large normal stress, which supports the conclusion that normal stress maintains a larger disorder in the system. It shows as well that the disorder increases during the strengthening phase and is only partially reduced during large slip events. Significant statistical features of slip widely observed in natural faults are reproduced by our experiments like the Gutenberg–Richter law, Omori’s law, and the moment-duration scaling, suggesting that the obtained results can be extrapolated to natural fault systems.

Open Research

All data obtained in our experiments are available at <https://seafire.unistra.fr/d/807cc92c4a42474797c2/>.

Acknowledgments

We thank Alain Steyer for the technical support. We thank Satoshi Ide for the discussion. This work of the Interdisciplinary Thematic Institute GeoT, as part of the ITI 2021–2028 program of the University of Strasbourg, CNRS and Inserm, was supported by IdEx Unistra (ANR-10-IDEX- 0002), and by SFRI-STRAT’US project (ANR ANR-20-SFRI-001) under the framework of the French Investments for the Future Program. This work was also supported by the China Scholarship Council (CSC) grant 201906370056.

References

Aharonov, E., & Sparks, D. (2004). Stick-slip motion in simulated granular layers.

- 828 *Journal of Geophysical Research*, 109(B09306).
- 829 Albertini, G., Karrer, S., Grigoriu, M. D., & Kammer, D. S. (2021). Stochastic prop-
 830 erties of static friction. *Journal of the Mechanics and Physics of Solids*, 147,
 831 104242.
- 832 Aubry, J., Passelègue, F., Escartín, J., Gasc, J., Deldicque, D., & Schubnel, A.
 833 (2020). Fault stability across the seismogenic zone. *Journal of Geophysical*
 834 *Research: Solid Earth*, 125(8), e2020JB019670.
- 835 Barbot, S., Lapusta, N., & Avouac, J.-P. (2012). Under the hood of the earthquake
 836 machine: Toward predictive modeling of the seismic cycle. *Science*, 336(6082),
 837 707–710.
- 838 Baumberger, T., & Caroli, C. (2006). Solid friction from stick–slip down to pinning
 839 and aging. *Advances in Physics*, 55(3-4), 279–348.
- 840 Ben-David, O., Cohen, G., & Fineberg, J. (2010). The dynamics of the onset of fric-
 841 tional slip. *Science*, 330(6001), 211–214.
- 842 Ben-Zion, Y., & Sammis, C. G. (2003). Characterization of fault zones. *Pure and*
 843 *Applied Geophysics*, 160(3), 677–715.
- 844 Bhushan, B. (1998). Contact mechanics of rough surfaces in tribology: multiple as-
 845 perity contact. *Tribology Letters*, 4(1), 1–35.
- 846 Bürgmann, R., Kogan, M. G., Steblov, G. M., Hilley, G., Levin, V. E., & Apel, E.
 847 (2005). Interseismic coupling and asperity distribution along the Kamchatka
 848 subduction zone. *Journal of Geophysical Research*, 110(B07405).
- 849 Candela, T., Renard, F., Bouchon, M., Brouste, A., Marsan, D., Schmittbuhl, J.,
 850 & Voisin, C. (2009). Characterization of fault roughness at various scales:
 851 Implications of three-dimensional high resolution topography measurements.
 852 *Pure and Applied Geophysics*, 1817–1851.
- 853 Candela, T., Renard, F., Klinger, Y., Mair, K., Schmittbuhl, J., & Brodsky, E. E.
 854 (2012). Roughness of fault surfaces over nine decades of length scales. *Journal*
 855 *of Geophysical Research*, 117(B8), B08409.
- 856 Cattania, C., & Segall, P. (2021). Precursory slow slip and foreshocks on rough
 857 faults. *Journal of Geophysical Research: Solid Earth*, 126(4), e2020JB020430.
- 858 Chester, F. M., & Chester, J. S. (1998). Ultracataclasite structure and friction pro-
 859 cesses of the Punchbowl fault, San Andreas system, California. *Tectonophysics*,
 860 295(1-2), 199–221.

- 861 Chester, F. M., Evans, J. P., & Biegel, R. L. (1993). Internal structure and weak-
 862 ening mechanisms of the San Andreas fault. *Journal of Geophysical Research*,
 863 98(B1), 771–786.
- 864 Davies, E. R. (2005). *Machine vision: theory, algorithms, practicalities*. Elsevier.
- 865 de Geus, T. W., Popović, M., Ji, W., Rosso, A., & Wyart, M. (2019). How collec-
 866 tive asperity detachments nucleate slip at frictional interfaces. *Proceedings of*
 867 *the National Academy of Sciences*, 116(48), 23977–23983.
- 868 Dieterich, J. H. (1979). Modeling of rock friction: 1. experimental results and consti-
 869 tutive equations. *Journal of Geophysical Research*, 84(B5), 2161–2168.
- 870 Dieterich, J. H., & Kilgore, B. D. (1994). Direct observation of frictional contacts:
 871 New insights for state-dependent properties. *Pure and Applied Geophysics*,
 872 143(1), 283–302.
- 873 Dublanchet, P., Bernard, P., & Favreau, P. (2013). Interactions and triggering in
 874 a 3-D rate-and-state asperity model. *Journal of Geophysical Research: Solid*
 875 *Earth*, 118(5), 2225–2245.
- 876 Faulkner, D., Lewis, A., & Rutter, E. (2003). On the internal structure and mechan-
 877 ics of large strike-slip fault zones: field observations of the Carboneras fault in
 878 southeastern Spain. *Tectonophysics*, 367(3-4), 235–251.
- 879 Fisher, D. S., Dahmen, K., Ramanathan, S., & Ben-Zion, Y. (1997). Statistics of
 880 earthquakes in simple models of heterogeneous faults. *Physical Review Letters*,
 881 78(25), 4885.
- 882 Fortune, S. (1995). Voronoi diagrams and delaunay triangulations. *Computing in*
 883 *Euclidean Geometry*, 225–265.
- 884 Frank, W. B. (2016). Slow slip hidden in the noise: The intermittence of tectonic re-
 885 lease. *Geophysical Research Letters*, 43(19), 10–125.
- 886 Frank, W. B., & Brodsky, E. E. (2019). Daily measurement of slow slip from low-
 887 frequency earthquakes is consistent with ordinary earthquake scaling. *Science*
 888 *Advances*, 5(10), eaaw9386.
- 889 Freymueller, J. T., Suleimani, E. N., & Nicolsky, D. J. (2021). Constraints on the
 890 slip distribution of the 1938 mw 8.3 alaska peninsula earthquake from tsunami
 891 modeling. *Geophysical Research Letters*, 48(9), e2021GL092812.
- 892 Gan, G., Ma, C., & Wu, J. (2020). *Data clustering: theory, algorithms, and applica-*
 893 *tions*. SIAM.

- 894 Gao, H., Schmidt, D. A., & Weldon, R. J. (2012). Scaling relationships of source pa-
 895 rameters for slow slip events. *Bulletin of the Seismological Society of America*,
 896 *102*(1), 352–360.
- 897 Gent, A. N. (1958). On the relation between indentation hardness and Young’s mod-
 898 ulus. *Rubber Chemistry and Technology*, *31*(4), 896–906.
- 899 Goebel, T. H., Kwiitek, G., Becker, T. W., Brodsky, E. E., & Dresen, G. (2017).
 900 What allows seismic events to grow big?: Insights from b-value and fault
 901 roughness analysis in laboratory stick-slip experiments. *Geology*, *45*(9), 815–
 902 818.
- 903 Gutenberg, B., & Richter, C. F. (1944). Frequency of earthquakes in California. *Bul-
 904 letin of the Seismological Society of America*, *34*(4), 185–188.
- 905 Gvirtzman, S., & Fineberg, J. (2021). Nucleation fronts ignite the interface rupture
 906 that initiates frictional motion. *Nature Physics*, *17*(9), 1037–1042.
- 907 Hanks, T. C., & Kanamori, H. (1979). A moment magnitude scale. *Journal of Geo-
 908 physical Research*, *84*(B5), 2348–2350.
- 909 Harbord, C. W., Nielsen, S. B., De Paola, N., & Holdsworth, R. E. (2017). Earth-
 910 quake nucleation on rough faults. *Geology*, *45*(10), 931–934.
- 911 Hyndman, R. D., Yamano, M., & Oleskevich, D. A. (1997). The seismogenic zone of
 912 subduction thrust faults. *Island Arc*, *6*(3), 244–260.
- 913 Ide, S. (2010). Striations, duration, migration and tidal response in deep tremor.
 914 *Nature*, *466*(7304), 356–359.
- 915 Ide, S., Beroza, G. C., Shelly, D. R., & Uchide, T. (2007). A scaling law for slow
 916 earthquakes. *Nature*, *447*(7140), 76–79.
- 917 Jestin, C., Lengliné, O., & Schmittbuhl, J. (2019). Energy partitioning during sub-
 918 critical mode i crack propagation through a heterogeneous interface. *Journal of
 919 Geophysical Research: Solid Earth*, *124*(1), 837–855.
- 920 Johnson, K. L. (1987). *Contact mechanics*. Cambridge university press.
- 921 Johnson, L. R. (2010). An earthquake model with interacting asperities. *Geophysical
 922 Journal International*, *182*(3), 1339–1373.
- 923 Jolivet, R., Candela, T., Lasserre, C., Renard, F., Klinger, Y., & Doin, M.-P. (2015).
 924 The Burst-Like Behavior of Aseismic Slip on a Rough Fault: The Creeping
 925 Section of the Haiyuan Fault, China. *Bulletin of the Seismological Society of
 926 America*, *105*(1), 480–488.

- 927 Jolivet, R., Lasserre, C., Doin, M.-P., Peltzer, G., Avouac, J.-P., Sun, J., & Dailu,
 928 R. (2013). Spatio-temporal evolution of aseismic slip along the Haiyuan fault,
 929 China: Implications for fault frictional properties. *Earth and Planetary Science*
 930 *Letters*, *377*, 23–33.
- 931 Kammer, D. S., Radiguet, M., Ampuero, J.-P., & Molinari, J.-F. (2015). Linear elas-
 932 tic fracture mechanics predicts the propagation distance of frictional slip. *Tri-*
 933 *bology Letters*, *57*(3), 1–10.
- 934 Kanamori, H., & Anderson, D. L. (1975). Theoretical basis of some empirical re-
 935 lations in seismology. *Bulletin of the Seismological Society of America*, *65*(5),
 936 1073–1095.
- 937 Khoshmanesh, M., & Shirzaei, M. (2018). Multiscale dynamics of aseismic slip on
 938 central san andreas fault. *Geophysical Research Letters*, *45*(5), 2274–2282.
- 939 Lay, T., & Kanamori, H. (1981). An asperity model of large earthquake sequences.
 940 *Earthquake Prediction: An International Review*, *4*, 579–592.
- 941 Lay, T., Kanamori, H., & Ruff, L. (1982). The asperity model and the nature of
 942 large subduction zone earthquakes. *Earthquake Prediction Research*, *1*, 3–71.
- 943 Lee, D.-T., & Schachter, B. J. (1980). Two algorithms for constructing a delaun-
 944 nay triangulation. *International Journal of Computer & Information Sciences*,
 945 *9*(3), 219–242.
- 946 Leeman, J., Saffer, D., Scuderi, M., & Marone, C. (2016). Laboratory observa-
 947 tions of slow earthquakes and the spectrum of tectonic fault slip modes. *Nature*
 948 *Communications*, *7*(1), 1–6.
- 949 Lengliné, O., Elkhoury, J., Daniel, G., Schmittbuhl, J., Toussaint, R., Ampuero,
 950 J.-P., & Bouchon, M. (2012). Interplay of seismic and aseismic deformations
 951 during earthquake swarms: An experimental approach. *Earth and Planetary*
 952 *Science Letters*, *331*, 215–223.
- 953 Lengliné, O., Frank, W. B., Marsan, D., & Ampuero, J.-P. (2017). Imbricated slip
 954 rate processes during slow slip transients imaged by low-frequency earthquakes.
 955 *Earth and Planetary Science Letters*, *476*, 122–131.
- 956 Li, T., & Rubin, A. M. (2017). A microscopic model of rate and state friction evolu-
 957 tion. *Journal of Geophysical Research: Solid Earth*, *122*(8), 6431–6453.
- 958 Luo, Y., & Ampuero, J.-P. (2018). Stability of faults with heterogeneous friction
 959 properties and effective normal stress. *Tectonophysics*, *733*, 257–272.

- 960 Marone, C. (1998). Laboratory-derived friction laws and their application to seismic
961 faulting. *Annual Review of Earth and Planetary Sciences*, 26(1), 643–696.
- 962 McLaskey, G. C., & Glaser, S. D. (2011). Micromechanics of asperity rupture dur-
963 ing laboratory stick slip experiments. *Geophysical Research Letters*, 38(12),
964 L12302.
- 965 McLaskey, G. C., Thomas, A. M., Glaser, S. D., & Nadeau, R. M. (2012). Fault
966 healing promotes high-frequency earthquakes in laboratory experiments and on
967 natural faults. *Nature*, 491, 101–104.
- 968 Mitchell, T., & Faulkner, D. (2009). The nature and origin of off-fault damage
969 surrounding strike-slip fault zones with a wide range of displacements: A field
970 study from the Atacama fault system, northern Chile. *Journal of Structural*
971 *Geology*, 31(8), 802–816.
- 972 Morad, D., Sagy, A., Tal, Y., & Hatzor, Y. H. (2022). Fault roughness controls slid-
973 ing instability. *Earth and Planetary Science Letters*, 579, 117365.
- 974 Moreno, M. S., Bolte, J., Klotz, J., & Melnick, D. (2009). Impact of megathrust
975 geometry on inversion of coseismic slip from geodetic data: Application to the
976 1960 Chile earthquake. *Geophysical Research Letters*, 36(L16310).
- 977 Nadeau, R. M., & Johnson, L. R. (1998). Seismological studies at Parkfield VI:
978 Moment release rates and estimates of source parameters for small repeating
979 earthquakes. *Bulletin of the Seismological Society of America*, 88(3), 790–814.
- 980 Nasuno, S., Kudrolli, A., Bak, A., & Gollub, J. P. (1998). Time-resolved studies of
981 stick-slip friction in sheared granular layers. *Physical Review E*, 58(2), 2161–
982 2171.
- 983 Perfettini, H., Avouac, J.-P., Tavera, H., Kositsky, A., Nocquet, J.-M., Bondoux, F.,
984 ... others (2010). Seismic and aseismic slip on the Central Peru megathrust.
985 *Nature*, 465(7294), 78–81.
- 986 Pohrt, R., & Popov, V. L. (2012). Normal contact stiffness of elastic solids with frac-
987 tal rough surfaces. *Physical Review Letters*, 108(10), 104301.
- 988 Power, W., Tullis, T., Brown, S., Boitnott, G., & Scholz, C. (1987). Roughness of
989 natural fault surfaces. *Geophysical Research Letters*, 14(1), 29–32.
- 990 Romanet, P., Bhat, H. S., Jolivet, R., & Madariaga, R. (2018). Fast and slow slip
991 events emerge due to fault geometrical complexity. *Geophysical Research Let-*
992 *ters*, 45(10), 4809–4819.

- 993 Rousset, B., Jolivet, R., Simons, M., Lasserre, C., Riel, B., Milillo, P., ... Renard,
 994 F. (2016). An aseismic slip transient on the north anatolian fault. *Geophysical*
 995 *Research Letters*, *43*(7), 3254–3262.
- 996 Ruff, L., & Kanamori, H. (1983). The rupture process and asperity distribution
 997 of three great earthquakes from long-period diffracted P-waves. *Physics of the*
 998 *Earth and Planetary Interiors*, *31*(3), 202–230.
- 999 Ruina, A. (1983). Slip instability and state variable friction laws. *Journal of Geo-*
 1000 *physical Research*, *88*(B12), 10359–10370.
- 1001 Schmittbuhl, J., Chambon, G., Hansen, A., & Bouchon, M. (2006). Are stress dis-
 1002 tributions along faults the signature of asperity squeeze? *Geophysical Research*
 1003 *Letters*, *33*(13).
- 1004 Schmittbuhl, J., Gentier, S., & Roux, S. (1993). Field measurements of the rough-
 1005 ness of fault surfaces. *Geophysical Research Letters*, *20*(8), 639–641.
- 1006 Schmittbuhl, J., & Måløy, K. J. (1997). Direct observation of a self-affine crack
 1007 propagation. *Physical Review Letters*, *78*(20), 3888–3891.
- 1008 Schmittbuhl, J., Schmitt, F., & Scholz, C. (1995). Scaling invariance of crack sur-
 1009 faces. *Journal of Geophysical Research*, *100*(B4), 5953–5973.
- 1010 Schmittbuhl, J., Vilotte, J.-P., & Roux, S. (1996). A dissipation-based analysis of
 1011 an earthquake fault model. *Journal of Geophysical Research*, *101*(B12), 27741–
 1012 27764.
- 1013 Scholz, C. (2019). *The mechanics of earthquakes and faulting*. Cambridge University
 1014 Press.
- 1015 Scholz, C., & Campos, J. (1995). On the mechanism of seismic decoupling and back
 1016 arc spreading at subduction zones. *Journal of Geophysical Research*, *100*(B11),
 1017 22103–22115.
- 1018 Scholz, C., & Campos, J. (2012). The seismic coupling of subduction zones revisited.
 1019 *Journal of Geophysical Research*, *117*(B05310).
- 1020 Schulz, S. E., & Evans, J. P. (2000). Mesoscopic structure of the Punchbowl Fault,
 1021 Southern California and the geologic and geophysical structure of active strike-
 1022 slip faults. *Journal of Structural Geology*, *22*(7), 913–930.
- 1023 Selvadurai, P. A., & Glaser, S. D. (2015). Laboratory-developed contact models con-
 1024 trolling instability on frictional faults. *Journal of Geophysical Research: Solid*
 1025 *Earth*, *120*(6), 4208–4236.

- 1026 Selvadurai, P. A., & Glaser, S. D. (2017). Asperity generation and its relationship to
 1027 seismicity on a planar fault: A laboratory simulation. *Geophysical Journal In-*
 1028 *ternational*, 208(2), 1009–1025.
- 1029 Stierman, D. J. (1984). Geophysical and geological evidence for fracturing, water cir-
 1030 culation and chemical alteration in granitic rocks adjacent to major strike-slip
 1031 faults. *Journal of Geophysical Research*, 89(B7), 5849–5857.
- 1032 Subarya, C., Chlieh, M., Prawirodirdjo, L., Avouac, J.-P., Bock, Y., Sieh, K., ...
 1033 McCaffrey, R. (2006). Plate-boundary deformation associated with the great
 1034 Sumatra–Andaman earthquake. *Nature*, 440(7080), 46–51.
- 1035 Sutton, M. A., Orteu, J. J., & Schreier, H. (2009). *Image correlation for shape, mo-*
 1036 *tion and deformation measurements: basic concepts, theory and applications*.
 1037 Springer Science & Business Media.
- 1038 Tanguy, A., Gounelle, M., & Roux, S. (1998). From individual to collective pinning:
 1039 Effect of long-range elastic interactions. *Physical Review E*, 58(2), 1577.
- 1040 Utsu, T., Ogata, Y., & S. Matsu’ura, R. (1995). The centenary of the Omori formula
 1041 for a decay law of aftershock activity. *Journal of Physics of the Earth*, 43(1),
 1042 1–33.
- 1043 Wu, B. S., & McLaskey, G. C. (2019). Contained laboratory earthquakes rang-
 1044 ing from slow to fast. *Journal of Geophysical Research: Solid Earth*, 124(10),
 1045 10270–10291.
- 1046 Yuen, H., Princen, J., Illingworth, J., & Kittler, J. (1990). Comparative study of
 1047 hough transform methods for circle finding. *Image and Vision Computing*,
 1048 8(1), 71–77.
- 1049 Zhou, X., He, Y., & Shou, Y. (2021). Experimental investigation of the effects of
 1050 loading rate, contact roughness, and normal stress on the stick-slip behavior of
 1051 faults. *Tectonophysics*, 816, 229027.

Collective behavior of asperities before large stick-slip events

Weiwei Shu¹, Olivier Lengliné¹, Jean Schmittbuhl¹

¹EOST/ITES, Université de Strasbourg/CNRS, France

Key Points:

- We propose a novel direct-shear setup to observe the collective behavior of asperities along an analog fault interface during stick-slips
- Scaling laws, that mimic those of slow slip events, are observed in our experiments and originate during the fault-strengthening phase
- Large scale quenched topography of the asperities along the interface has a direct impact on the interseismic coupling

Corresponding author: Weiwei Shu, w.shu@unistra.fr

Abstract

The multi-scale roughness of a fault interface is responsible for multiple asperities that establish a complex and discrete set of real contacts. Since asperities control the initiation and evolution of the fault slip, it is important to explore the intrinsic relationships between the collective behavior of local asperities and the frictional stability of the global fault. Here we propose a novel analog experimental approach, which allows us to capture the temporal evolution of the slip of each asperity on a faulting interface. We find that many destabilizing events at the local asperity scale occurred in the frictional strengthening stage which is conventionally considered as the stable regime of a fault. We compute the interseismic coupling to evaluate the slipping behaviors of asperities during the fault-strengthening stage. We evidence that the interseismic coupling can be affected by the elastic interactions between asperities through the embedding soft matrix. Scaling laws of natural slow slip events are reproduced by our setup in particular the moment-duration scaling. We also evidence an unexpected persistency of a disordering of the asperities through the seismic cycles despite the relaxation effects of the large slip events.

Plain Language Summary

Earthquakes are the results of a slip along a rough fault on which a complex and discrete set of asperities establish the interfacial contacts and control the frictional stability of the fault. We propose a novel experimental setup capable of measuring directly the subtle motion of individual asperities on an analog faulting interface. By capturing the temporal evolution of the slip of each asperity, we link the mechanical behavior of the global fault with the collective behavior of local asperities. Many destabilizing events at the local asperity scale are found during the globally stable stage of the fault. We prove that the interseismic coupling of asperities is affected by the normal load, the peak height of asperities, and the interactions between asperities. The spatiotemporal interactions of asperities are quantified as slip episodes to mimic the ruptures including both stable and unstable slips. With the catalog of slip episodes, we reproduce the significant characteristics and scaling laws observed in natural faults, such as the magnitude-frequency distribution and the moment-duration scaling. Such upscaling suggests that our results can be extrapolated to natural faults and provide insights into fault physics and mechanics.

1 Introduction

Crustal fault interfaces display geological heterogeneities at various scales (Faulkner et al., 2003; Chester et al., 1993; Ben-Zion & Sammis, 2003). In particular, exhumed fault surfaces exhibit a complex topography characterized by height variations at all scales (Candela et al., 2009, 2012; Power et al., 1987; Schmittbuhl et al., 1993, 1995; Scholz, 2019). Supposing that the roughness of these interfaces is similar to those of active faults at depth, it implies that the frictional interface is formed by a complex set of junctions across the two opposite surfaces in contact (Schmittbuhl et al., 2006; Pohrt & Popov, 2012). These junctions are commonly known as asperities (Bhushan, 1998). They have been characterized at the laboratory scale as microcontacts (Dieterich & Kilgore, 1994) where the resistance to an imposed shear stress is shown to be governed by the initiation and evolution of the fault slip (Scholz, 2019).

The presence of these asperities on the fault is supported by the observation of small repeating earthquakes, supposedly representing cohesive zones that fail periodically under constant loading (Nadeau & Johnson, 1998). The role of such asperities in the behavior of earthquakes has long been recognized. For example, it is suggested that small and scattered asperities on a subduction interface may lead only to a minor release of the seismic moment (Ruff & Kanamori, 1983). On the other hand, a great earthquake may involve the simultaneous rupture of multiple asperities, such as the 1960 M_W 9.5 Chile earthquake (Moreno et al., 2009) or the 2004 M_W 9.2 Sumatra-Andaman earthquake (Subarya et al., 2006). Such examples have been interpreted in a framework drawing a strong link between the rupture synchronization of asperities and the magnitude of the impending earthquake (Lay & Kanamori, 1981; Lay et al., 1982). This synchronization of asperities actually emphasizes a strong time-and-space dependent mechanism for the underlying physics and corresponding mechanical response of fault slip. The role of asperities on the behavior of the faulting interface is not limited to dynamic rupture events. Indeed, the interseismic phase is also strongly impacted by the presence of such strong contact areas. This notably arises as locked patches can create stress shadows which lead to reduced interseismic slip rates on the surroundings of the asperity (Bürgmann et al., 2005) and thus a spatial modulation of the interseismic coupling (Perfettini et al., 2010).

Numerical models have addressed the behavior of a fault interface comprising multiple asperities. A number of simulations represent the interface notably in the context of the rate-and-state friction framework (Dieterich, 1979; Ruina, 1983; Marone, 1998) and asperities are presented as distinct patches spatially distributed over the fault plane with distinct frictional parameters (Barbot et al., 2012; Dublanche et al., 2013; Luo & Ampuero, 2018; Li & Rubin, 2017). In these numerical models, the asperities are usually considered as velocity weakening patches and are therefore defined to be potentially unstable. These models indicate that the mechanical response of a fault is evidently affected by the interactions of discrete asperities surrounded by aseismic creep areas. For instance, a variable density of asperities (Dublanche et al., 2013), which is the ratio between the total area covered by asperities and the total area of the fault plane is proposed and utilized to explain at which condition the fault will be ruptured entirely or locally. Incorporating roughness on the fault plane (as fluctuations of the normal stress), Cattania and Segall (2021) show that this heterogeneity modulates the slip stability across the fault. Finally, Romanet et al. (2018) demonstrate that the sliding diversity of a fault can be obtained from geometrical complexities alone, without the need for the complexity of the friction law. All these numerical approaches, therefore, point to the importance of these asperities and their interactions in controlling fault mechanics. However, these models are severely limited by the computational cost of simulating heterogeneities with a variable size over a large time and space domain and inherently only describe a limited aspect of the ongoing physics.

At the laboratory scale, numerous experiments on rock samples have also shown that fault roughness plays a crucial role in fault slip behavior (Goebel et al., 2017; Harbord et al., 2017; Morad et al., 2022; Zhou et al., 2021) as it controls actual stress conditions at contacting asperities (Aubry et al., 2020). These results imply that the stress heterogeneity at local asperities is significant for influencing fault slip behavior. However, these experiments usually analyze the effects of asperities by comparing the initial and final roughness of the fault interface as the nontransparent rock slabs cannot provide the possibility to capture what is happening on the interface during the fault slip process. On the contrary, some other experiments take advantage of the transparency of analog materials (e.g., Poly-methyl-methacrylate, PMMA) to optically observe the asperities distributed on the interface (Lengliné et al., 2012; Jestin et al., 2019; Selvadurai & Glaser, 2015, 2017), which provides a possibility for the direct monitoring of the

107 faulting interface. Although the contacts were captured during these experiments, it was
 108 not possible to track the slip at each point during shearing.

109 Here we present a novel experimental setup that aims at capturing the slip as a func-
 110 tion of time for each asperity on a sheared interface. Our experimental setup is much
 111 simpler than a complex fault zone system, which has no mineralogy, no fluid, and no chem-
 112 ical transformation, but the fundamental process of interest, the relationship between
 113 the collective behavior of local asperities and the stability regime of the global fault sys-
 114 tem, remains similar. Specifically, this novel experimental approach allows a thick trans-
 115 parent PMMA plate to slide slowly on a customized surface with height variations, on
 116 which asperities are modeled by numerous identical spherical PMMA beads embedded
 117 in a softer polymer base. Thanks to a high-resolution camera, our setup is capable of
 118 measuring directly the subtle motion of local asperities on the interface during the whole
 119 slipping process, which helps to understand the time-and-space dependent behavior of
 120 each single asperity. The mechanical response of the global fault system is well recorded
 121 and explained through the collective behavior of local asperities. The link between the
 122 fault topography and the interseismic coupling is also investigated. In addition, the spatio-
 123 temporal interactions of asperities are quantified as collective slip episodes mimicking
 124 fault ruptures including both stable and unstable slips. To give some geophysical impli-
 125 cations, the effective upscaling from the analog interface to natural faults is demonstrated
 126 by reproducing significant characteristics and scaling-laws observed in natural fault sys-
 127 tems.

128 **2 Experimental Setup**

129 We build an analog model of a shear interface that aims at reproducing the typ-
 130 ical mechanical structure of a natural fault core. We consider that a fault zone consists
 131 of several key elements. At the interface, the roughness of the fault topography creates
 132 contacts on a number of discrete sites, i.e. asperities, that are here modeled as PMMA
 133 beads. The core of the fault, which consists generally in a heavily fractured medium (Chester
 134 & Chester, 1998; Schulz & Evans, 2000) is represented in our setup with a soft material
 135 surrounding the PMMA beads. At a greater distance from the fault, the number of dam-
 136 age decreases (Ben-Zion & Sammis, 2003; Mitchell & Faulkner, 2009; Stierman, 1984),
 137 and the fault becomes stiffer which translates in our setup in a rigid base attached to
 138 the soft material (Figure 1). The asperities are in contact with a top rigid block and es-

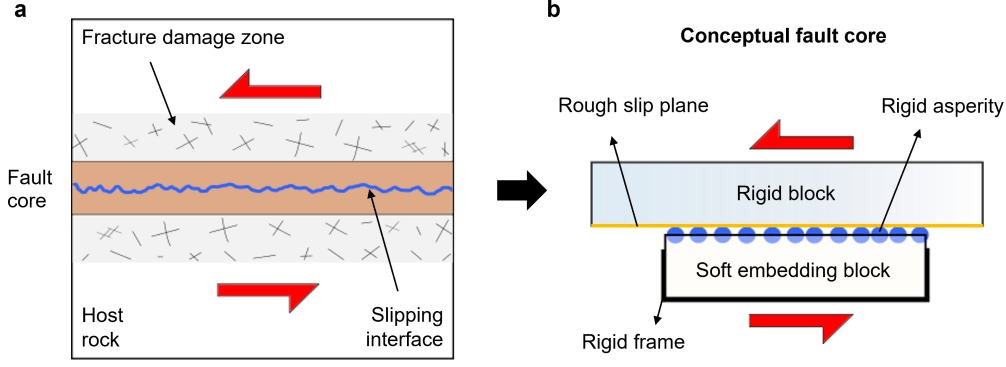


Figure 1. a: Sketch of a typical natural fault zone showing a rough frictional slipping interface subjected to shear. b: Conceptual model of the analog shear interface derived from the natural fault core structure. The rigid asperities embedded in the soft thick block establish a rough slip plane beneath the top rigid block.

establish a rough slip plane, while the soft embedding block fixed within the bottom rigid frame is easily deformed. This thick, rough, and deformable interface allows us to study the interactions of asperities and their collective behavior with respect to the frictional stability of the fault interface.

2.1 Sample Preparation and Characterization

To prepare such a model of multi-asperity contact, numerous identical spherical PMMA beads (a total number of 175) with a radius R of 3 mm are embedded in a soft block. The soft block is composed of silicone (BLUESIL RTV 3428 A&B product from the Elkem company), with dimensions $10 \times 10 \times 3.0$ cm. The preparation of the sample consists in first pouring a thin layer (of the thickness of a bead radius) of edible gelatin mixed with water at the bottom of a mold. Then PMMA beads are dropped randomly in this layer all over the interface. After the gelatin layer solidifies, we then pour the liquid silicon into the mold to cover the beads and wait for at least 24 hours at room temperature for its solidification. Finally, we take out the upside-down sample and remove the mixture of gelatin and water. Following the procedures above, we customize an experimental sample and its picture is displayed in Figure 2. The resulting sample is made such that all beads have nearly the same height while being scattered randomly over the sample. Physical characteristics of the silicone are derived from the technical datasheet,

the relation of Gent (1958) for converting durometer values to Young’s modulus, and laboratory measurements of the P-wave velocity of the material. We obtain a P-wave velocity for this material of 1000 m/s, an S-wave velocity of 19 m/s, a Young’s modulus of 1.1 MPa, and a density of 1100 kg/m³.

In order to precisely describe the so-formed interface and get the summit heights of all the beads, we measure a high-resolution topographical map for the interface. The data are acquired by a digital microscope profiler (RH-2000, HIROX) and a non-contact Nano Point Scanner (NPS, HIROX). The system uses a white light confocal LED beam with grids of 28 μm and 100 μm in the x - and y -directions, respectively. The topographical map of the interface is shown in Figure 3a, where the blueish part indicates the embedding silicone block while the discrete circles represent the asperities with different heights. We determine the peak heights of all the asperities (Figure 3b) and statistically analyze their distribution (Figure 3c). The peak heights of asperities (relative to the average silicone upper face level) range from 1.31 mm to 3.15 mm, with most of them within the peak height interval [1.4, 2.6]. The average peak height is 2.02 mm and the standard deviation of the peak heights is 0.39 mm, which indicates a small variance in the peak heights of asperities. We notice that there is a large-scale trend across the entire sample of this peak bead height. This is most likely due to the non-perfect planarity of the gelatin layer. Removing this large-scale trend, we observe that the height difference between neighboring asperities is low. In addition, we compute the average peak height difference between two asperities as a function of the distance in x and y direction (Figure 3d). We find a pattern highlighting the large scale variation of the peak height but no other correlation of the peak heights emerges.

2.2 Mechanical Loading

To simulate a large-scale, far-field, loading imposed on a fault, the shear of the whole analog interface system is induced by imposing a small displacement rate to the PMMA plate under well-controlled normal loads (Figure 2). PMMA has been widely used, as an analog material, to simulate numerous mechanical processes taking place within the Earth. In particular, frictional processes taking place on natural faults have been investigated using this material, such as fault creep and nucleation phases (e.g., McLaskey & Glaser, 2011; McLaskey et al., 2012; Selvadurai & Glaser, 2015) but also ruptures (e.g., Ben-David et al., 2010; Gvirtzman & Fineberg, 2021; Schmittbuhl & Måløy, 1997). Due

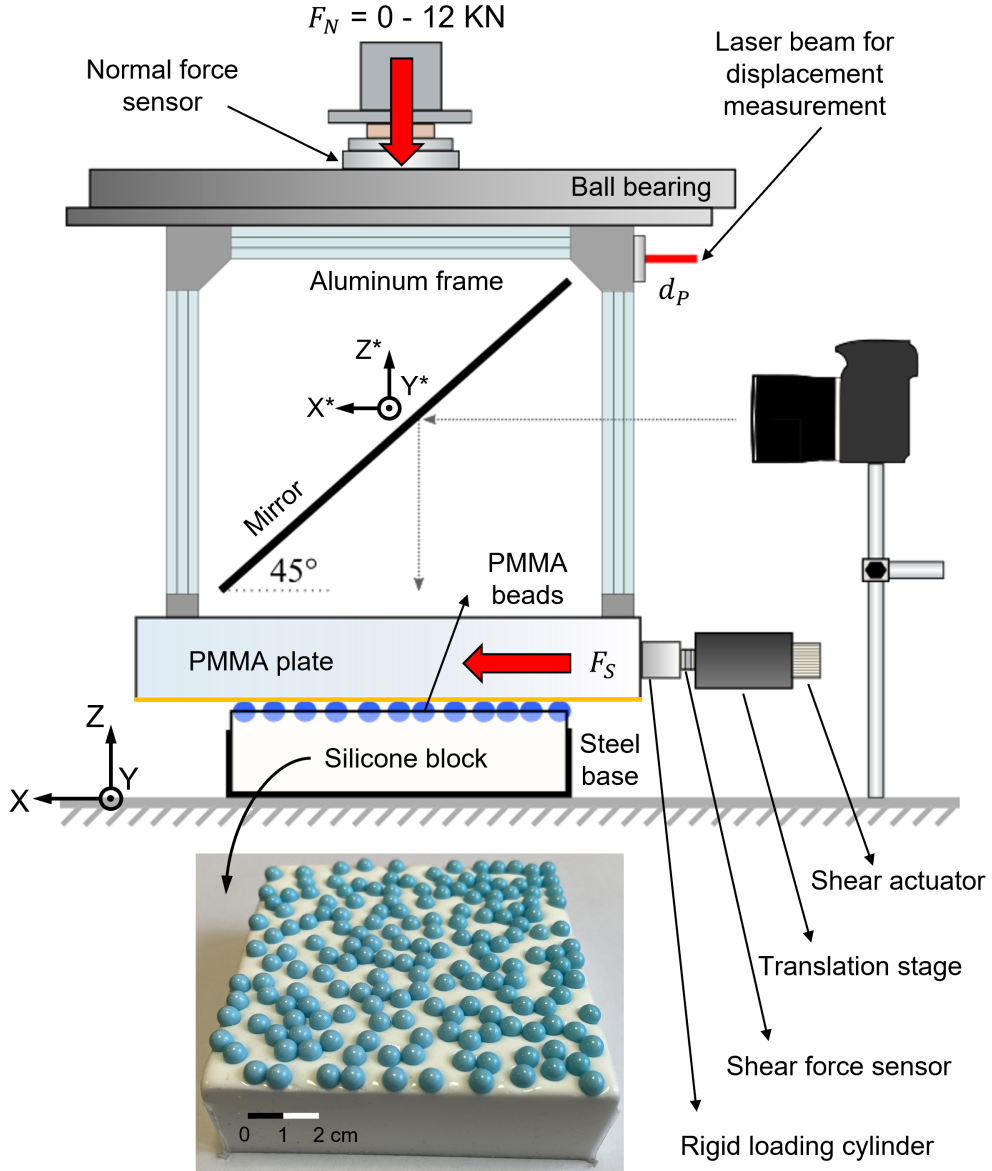


Figure 2. Schematic diagram of the technical experimental setup (side view). The normal force, F_N , and shear force, F_S , are measured by their corresponding sensors. A laser is employed to measure the displacement of the PMMA plate, d_P . A high-resolution camera is utilized with a mirror to monitor the positions of the PMMA beads during the whole shear process. Two axis systems, one attached to the ground and another one attached to the mirror, are represented. The yellow line indicates a rough slip plane established between the PMMA plate and the PMMA beads. The inset shows an image of the PMMA beads embedded in the soft silicone block.

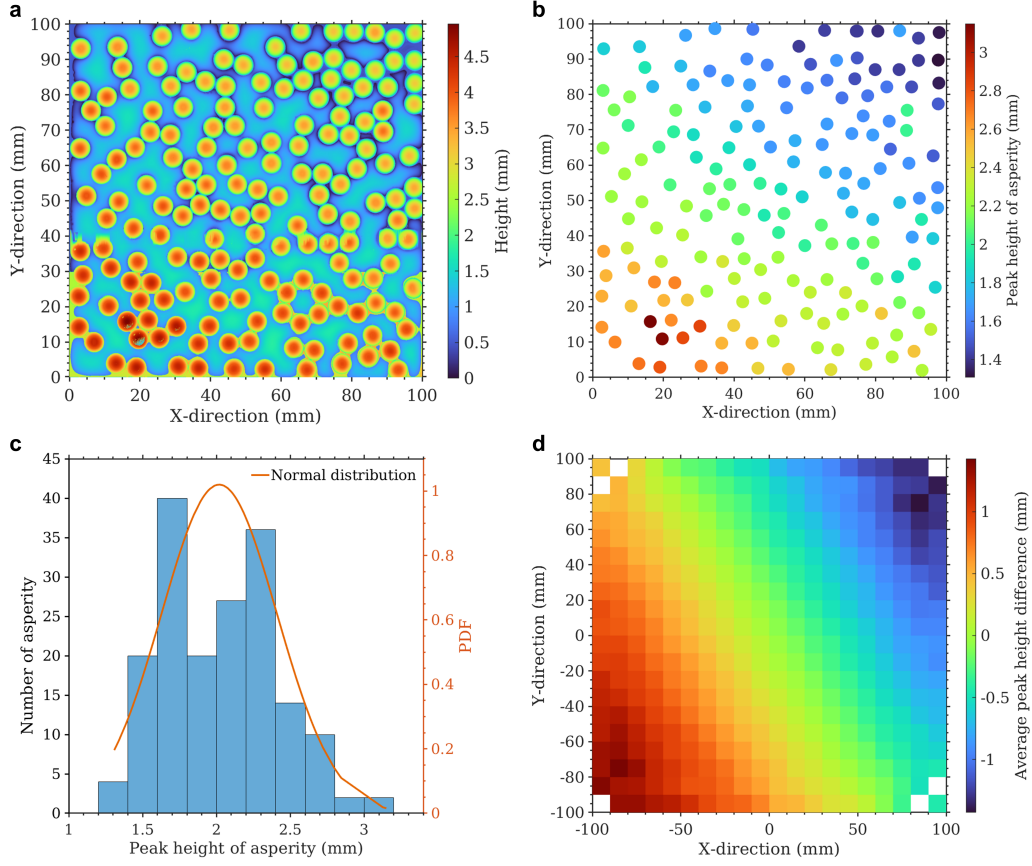


Figure 3. a: Topographical map of the analog fault interface. The blueish part is the embedding silicone block while the colored circles are the asperities created by the PMMA beads. There are a few non-measured points in the bottom-left corner that have little effect on characterizing the interface. b: Peak height of each asperity. The minimum and the maximum are 1.31 mm and 3.15 mm, respectively. c: Distribution of the peak heights of all the asperities. The asperities with peak heights ranging from 1.4 to 2.6 mm account for the majority. A standard deviation of 0.39 mm indicates a small variance in the peak heights. d: Average peak height difference as a function of the x and y direction. This highlights the large scale variation of the peak heights.

to its transparency, the PMMA enables a clear direct observation of the deforming medium (Lengliné et al., 2012; Jestin et al., 2019). The shear modulus of the PMMA is estimated as 2277.1 MPa (Selvadurai & Glaser, 2015).

The normal force F_N is applied by the vertical movement of the rigid load platen driven by a high-precision micro stepper motor (LoadTrac II), and uniformly transferred to the PMMA plate through the ball bearing and the rigid aluminum frame. A sensor of resolution 0.01 N is utilized to record the normal force and maintain a constant normal load throughout the whole duration of an experiment. We run the shear actuator, a combination of servo and stepper motor, with a constant displacement rate V_S to drive the translation stage and the rigid loading cylinder to impose the shear force F_S while maintaining a normal force F_N on the PMMA plate. The loading cylinder is composed of the aluminium alloy 2017A, with a stiffness of 78 N/ μm . The shear force F_S is measured using a sensor placed between the cylinder and the translation stage, with a resolution of 0.01 N. The stiffness of this sensor is 1 N/ μm , thus most of the loading stage deformation is actually taking place within the force sensor. We employ a laser (Keyence IL-S025), range 10 mm and resolution 0.1 μm , to measure the displacement of the PMMA plate, d_P (Figure 2). For all the experiments, we keep the initial value of d_P the same to ensure each fault slip starts from the same position.

Prior to performing the experiments, we fix the PMMA plate to the aluminum frame and attach the silicone block to the rigid steel base and clamp it. We use a digital level to make sure that the whole experimental system, especially the slip plane, is flat horizontal. Each experiment begins at the moment when the shear force starts to increase on the PMMA plate, given the analog fault has been previously loaded by a stable normal load. The duration of each experiment is set to 600 s. We performed 28 experiments by applying various normal loads ranging from 10 N to 1000 N and displacement rates ranging from 5.0 $\mu\text{m/s}$ to 15.0 $\mu\text{m/s}$ (Table S1). We define the x-direction as the sliding direction of the PMMA plate while the direction y is set perpendicular to the x-direction.

To demonstrate the transition from steady slip to stick-slip in our analog fault system, the evolution of the shear force, F_S , under multiple normal loads, F_N , maintaining the same loading rate V_S of 5.0 $\mu\text{m/s}$ is presented in Figure 4. We clearly observe the steady sliding of the interface when the normal load is quite small (e.g., $F_N = 10$ N). On the other hand, multiple stick-slips are observed when the normal load becomes greater

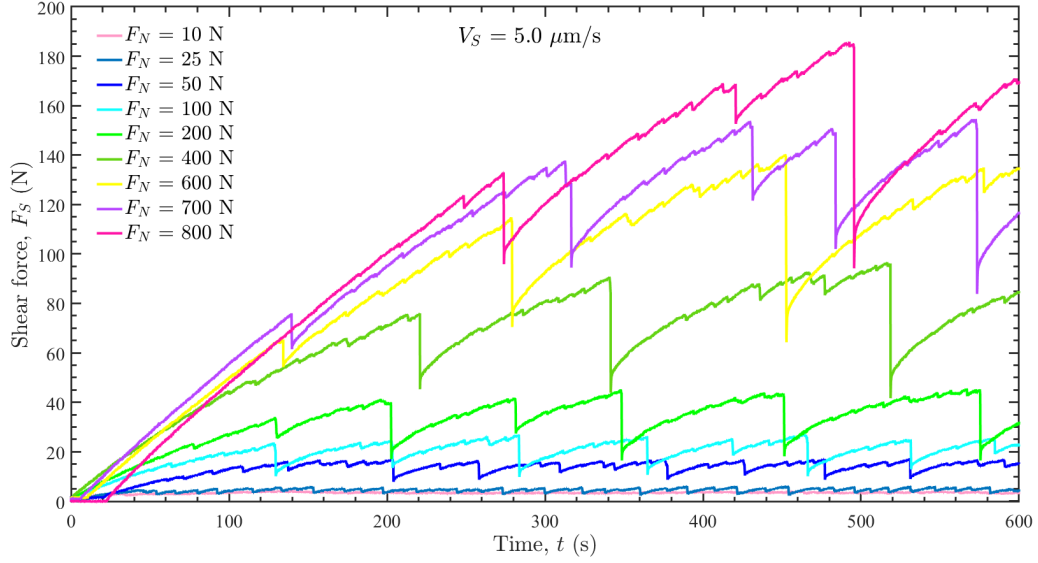


Figure 4. Temporal evolution of the shear force under multiple normal loads. The interface slips steadily when the normal load is quite small while evident stick-slips occur when the normal load becomes greater than 50 N. With the increase of the normal load, the shear force drop also increases.

than 50 N (Figure 4). In addition, the shear force drop of each stick-slip increases with the increase of the normal load.

2.3 Optical Monitoring

To capture the positions of asperities and compute their slips during the experiments, we use a high-resolution camera (Nikon D800) with a lens (Nikon 105mm f/2.8D AF Micro-Nikkor) in automatic focus mode to record videos. A mirror fixed inside the aluminum frame, which is inclined at 45 degrees, reflects the interface and moves with the sliding of the PMMA plate during the experiments (Figure 2). The main settings of the optical system are as follows: aperture size f/14, exposure time 1/30 s, and photosensitivity (ISO) 100. Two LED lights are placed behind the camera to supplement sufficient light for the clear observation of the interface. We record videos of dimensions in 1920×1080 pixels with a sampling rate of 29.97 frames per second. In addition, to synchronize the force measurement and the optical monitoring, we send an electrical synchronization signal and correct the time base of each record.

For each experiment, we extract all pictures taken by the camera between the times t_0 and t_f which are respectively the times at the beginning and the end of an experiment. From this set of pictures, we extract the slip of each individual asperity as a function of time. Denoting $x_i(t)$ and $y_i(t)$ the positions of the center of asperity i in a fixed reference frame (attached to the ground) we can define the displacement, $d_i(t)$, of an asperity along the loading direction in this fixed frame,

$$d_i(t) = x_i(t) - x_i(t_0). \quad (1)$$

Similarly, we define $x_P(t)$ as the position of the center of the mirror in the same fixed frame and then its displacement (which corresponds to the displacement of the PMMA plate as well), is computed as:

$$d_P(t) = x_P(t) - x_P(t_0). \quad (2)$$

The cumulative slip of asperity i at time t is defined as the difference of the displacement between the two sides of the interface (i.e., the asperity and the PMMA plate):

$$u_i(t) = d_i(t) - d_P(t). \quad (3)$$

As the camera and the silicone block are both fixed to the ground while the mirror moves with the sliding PMMA plate, the position of each asperity, i , on pictures taken by the camera is relative to the moving frame of the mirror and is noted $(x_i^*(t), y_i^*(t))$. It follows that the displacement of an asperity in this moving frame is simply $d_i^*(t) = x_i^*(t) - x_i^*(t_0)$. From the definition of the cumulative slip introduced before, this displacement, $d_i^*(t)$, corresponds exactly to the cumulative slip, $u_i(t)$ of asperity i . Consequently, the cumulative slip of each asperity is obtained by tracking the evolution of its position, $x_i^*(t)$, between time t_0 and time t_f .

We developed a two steps procedure for tracking the evolution of the position $x_i^*(t)$ of each asperity i in the moving frame of the mirror. In the first step, we applied the circular Hough transform algorithm implemented within MATLAB for automatically detecting circular objects (Yuen et al., 1990; Davies, 2005). From the first and last pictures at times t_0 and t_f respectively, we extract the initial position $x_i^*(t_0)$ and final position $x_i^*(t_f)$ of asperity i . We also estimate the initial position of the beads, $y_i^*(t_0)$ in the direction perpendicular to the slip direction.

The initial positions of asperities detected at time t_0 are shown in Figure 5. The asperities marked by red circles, with a total number of $N = 144$, are retained in our

analysis while the asperities with blue markers are excluded from the subsequent image analysis because they are located too close to one of the image edges. We note the value of N may change with different experiments mainly due to the field view of the camera, but it fluctuates around 140. In addition, we obtain the radius R , which is 36 pixels, and compute the scaling of the image from the known radius of the PMMA beads ($R = 3$ mm), 12 pixels/mm. Based on the initial and final positions of asperities, we are able to estimate the total slip $u_i^*(t_f) = x_i^*(t_f) - x_i^*(t_0)$ of each asperity. Due to the constant loading rate, a simple linear trend between these two positions gives an approximate position, $x_i^*(t)$ of asperity i at each time step. This provides a first order estimate of each asperity location during the experiment. In the second step, in order to obtain the most accurate locations, we applied an image correlation technique (Sutton et al., 2009) to refine these first measurements.

To quantify the slip of each asperity, a square window for image correlation with a size of $\sqrt{2}R$ is defined at the center of each asperity based on our previous estimates of $x_i^*(t)$ and $y_i^*(t_0)$. We extract the image defined by the square correlation window of each asperity at all frames. For each asperity, we compute the FFT (fast Fourier transform)-based two-dimensional cross-correlation between the extracted window defined at time t_k and the window defined at time t_{k-1} . From the correlation map, we isolate the position of the maximum value which gives the displacement of the bead. We then shift the correlation window of the second frame based on this displacement and repeat the procedure until the computed displacement is null. At this last stage, we then extract a sub-sample displacement by interpolating the correlation map around its maximum. The final displacement of the bead between the two time frames is then obtained by summing all displacements computed during this iterative process. Repeating this procedure for all time frames and for each bead we are able to obtain the cumulative slip of each asperity during the whole duration of an experiment. The typical resolution of the resolved displacement in each direction is of the order of 0.01 mm.

Due to the geometry of our experimental setup, the non-parallelism which may result from the non-perfect 45 degree inclination of the mirror and/or the non-parallel view between the camera lens and the slip plane (Figure 2), can create a non-linear scaling along the x axis. In order to eliminate this effect, we correct the cumulative slip of asperity i based on its total slip $u_i(t_f)$, which is supposed to be no greater than the displacement $d_P(t_f)$ of the PMMA plate at time t_f . Given the corrected cumulative slip

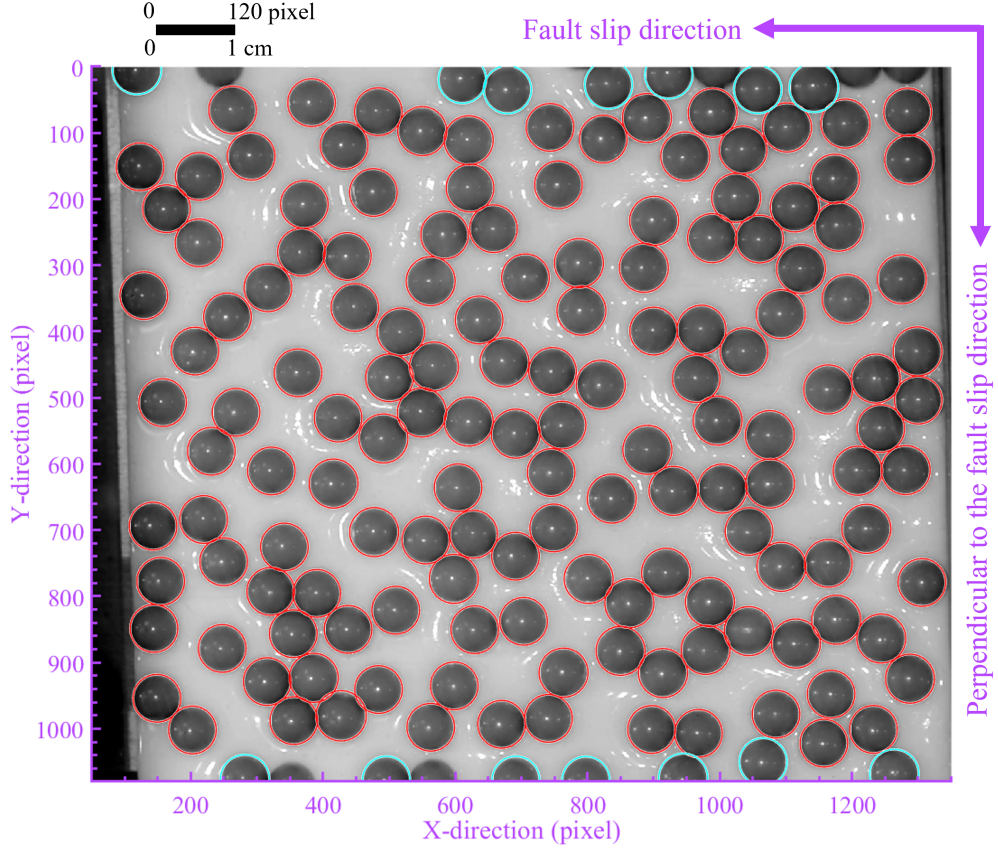


Figure 5. Typical automatic detection results indicating the initial positions of asperities at time t_0 , on the interface within a region of interest of dimensions 1300×1080 pixels (i.e., 108.33×90 mm). The asperities without markers represent the undetected ones while the asperities with blue circles correspond to the excluded ones as their correlation windows exceed the image boundary. A total of $N = 144$ asperities marked by red circles are kept and their positions $x_i^*(t_0)$ are taken as the initial positions for computing the slip through the image correlation.

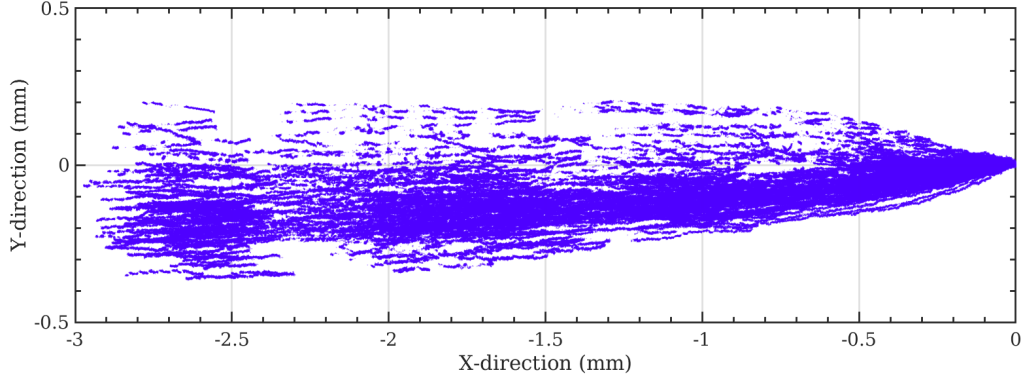


Figure 6. Trajectories of all the asperities during the whole duration of an experiment under a normal load of 400 N and a loading rate of $5 \mu\text{m/s}$. The onset of each trajectory is superimposed to be at the origin $(0,0)$. The prominent gaps correspond to the large stick-slip events.

$u_i(t)$ of asperities, we then update the displacement $d_i(t)$ of asperities following the equation (3).

Finally, we also note that the asperities also exhibit slips perpendicular to the loading direction. These cumulative slips are near-evenly distributed around zero and the maximum cumulative slip is quite small compared to the cumulative slip along the faulting direction. We present the trajectories of all the asperities during the whole experimental duration in Figure 6, where the onset of the trajectory of each asperity is set to be at the origin $(0,0)$. The total slip during this experiment is of the order of the asperity size, $R = 3 \text{ mm}$, and the slip in the x direction is about 10 times larger than that in the y direction. There is a fan shape of the trajectories with a mean y -direction that is close to zero. We observe several prominent gaps that correspond to the large stick-slip events during the faulting. For the other experiments under different loading characteristics, the total slip of asperities in the x direction is dependent on the loading rate and the experimental duration while that in the y direction is generally of the same order of $\sim 0.3 \text{ mm}$.

3 Collective Behavior of Asperities

3.1 Temporal Evolution of the Cumulative Slips of Asperities

To understand the individual behaviors of asperities as well as the relationship between each local asperity and the whole interface, we present the temporal evolution of the cumulative slips of individual asperities. For a better visibility, only 20 asperities, randomly selected out of 144 asperities, are presented in Figure 7. The cumulative slips of the 20 asperities are color-coded by their initial positions $y_i(t_0)$. We also indicate in Figure 7 the loading rate of the interface which is $15.0 \mu\text{m/s}$ here. Any asperity following this trend could be considered then as fully sliding. On the contrary, a fully sticking asperity would accumulate no relative slip with respect to the loading plate. Its behavior would appear as a horizontal line in Figure 7.

The stepping feature of cumulative slip evolution of the asperities in Figure 7 illustrates the repetitive stick-slip events of the interface (20 events in Figure 7a and a zoom on one of them in Figure 7b). These events involve all the asperities of the interface. In the time interval between these whole stick-slip episodes, during the sticking phase, the asperities show distinct behaviors. We observe that all the slipping rates are smaller than that of imposed loading rate (see the slopes of the cumulative slip of the asperities and the PMMA plate) but with a non-horizontal trend, which indicates that, actually, the asperities are slipping at a low rate during the sticking phase, instead of being fully locked.

It is noteworthy that the slips accumulated during each sticking period are not the same for different asperities. This proves that different asperities can slip at different rates, though they are all in the quasi-static regime (i.e. the sticking phase of the interface stick-slip behavior). Another interesting finding is that there are also some small visible slips that occurred at different single asperities during the overall sticking phase and correspond to small stick-slip events at the scale of several asperities. These small episodes contrast with global slip episodes, when all the local asperities slip rapidly in a synchronous way and that we define as a large stick-slip event (LSE). Moreover, the observation that the slips on all asperities after a LSE do not reach the imposed loading slip, indicates that accumulated stress is only partly released during such a whole scale event.

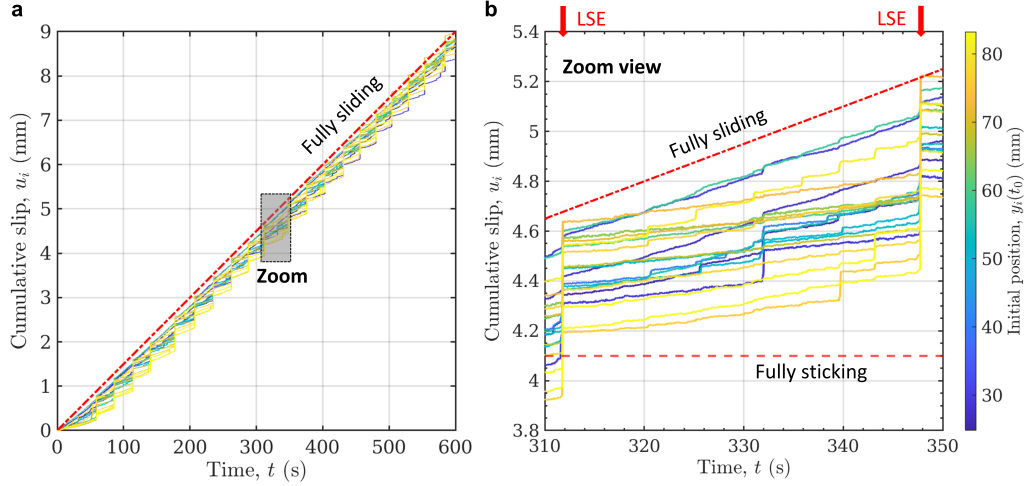


Figure 7. a: Temporal evolution of the cumulative slip in the x direction for 20 asperities during an experiment under a normal load of 200 N and a loading rate of $15.0 \mu\text{m/s}$. The cumulative slips of the 20 asperities are colored-coded by their initial y positions at time t_0 . b: Zoom view of Figure 7a showing the detailed behaviors of asperities during one time interval between two large stick-slip events (LSE) and ranging from 310 s to 350 s. Fully sticking indicates a locked state while fully sliding gives the slope of the imposed displacement rate to the system.

3.2 Slip Velocity of Asperities

Slip velocity reflects the slipping rate of asperities, which is estimated using a given discretization of the time (i.e., time step) during the whole experiment. The slip velocity $v_i(t_k)$ of each asperity i is computed as

$$v_i(t_k) = \frac{s_i(t_k)}{\Delta t} = \frac{u_i(t_k) - u_i(t_{k-1})}{\Delta t}, \quad (4)$$

where $s_i(t_k)$ is the slip of the asperity i at time t_k and Δt is the fixed time step of $1/29.97$ s determined by the sampling rate of the camera, i.e., $t_k - t_{k-1}$. Following the same experimental data used in Figure 7, for illustration, the slip velocity of all the 144 asperities ranging from time 330 s to time 350 s is shown in Figure 8, where the asperities are sorted in ascending order by their initial positions $x_i(t_0)$. A LSE involving the synchronous slipping of all the asperities is observed at the time 348 s. We also observe several small stick-slip events that share the same characteristic, which is the synchronized sliding of only a part of the asperities.

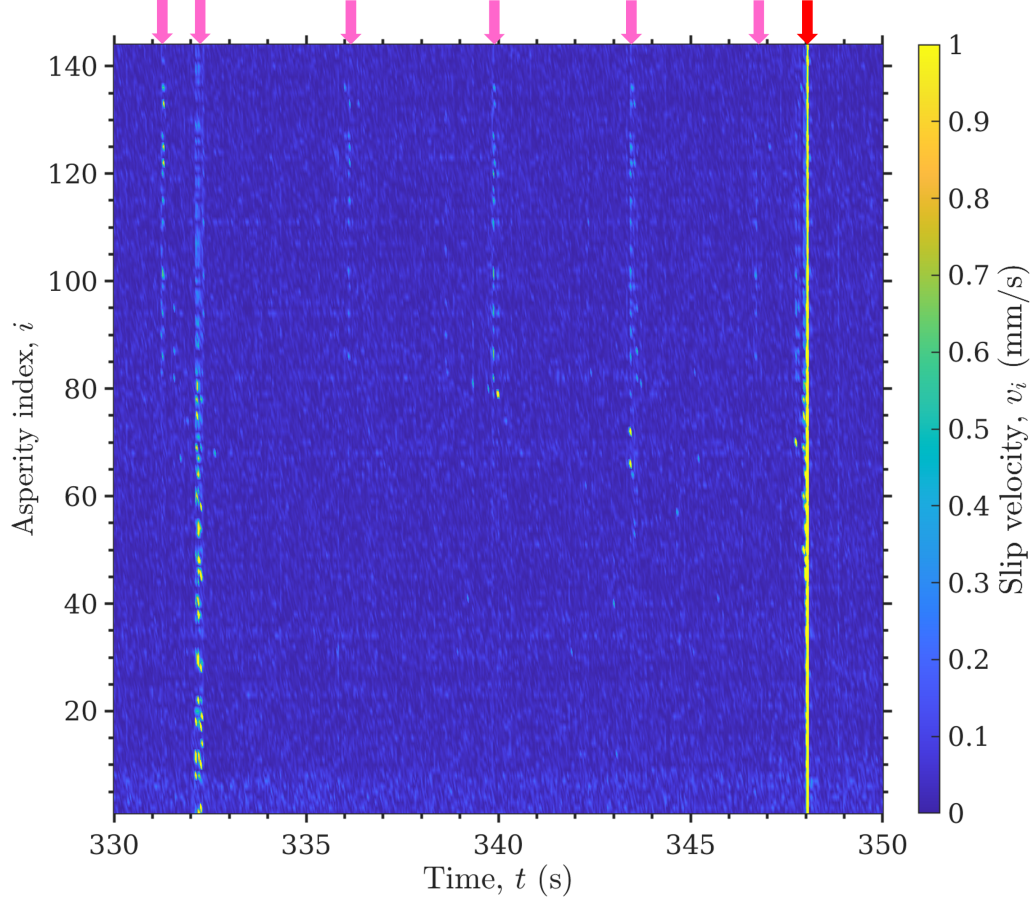


Figure 8. Slip velocity of all the asperities during the time period ranging from 330 s to 350 s of the same experiment shown in Figure 7. The asperities are sorted in ascending order by their initial x positions at time t_0 , $x_i(t_0)$. A large stick-slip event (LSE) indicated by the red arrow occurred at time 348 s observed, where all the asperities are synchronously slipping. During the sticking phase, there are also several small stick-slip events (SEs) which are indicated by the pink arrows involving the slipping of a part of asperities.

3.3 Mechanical Response of the Interface

In order to document the mechanical response of the frictional interface, we analyze how the friction coefficient, $\mu = F_S/F_N$, evolves as a function of slip. We compute the spatial average of the cumulative slip, $\langle u(t) \rangle$, over all asperities, N , following

$$\langle u(t) \rangle = \frac{1}{N} \sum_{i=1}^N u_i(t), \quad (5)$$

which is a global indicator of the collective behavior of all the asperities. As multiple seismic cycles (i.e., large stick-slip events) are produced during a single experiment, we report in Figure 9a the evolution of μ as a function of $\langle u(t) \rangle$, for all the cycles of a single experiment. Each cycle is separated based on the onset of a large scale slip event LSE (observed when μ reaches a local maximum before an abrupt decrease). The value of the friction coefficient mainly ranges between 0.10 and 0.23, which is a low friction coefficient but comparable to the values in other PMMA-PMMA interfaces (Baumberger & Caroli, 2006; Selvadurai & Glaser, 2015). We observe, in each cycle, an overall frictional strengthening stage during the sticking phase and a weakening stage during the slipping phase.

To focus on the sticking phase of the whole faulting process, the variations of friction coefficient, $\Delta\mu$, and of the average cumulative slip, $\Delta\langle u(t) \rangle$, are both computed relative to their respective values at the onset of these large scale slips. We plot the friction coefficient variation, $\Delta\mu$, as a function of the variation of the average cumulative slip of all the asperities, $\Delta\langle u(t) \rangle$, by superimposing all the sticking phases and the slipping phases, where each onset of the slipping phase is set to be $\Delta\mu = 0$ and $\Delta\langle u(t) \rangle = 0$ (Figure 9b). The curves represent the sticking phase while the circles represent only a few time steps after the onset of the LSE. We observe a good similarity between all seismic cycles, proving the repeatability of our observations. We observe that the friction coefficient during the period preceding the large scale event (LSE) is increasing. This strengthening of the interface is occurring while the interface is slipping. We observe that during this overall increase of the friction coefficient, there exist multiple instances where μ actually drops significantly compared to the error of the friction coefficient measurement. The strengthening of the interface (an overall increase of μ) is thus not a homogeneous process and is slip-controlled in a non-linear manner. This shows as well that this strengthening stage, conventionally considered as the stable regime of a fault, actually consists of many small-scale destabilizing events. The rapid slip that occurs dur-

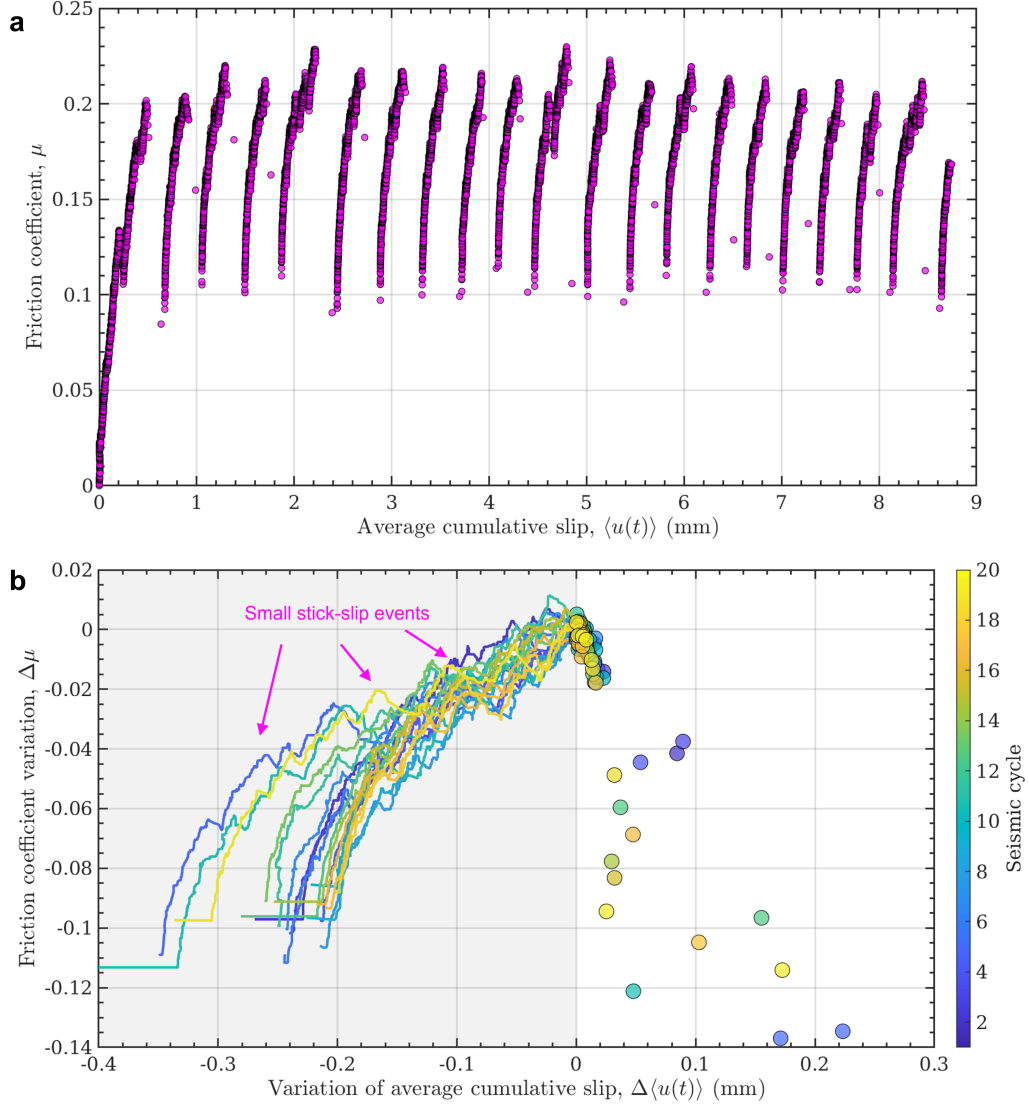


Figure 9. a: Evolution of the friction coefficient, μ , as a function of the average cumulative slip, $\langle u(t) \rangle$, during the same experiment shown in Figure 7 with multiple seismic cycles. b: Friction coefficient variation, $\Delta\mu$, as a function of the variation of the average cumulative slip of all the asperities, $\Delta\langle u(t) \rangle$, for the same experiment shown in Figure 9a. All the seismic cycles represented by different colors are superimposed together by setting the onset of each slipping phase as the origin. The colored curves in the shadow indicate different sticking phases while the circles denote the corresponding slipping phases.

ing a LSE is not well captured by our experiments mainly because of the limited time resolution of the camera that does not allow a sufficient time sampling during this stage. It is also possible that the weakening part is velocity dependent which is not well captured here since Figure 9b represents the friction coefficient as a function of slip with no information on the velocity.

3.4 Topographical Effect on Interseismic Slipping Behaviors

Our results show that many small stick-slip events accompanied by friction coefficient drops are found during every fault strengthening stage (Figure 9). These interseismic, small stick-slip events result from the slip of a limited number of asperities on the interface. In order to identify what controls the number and the amount of these partial slips, we document the interseismic slipping behaviors of the asperity using the interseismic coupling coefficient (Hyndman et al., 1997). We denote the onset times of the j and the $j+1$ large stick-slip events as $t(\text{LSE}(j))$ and $t(\text{LSE}(j+1))$, respectively. To describe the extent of the slipping of the asperity i during the interseismic phase between $t(\text{LSE}(j))$ and $t(\text{LSE}(j+1))$, the interseismic coupling, $\lambda_{i,j+1}$, is computed as

$$\lambda_{i,j+1} = 1 - \frac{u_i(t(\text{LSE}(j+1))) - u_i(t(\text{LSE}(j)))}{d_P(t(\text{LSE}(j+1))) - d_P(t(\text{LSE}(j)))}. \quad (6)$$

We note that λ is in the range $[0, 1]$, where $\lambda = 0$ indicates no coupling or fully sliding while $\lambda = 1$ denotes a fully coupled interface or sticking. For experiments with multiple seismic cycles, we compute the final interseismic coupling for each asperity i by averaging λ_i over all of the interseismic phases.

With the experimental data used in Figure 9, we present the interseismic coupling of these asperities along the interface (Figure 10). We observe a large scale trend of this interseismic coupling that we can link with the same trend observed from the peak height of asperity derived from the topographical map (Figure 3b). A higher peak height of asperity corresponds to a higher interseismic coupling while a smaller peak height is corresponding to a lower interseismic coupling. This can be interpreted in terms of normal stress on the asperity where a higher peak height causes a greater normal stress, and therefore creates the locking of the asperity which increases the interseismic coupling. On the contrary, the asperities with smaller peak heights have a low normal stress and thus cannot accumulate large shear stress (and consequently large slip deficit) and will fail more often during the interseismic phase and have a low coupling, i.e., low values of λ .

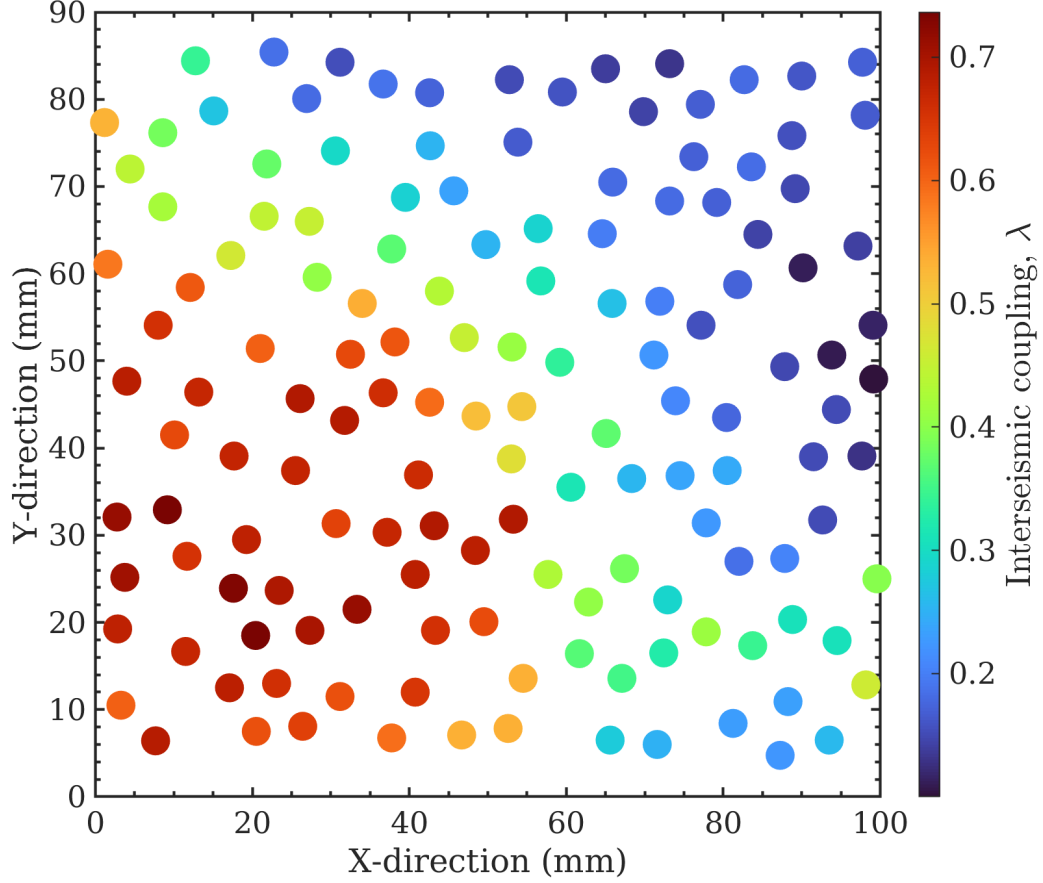


Figure 10. Map of the interseismic coupling of asperities along the interface using the same experimental data shown in Figure 9. A similar pattern between the peak heights of asperity (Figure 3b) and the interseismic coupling is observed, which shows that a larger peak height corresponds to a larger interseismic coupling whereas a smaller peak height corresponds to a lower interseismic coupling.

We also investigate the direct effect of the macroscopic normal load on the interseismic coupling, as shown in Figure 11. For all experiments with the same normal load, we compute the interseismic coupling of each asperity, which is indicated by the color circles. The average evolution of the interseismic coupling with peak heights conceals some scattering. Indeed, we can observe from Figure 11 that for the same normal load and the same asperity height, different values of λ are computed. To present the evolution of the interseismic coupling as a function of the peak height of asperity, we average the interseismic coupling values over peak heights within a bin width of 0.10 mm. It evidences that, when the normal load is low: 10 N and 25 N, all the asperities have a quite small interseismic coupling, a value that is not distinguishable from zero. The interseismic coupling shows no dependency on the peak height. This is consistent with the mechanical response of the fault system shown in Figure 4, where the global fault slips almost steadily under the normal loads of 10 N and 25 N.

As the normal load increases and becomes large enough such that large stick-slips of the whole fault system are observed, we evidence that interseismic coupling is then dependent on the peak height of asperities. The asperities with low peak heights correspond to low normal stresses, thus inducing the small stick-slip events observed in between the large stick-slip events due to a small interseismic coupling. For the same peak height of asperity, the interseismic coupling increases with the increase of normal stress, which strengthens the locking of the asperities. The maximum value of the interseismic coupling is about 0.55 which is significantly lower than 1. This is consistent with the partial slipping of asperities shown in Figure 7b and Figure 8. It is interesting to note a transition of the interseismic coupling, for a given normal load, at a specific peak height threshold. This peak height threshold is decreasing as a function of the increased normal stress (from about 2.67 mm at 50 N to about 1.85 mm at 700 N). The interseismic coupling above this peak height threshold converges for all loading conditions to a constant value of around 0.6. Below the threshold, λ decreases towards 0.

4 Interactions between Asperities during the Strengthening Phase

4.1 Collective Slip Episodes

To investigate the spatiotemporal interactions of asperities, we use a two-step procedure in order to define and characterize slip episodes (SEs). In the first step, we an-

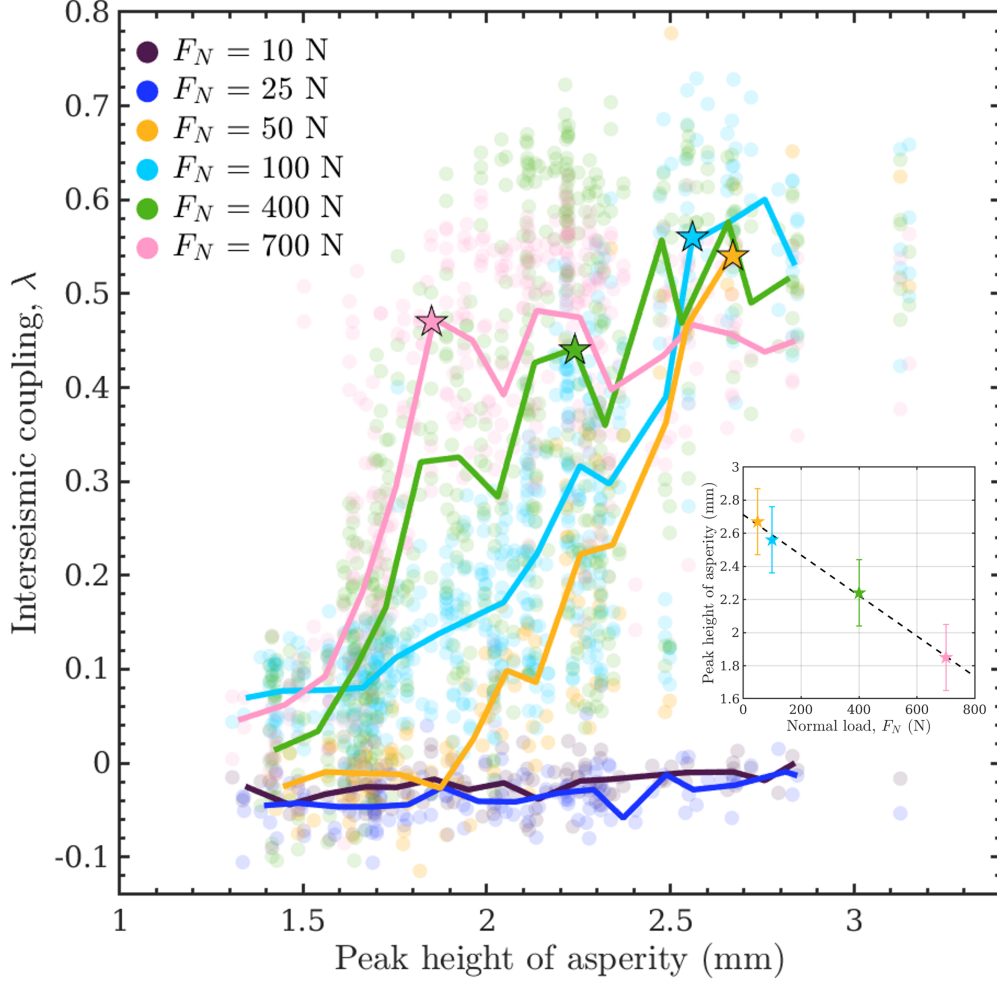


Figure 11. Evolution of the interseismic coupling at different peak heights of asperity under multiple normal loads. The circles with one filled color are the dataset computed for all the experiments under the corresponding normal load. Each curve is obtained by averaging the interseismic coupling over the peak height of asperity with a bin width of 0.10 mm. The inset displays the peak height of asperity at transitions from high to low coupling (stars) as a function of the normal load, where the peak height of asperity decreases with the increase of the normal load.

analyze individually each asperity to isolate individual asperity slips (IASs) from their slip history. In the second step, we identify collective behavior by clustering IASs based on their time and space connection to build slip episodes. The first step is realized by thresholding the velocity $v_i(t)$ for each asperity i . We use a threshold Γ_i specifically for each asperity i , which is determined by considering the median \tilde{v}_i and the median absolute deviation D_i^{med} of the slip velocity $v_i(t)$,

$$\Gamma_i = \tilde{v}_i + c \cdot D_i^{med}, \quad (7)$$

We test several values of the coefficient c in front of D_i^{med} (see Figure S1) and found that the value retained here ($c = 6$) is best able to separate noise from slip event. Following equation (7), we define the IASs as periods with $v_i(t) > \Gamma_i$ while the others with $v_i(t) \leq \Gamma_i$ are taken as minor slip events and possible noise, and are not included in the catalog of IASs. Figure 12 presents the slip events (blue stars) of one single asperity ($i = 98$) for the same experiment displayed in Figure 7 and its corresponding threshold Γ_{98} (thick magenta line). We find a diversity of slip velocities of IASs. To display the IASs with low slip velocities during the interseismic phase, we zoom in on Figure 12 during a time interval between two large stick-slip events, ranging from 310 s to 350 s (the same time period exhibited in Figure 7b). The observation that several IASs with moderate maximum slip velocity are observed for this asperity is actually consistent with the small stick-slip events found during the fault strengthening stage shown in Figure 9. For each experiment, we establish a complete catalog of IASs by computing the slip velocity $v_i(t)$ of all the asperities and the corresponding threshold Γ_i .

To cluster in space and time all the IASs defined at different asperities into collective SEs covering multiple asperities and time steps, we analyze the time and space connections of these IASs. We define a link between a pair of IASs if the two events are separated in time by one or less time step and if they have a spatial connection (i.e., they are nearest neighbor), introducing a two-dimensional Delaunay triangulation, and considering the location of each asperity as a vertex (Lee & Schachter, 1980). The edges of the resulting triangulation give the spatial connection between asperities used to make clusters. Additionally, we assume that an asperity is always spatially linked with itself. The IASs simultaneously connected in time and space scales are clustered as a new SE using a single linkage clustering algorithm (Gan et al., 2020). IASs that are not linked to other neighboring IASs are considered as individual SEs. Figure 13 shows one SE last-

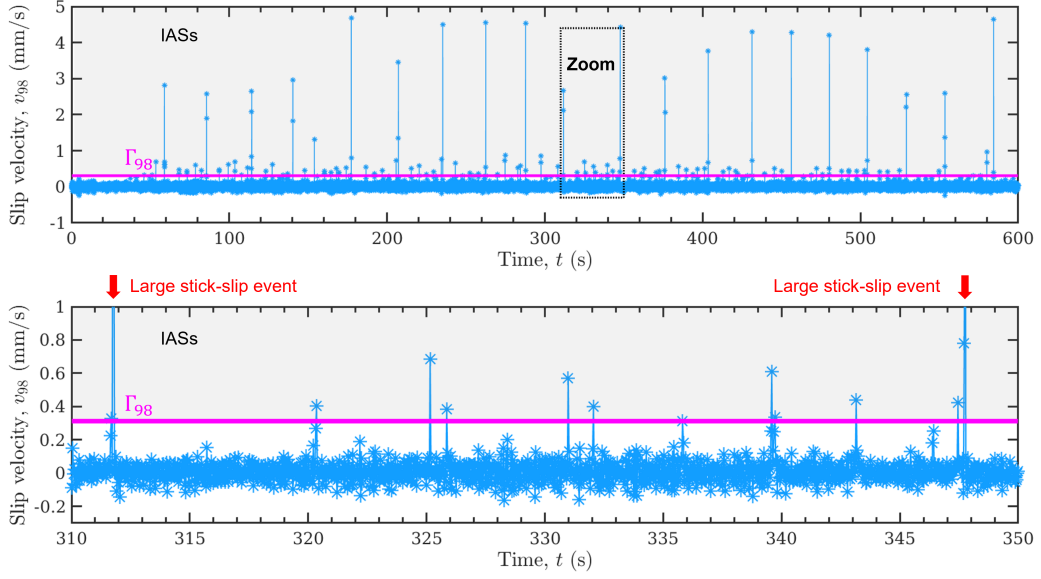


Figure 12. Time-localized slip events produced by a single asperity ($i = 98$) in the same experiment shown in Figure 7. The blue stars and the thick magenta line represent slip events and the corresponding threshold Γ_{98} specifically computed for this asperity. The slip events localized in the shadow region with slip velocity greater than the threshold are defined as IASs while the others indicating minor slip events and noise are removed. A zoom view showing the low amplitude IASs during an interseismic phase ranging from 310 s to 350 s is presented below. Several IASs with low slip velocities are observed.

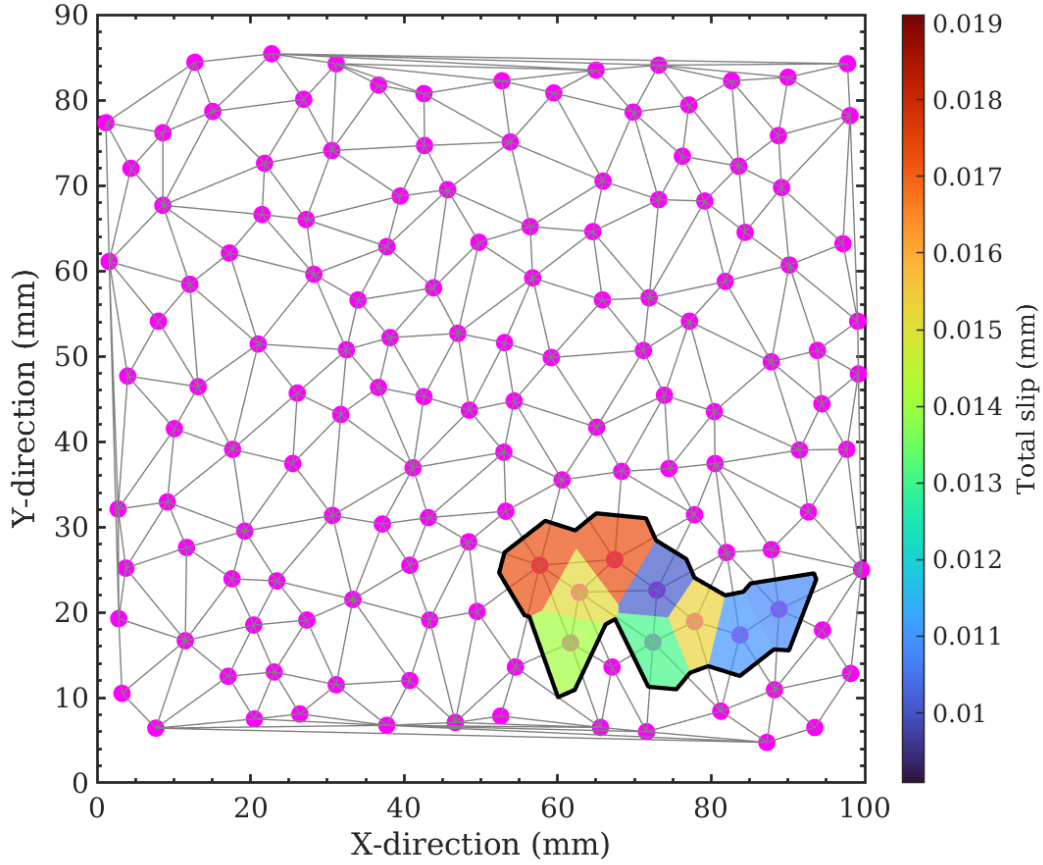


Figure 13. Example of one SE lasting one time step which is composed of nine IASs (polygons with different colors) colored by their total slips. The magenta dots and gray lines indicate the bead locations and the spatial connections all over the interface determined by the Delaunay triangulation, respectively.

ing only one time step, and composed of nine IASs. The polygons with different colors represent the slip area allocated to each IAS and are determined by the Voronoi diagram corresponding to the performed triangulation (Fortune, 1995). We, therefore, are able to build the catalog of spatiotemporal SEs for each experiment.

4.2 Magnitude-Frequency Distribution

In order to characterize the so-formed slip events, we first investigate their magnitude distribution. The magnitude of the slip event is estimated based on the computation of their moment, M_0 . For one SE containing n IASs, its seismic moment is com-

puted as:

$$M_0 = \sum_{i=1}^n G \cdot A_i \cdot s_i, \quad (8)$$

where G is the shear modulus of the PMMA, A_i and s_i are respectively the slip area and the slip of each IAS i that compose this SE. Then, we can calculate the magnitude M of each SE following (Hanks & Kanamori, 1979) as:

$$M = (\log_{10} M_0 - 9.05)/1.5. \quad (9)$$

The magnitude-frequency distributions of the SEs extracted from three experiments, which are under the same normal load of 400 N but with three different loading rates, are presented in Figure 14. The symbols with crosses represent the large stick-slip events that involve all the asperities of the interface and subsequently with a size controlled by the finite size of the interface. As evidenced already for finite systems, the distribution of events is bimodal: exponentially distributed size for the events not reaching the interface and a peak for system-wide events (Fisher et al., 1997). Excluding system-wide events, the observed distributions follow a typical Gutenberg-Richter distribution (Gutenberg & Richter, 1944): $\log_{10} N(m) = a - bm$. For the three experiments under loading rates of 5.0 $\mu\text{m/s}$, 10.0 $\mu\text{m/s}$, and 15.0 $\mu\text{m/s}$ and a normal load $F_N = 400$ N, their b values are 1.21 ± 0.05 , 1.44 ± 0.1 , and 1.35 ± 0.12 , respectively. A gray dashed line showing a reference b value of 1.3 is displayed in Figure 14. We can observe that all these three experiments have a b value nearly similar to this reference. It shows that the b value has no clear dependence on the loading rate of the system. In addition, our experimental results show that the b value is insensitive as well to the imposed normal load (see Table S2).

4.3 Moment-Duration Scaling Relation

For regular earthquakes, a scaling relation between the moment and the duration is commonly observed and takes the form $M_0 \propto T^3$ (Kanamori & Anderson, 1975). This relation can be understood from the representation of an earthquake as a circular crack expanding at a constant speed and with a constant stress drop. Another scaling relation has also been resolved for slow slip events observed in subduction megathrusts which follows the form $M_0 \propto T$ (Gao et al., 2012; Ide et al., 2007).

We represent from our SEs the relation between their duration, T , defined as the time difference between its onset and end, and their moment, M_0 (Figure 15a). The moment-

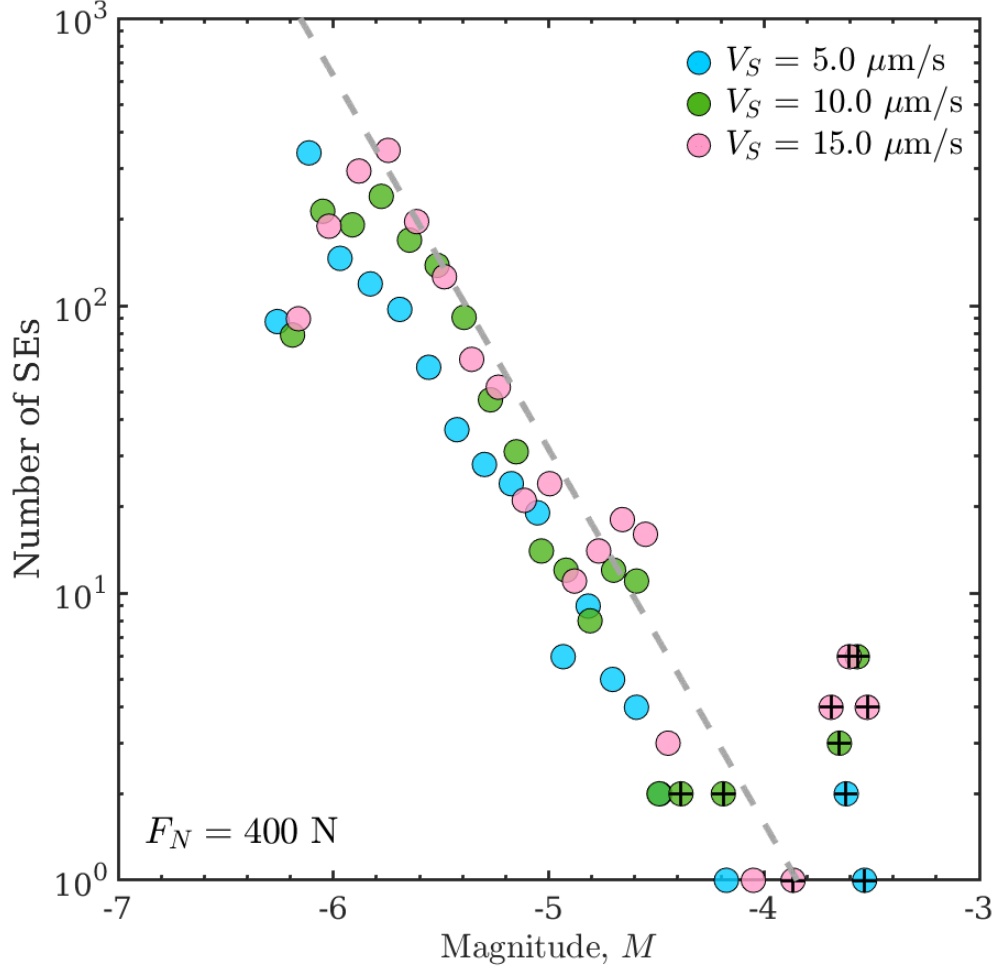


Figure 14. Magnitude-frequency distribution at different loading rates under the same normal load of 400 N. The circle symbols marked by crosses indicate the large stick-slip events at the global fault scale, which are excluded from the computation of the b value. The gray dashed line indicates a reference line with a b value of 1.3.

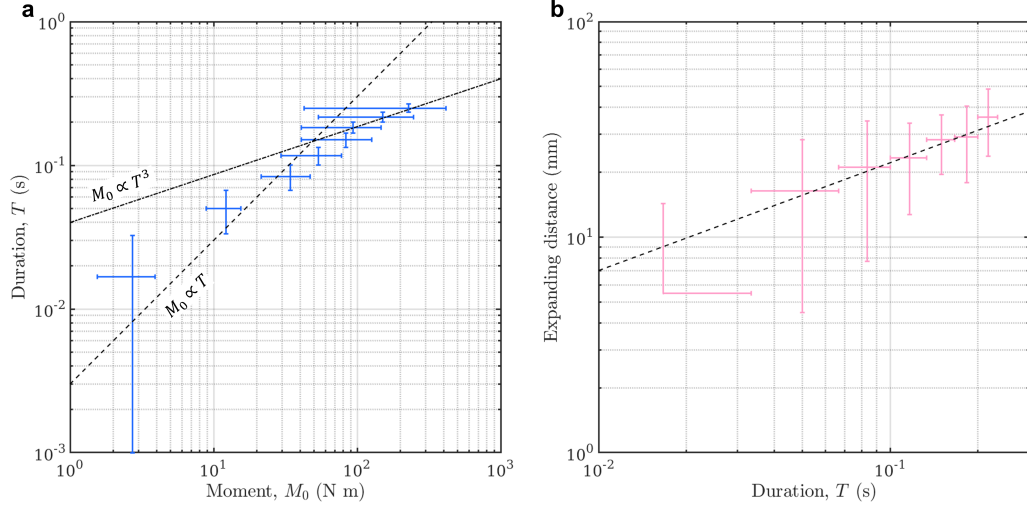


Figure 15. a: Moment-duration scaling relation obtained using SEs from all experiments at various normal loads and loading rates. The black dash-dotted line and dashed line represent the scaling relations of $M_0 \propto T^3$ and $M_0 \propto T$, respectively. The largest slip events, reaching the edge of the sample have been excluded. b: Scaling relation between the expanding distance of SEs and their duration. The black dashed line represents the square-root scaling relation between the expanding distance and the duration.

duration scaling is represented for all experiments with various normal loads and load-
ing rates. In order to retain in this analysis only confined ruptures and not be influenced
by the condition at the edge of the sample, the largest slip events reaching the edge of
the sample are excluded. We evidence a linear scaling relation close to $M_0 \propto T$ for all
the experiments for $M_0 < 100$ N m and a transition to the scaling for earthquakes ($M_0 \propto$
 T^3) for the largest events.

For each SE, excluding large-scale stick-slip events, we also compute the distance
between the first and last slipping asperities. The duration and expanding distance are
averaged to present their relation, as shown in Figure 15b. We observe a square-root scal-
ing relation between the expanding distance and the duration.

4.4 Temporal Decay of Slip Episodes

In order to investigate the possible time interaction between our identified SEs, we compute the time correlation between them, $C(t)$ with

$$C(t) = \frac{1}{Tn_t} \sum_{i=1}^{n_t} \sum_{j=i+1}^n \Theta(t_j - t_i \in [t; t+T]), \quad (10)$$

where $\Theta(\mathcal{P})$ of proposition \mathcal{P} is 1 if \mathcal{P} is true and 0 otherwise. In order to take into account the time finiteness of the catalog, the first sum is performed up to n_t which is the largest index i such that $t_n - t_i < t+T$, where T is the duration of the time bin. The equation (10) actually gives the average rate of SEs at time t following a preceding slip event and we represent an example of $C(t)$ computed for an experiment under a normal load of 200 N and a loading rate of 15 $\mu\text{m/s}$ (Figure 16). We observe a rapid decrease of $C(t)$ at a short time range, following a power law decay similar to $1/t$. After a duration of about 1 s, the average rate of SE stabilizes to a background rate of around 2 SEs per second. This indicates that interactions between SE exist for a short time and that they quickly decay. This evolution of the event's rate bares some analogy with Omori's law observed after large earthquakes which gives as well a decay of the earthquake rate following $1/t$ (Utsu et al., 1995).

5 Discussion

5.1 Interseismic Coupling

Our results indicate that the interseismic slip rate relative to the loading rate, i.e. the interseismic coupling, λ , is related at first order to the normal stress imposed on the asperities. The transition from small to high coupling is a function of the normal load (the height of the asperity at this transition is decreasing with normal stress) but the value of the coupling at high or low normal stress is the same for any normal load. This is visible first as a global macroscopic effect affecting all asperities when we change the imposed normal load in our experiments (Figure 11). This can also be observed at the individual asperity scale where we observe that the asperity peak height is correlated with λ . Indeed, considering a simple Hertz contact model, a higher asperity height results in higher normal stress. The distribution of asperity heights in our experiments, therefore, leads to a distribution of normal stresses and a continuum of values of λ (Figure 11).

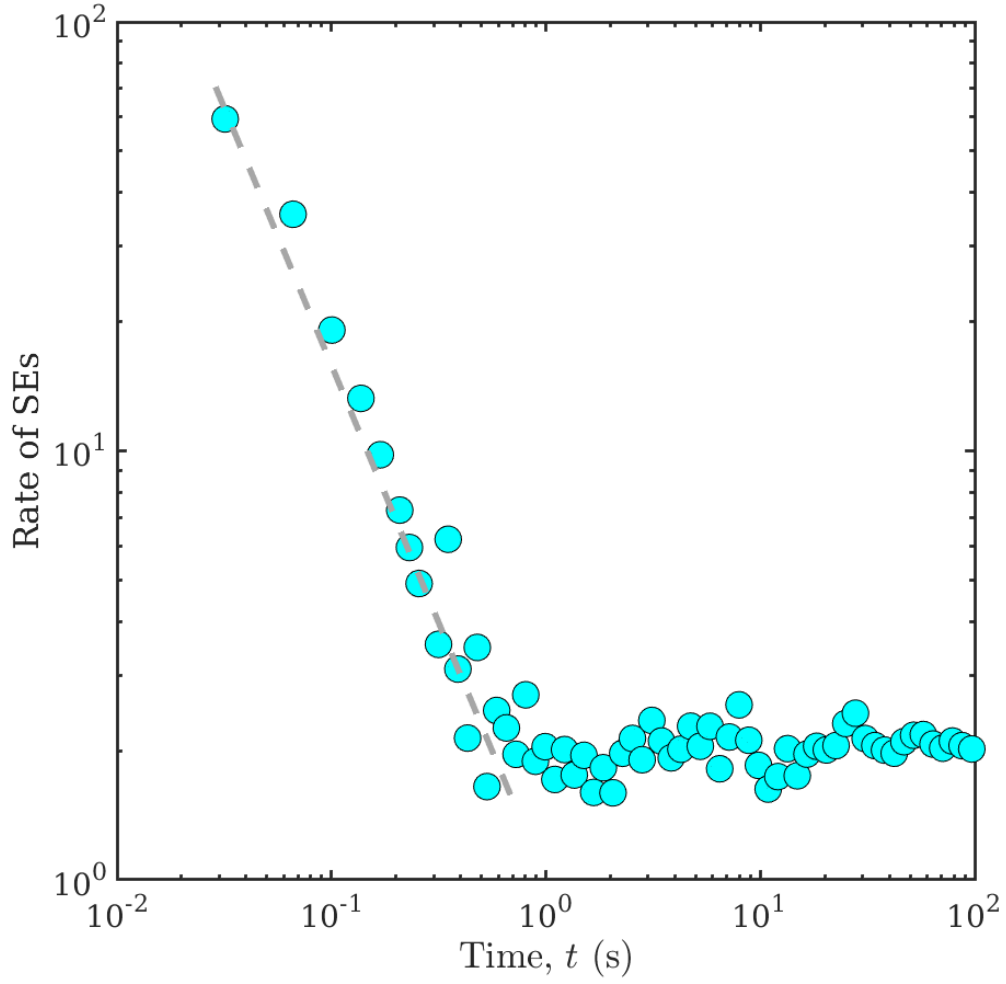


Figure 16. Temporal decay of SEs defined in an experiment under a normal load of 200 N and a loading rate of $15 \mu\text{m/s}$. The rate of SEs first decays rapidly with $1/t$ during about 1 s and then keeps stable as a background value of about 2 SEs per second.

It is tempting to relate the characteristic asperity height in our experiment to the critical reduction in the normal force, ΔF_N^* , that controls the transition from low to high coupling, as identified in the model of Scholz and Campos (1995, 2012). We note however that in this model the transition results from the sole effect of the global normal load since the interface is considered as homogeneous. This approach is thus describing the effective seismic coupling of the interface but not that of the asperities, which we can achieve in our experiments. We interpret that the effective coupling of the interface is a function of the quenched disorder of the fault and then indirectly of the normal stress. If we assume the same height of all the asperities, there would be no variance in interseismic coupling at different asperities at the same time. Similarly, the whole interface would have the same behavior as that of the asperities and lead to little collective effect. We emphasize here that a large scale topography of a fault with variations of the asperity heights can influence the effective seismic coupling of the fault differently from a classical normal stress level effect. This is a collective effect but related to the quenched disorder of the asperities.

Finally, we acknowledge that the definition of interseismic coupling is not completely satisfactory as it fails to capture the variation of the slip velocity inferred on some asperities in between two large scale stick-slip events. Indeed, we highlighted some transient activity and non-steady slipping rate for asperities which indicate that the value we computed only represents an effective behavior of the asperity at the time scale between two large scale stick-slip events.

5.2 Interfacial Elastic Energy

Our results evidence that for an interface composed of multiple asperities, as in our system, local slip events with various sizes (see Figure 14) are taking place at all times. We also note that large scale events that involve slips on all asperities of the interface are also observed. These large scale slip events can only happen when sufficient large stress has been accumulated on the strongest asperities. This requires that asperities at some time are synchronized such that initiating the failure at one location triggers the cascading rupture of all the asperities on the interface, thus generating the large scale stick-slip event. This is equivalent to a collective depinning induced by the long range elastic interactions in a slowly (quasi-static) loaded system.

We quantitatively illustrate such synchronization effect by computing the evolution of the interfacial elastic energy, E_h , and of the bulk elastic energy, E_t , following the definition of Schmittbuhl et al. (1996). The interfacial elastic energy, E_h , is quantified through the sum of the relative distance between two asperities over all the spatial links defined by the two-dimensional Delaunay triangulation:

$$E_h(t) = K_N \sum_{k=1}^D (l_k(t) - l_k(t_0))^2, \quad (11)$$

where l_k is the relative distance computed through the x positions of two asperities linked spatially and D is the number of the spatial links between two asperities defined by the Delaunay triangulation. K_N is the compressive stiffness between asperities, computed through $K_N = E_s \langle d_{asp} \rangle$, where E_s denotes Young's modulus of the silicone block and $\langle d_{asp} \rangle$ is the average distance between asperities which estimated to be 6 mm. The interfacial elastic energy, E_h , actually quantifies the variance of the change of distance between neighboring asperities, thus is related to the elastic force interactions between asperities. The bulk elastic energy, E_t , is the total elastic energy stored on the interface through the global loading, which is characterized by the collective change in the absolute positions of all the asperities along the x direction:

$$E_t(t) = K_S \sum_{i=1}^N (d_i(t))^2, \quad (12)$$

where K_S is the shear stiffness estimated using $K_S = G_s L$. G_s is estimated from Young's modulus of the silicone block, 1.1 MPa, while L is the size of the interface, 10 cm. N is the total number of asperities and d_i the displacement of each asperity.

We present the interfacial elastic energy, E_h , and the bulk elastic energy, E_t , as a function of the PMMA plate displacement, d_P , for different experiments with various normal loads but the same loading rate, as shown in Figure 17. We identify multiple large scale stick-slip events and the corresponding fault strengthening phases from the large abrupt drops of E_t and the slow accumulation of E_t , respectively. We also observe a similar pattern for the evolution of E_h , which is equivalent to the direct measure of the spreading of the x positions of the asperities apart from their initial position where $E_h = 0$. Additionally, we observe a clear dependency of E_h and E_t on the normal load, which is consistent with the mechanical response of the fault system shown in Figure 4. With the increase of normal load, the interfacial elastic energy, E_h , and the bulk elastic energy, E_t , also increase.

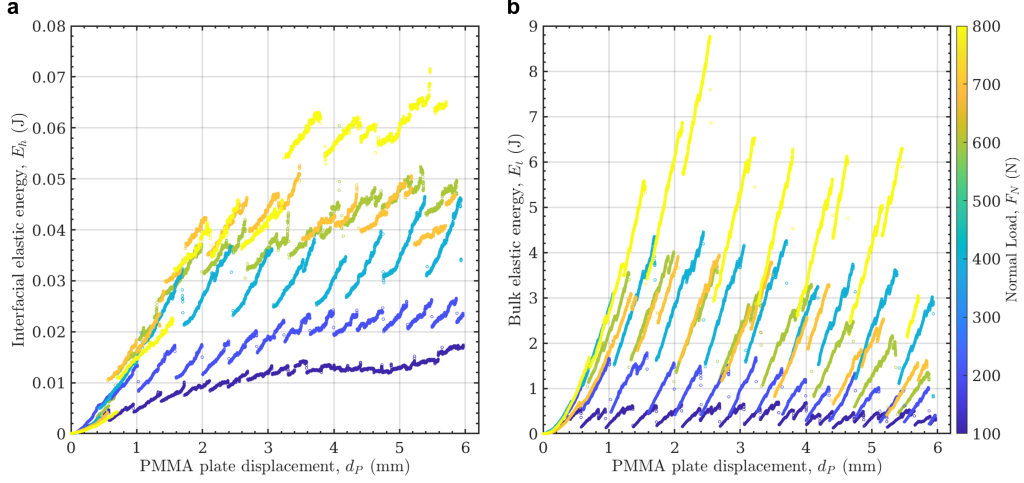


Figure 17. Evolution of (a) the interfacial elastic energy, E_h , and of (b) the bulk elastic energy, E_t , under different normal loads and the same loading rate. Both E_h and E_t accumulate slowly during the fault strengthening phases and drop when a large stick-slip event occurs. Both E_h and E_t show a clear dependency on the normal load.

Such evolution of the elastic energies during successive seismic cycles illustrates the disordering effect of asperities and the build-up of the elastic energy during the strengthening phase. We interpret the rising E_h as the disordering process of asperities, that is the strong perturbation from the initial position which is supposed to be quenched in the system. The sticking phases correspond to a period of increase of E_h during which the asperities increase disordering, while a large scale event corresponds to the rapid decrease of E_h (re-ordering of the asperities). We note that during such a large scale event, while E_t drops significantly and returns to zero, the drop of E_h is only partially such that a disorder, and elastic energy, is still present after a large event. It implies that there is a memory effect over the cycles from the relative positions of the asperities.

We also observe a transient period at the beginning of the shearing where the evolution of E_h is similar for all experiments. As the normal stress is increased a larger level of E_h is reached in the system, so a larger disordering of the asperities. It implies that higher normal stress prevents the interface to come back to its initial state (with low E_h) even during a LSE and so maintains a larger disorder in the system with internal stresses along the interface at any time.

The process of synchronization has been well documented notably in numerical simulations and shows that only for forces larger than a critical force, that constitute a critical point, the system will become unstable and sliding will extend to all sites of the interface (Fisher et al., 1997; Tanguy et al., 1998; Kammer et al., 2015; de Geus et al., 2019; Albertini et al., 2021). This constitutes a depinning transition and this phenomenology leads to stick-slip. In such models, this critical force is linked to a critical length scale, L_c , of an initiating slip pulse, that will invade all the interface if its extension becomes larger than L_c . Most of these results were inferred from a homogeneous fault model. Here, both the evolution of the macroscopic force (Figure 9) and the distribution of slip events in Figure 14 are not in agreement with these predictions. Indeed, we first observe in Figure 9 that the macroscopic force required to propagate a full scale event is not perfectly constant but rather displays some fluctuations from one rupture to the other. Secondly, the distribution of event magnitudes (Figure 14) shows almost no gap between the largest avalanche and the whole interface avalanche. It, therefore, implies that avalanches of all sizes can exist in the system without necessarily leading above a certain size to a complete failure. In such a case one would expect a larger gap in event size between the maximum observed avalanche and the system wide event. Such different nucleation mode can arise in the heterogeneous system as interactions between arrested small events could exist and significantly modifies the process leading to a major rupture (Albertini et al., 2021). Interpreting these results in terms of fault mechanics suggests that creeping faults correspond to the interface with an asperity disorder and a strengthening regime with disordering of the interface by small destabilizing events that increase elastic interaction between asperities but without impacting the global fault loading.

5.3 Slip Intermittency

Our system is driven by a constant displacement rate for each experiment and we measure a macroscopic velocity of the PMMA plate that is indeed constant (except during a large-scale event, where a small but noticeable displacement step is observed). This macroscopic measurement mimics the measure that could be made around natural faults by geodetic instruments located at the surface, and thus necessarily far away from the slipping area at depth. It implies that such kind of measurement actually misses the actual complexity of the slip distribution taking place on the interface at a short time and spatial scale. Some fine measurements of the slip distribution in both time and space for

shallow creeping faults indeed reveal that the long term continuous creeping of faults is actually accommodated during bursts of aseismic slip of various sizes (Jolivet et al., 2013, 2015; Rousset et al., 2016; Khoshmanesh & Shirzaei, 2018). During slow slip events, the analysis of GPS signal in conjunction with the recording of low frequency earthquakes (LFEs) also reveals that the large scale motion along the slab consists in the superposition of numerous small slip episodes each acting for a limited duration (Frank, 2016; Frank & Brodsky, 2019). The analysis of LFEs as a proxy for local slip on the interface reveals as well that these slip episodes span a wide range of sizes and present both temporal and spatial correlation (Lengliné et al., 2017). All these results are well in agreement with the observations performed in this study where the interseismic slip on the fault is characterized by slip events (SEs) of different sizes that act in a close temporal relationship.

The slip events we characterized here are slow events in the sense that their duration with respect to their size is much lower than the Rayleigh wave speed of the material that constitutes the interface. Indeed, supposing a typical PMMA Rayleigh velocity of 1255 m/s (Gvirtzman & Fineberg, 2021), this would imply that in one time frame (1/29.97 s) a dynamic rupture front travels up to 42 m. This is inconsistent with the observations of SEs that last several time frames. If we suppose that most of the stress transfer between asperities is actually mediated by the silicone base embedding the PMMA beads, this gives a Rayleigh wave velocity of the order of 20 m/s, and then the propagation of a rupture front of 66 cm in one time frame. As the largest SEs have a typical duration of 0.3 s and cover a maximum area with a characteristic dimension of half the sample length (5 cm), this suggests that the SEs formed by our criterion actually correspond to slow events. It does not preclude local dynamic rupture to take place during such SEs, but their size might be limited to a single bead contact area (or smaller). This implies that the moment-duration scaling we report in Figure 15 should be interpreted as scaling attached to slow ruptures on the interface. The best-resolved trend shows $M_0 \propto T$ in agreement notably with the observations of (Ide et al., 2007) that show that many slow slip events on subduction zones follow this scaling law. We note however that the scaling in our experiment is only resolved over a restricted range of moments. This calls for future further experiments involving an increase in the number of beads and the sampling rate of the optical device. This moment-duration scaling is also in agreement with the observed evolution of the slip event characteristic distance with the square root

of duration. This, therefore, suggests that the slip events are driven by a diffusion process controlling the propagation of the rupture, similar to slow-slip events tracked with tremor migration (Ide, 2010).

The slip event, SEs are characterized as a single rupture following the clustering procedure we defined. It is not obvious how to select the merging condition which is imposed partially in our case by the acquisition rate of the optical device. However, what is the exact definition and extent of a slip event is not a question limited to our experiment. Indeed, the analysis of earthquakes for example, generally indicates that they are actually composed of several sub-events. The identification of these sub-events, therefore, questioned the definition of the earthquake rupture that consists of several connected local slip episodes. As we discussed above, the same problem of definition arises for a slow slip event which is actually made of a sum of local transient slip episodes connected in time and space. Decreasing the time interval required to merge individual asperity slips into the same cluster would ultimately lead to only isolated local slip events. On the opposite, increasing this time interval would lead to a single slip event comprising all the beads. Finally, we conclude that SEs are thus analyzed at the spatial and temporal scale imposed by our acquisition system which is a constraint imposed as well to observations made on natural fault systems.

5.4 Mechanics of the Strengthening Regime

Our system resolves confined rupture that takes place during the strengthening phase. This contrasts with most frictional setups where only large scale ruptures are analyzed during the weakening phase. Unlike these large scale ruptures that are largely controlled by the machine loading stiffness (Leeman et al., 2016; Wu & McLaskey, 2019), partial ruptures provide the opportunity to study the slip events taking place on an interface without being actually influenced by the loading system. In our system, the events are arrested because of stress heterogeneity that arises notably from the variable asperity heights creating spatial differences in frictional strengths. We stress that the heterogeneous nature of the interface only arises as a result of the topography and the position distribution of the asperities with respect to their initial position (assessed by the interfacial elastic energy E_h), but that there is no variation of the material properties that constitute the interface. In particular, it implies that the complex dynamic that we recovered during our experiment is not the result of a heterogeneous spatial distribution

of the a and b parameters of the rate-and-state friction model as employed in several simulations of faulting (Barbot et al., 2012). We note that such approaches are based on a continuum description of the interface and do not model the failure of individual asperities where locations in between are contact-free and hence have zero frictional strength like in our case.

Our results indicate that the strengthening phase, which could be seen as the preparatory phase of large ruptures, includes a population of events that are multi-scale in size (Gutenberg-Richter relation in Figure 14) and in duration (Figure 15). A similar multi-scale size distribution has also been reported by Nasuno et al. (1998) for the events that occurred during the strengthening phase along a sheared fault gouge layer simulated by spherical glass particles that are similar to our asperities. Such granular layers have also been numerically modeled by Aharonov and Sparks (2004), which evidenced a transition from weak to strong contacts accompanied by accelerating internal stress release of grains before large stick-slip events. It suggests that such a transition of localized contacts during the strengthening phase could be considered as a precursor for the impending large scale stick-slip. Combined with our results, it implies that the preparatory phase of large earthquakes is very long with many foreshocks strongly related to the quenched disorder. This result is highly reproducible with the same disorder in the asperity positions.

5.5 Limitations of the Experimental Setup

Our novel experimental setup builds a heterogeneous shear interface of multi-asperity contacts. An important point resulting from the designed configuration is that the elevated adhesion of the silicone block to the asperities is strong enough such that there is no rolling of asperities caused by the shearing imposed on the PMMA plate. Similarly, we also make sure that the silicone block is at no time in contact with the PMMA plate during the experiment. Indeed, in such a case, the high adhesion of the silicone would cause a local resistance to slip and modify the modeled physical process (from friction to adhesion). This limits the maximum normal load we can impose on the system to approximately 1500 N, at a higher imposed normal load, the silicone block starts to have some local contacts with the PMMA plate.

The sampling rate of the camera employed directly determines the time resolution for tracking the slips of asperities. Thus, the rapid slipping phase involving multiple asperities cannot be analyzed in detail. For example, it is not sampled with a high enough time resolution to capture a clear trend of the decay of the shear force as a function of slip during these episodes (see Figure 9). Furthermore, the precise timing, migration, or interactions of local bead slips during the high slipping phase is not accessible. Finally, as we evidence, the overall rupture during such SEs is slow but it does not preclude that locally during such slow transient, local dynamic rupture occurs such that some proportion of the resolved slip is actually taking place during such dynamic phase and radiate elastic wave. The proportion of the slip taking place on the asperities as dynamic events is presently not measurable but remains to be investigated for future studies.

The derivation of the moment, M_0 , of the slip events required the computation of an area, A_i , attached to each asperity (see Eq. 8). Here we take for each asperity the area returned by the Voronoi cell including the asperity. Such a definition of the slip area attached to an asperity probably over-estimate the real slipping area during an IAS. Indeed, the locked area of an asperity is presumably much lower than a circle of the asperity radius (considering a Hertz contact model) (K. L. Johnson, 1987). Although some slip deficit can extend beyond the fully locked area, it becomes negligible at a distance typically greater than one asperity radius (L. R. Johnson, 2010). It then leads to an over-estimation of the computed moment. However, as the contact area for each asperity should be nearly similar (considering again the Hertz contact model and the low stiffness of the silicone) we can expect that the conclusion of the magnitude distribution presented in Figure 14 would be unchanged if one could obtain a precise measurement of the slipping area of each IAS. We thus acknowledge that the reported moment of slip events should be mostly interpreted relatively than as absolute values. Such complexity of the slip distribution is also observed for natural earthquakes with zones of little or no slip (Freymueller et al., 2021).

Another ambiguity is involved in the calculation of the moment from equation (8). Indeed, the shear modulus used in this equation is taken as the shear modulus of the PMMA. However the PMMA is the dominant material only on one side of the system, the other side is composed of the PMMA beads embedded in the silicone block. Characterizing the shear modulus for such bi-material is not a trivial task and again further warns against a direct interpretation of the absolute values of M_0 .

6 Conclusions

This study analyzes the collective behavior of numerous discrete asperities ($N \approx 140$) modeled on an analog fault interface during multiple seismic cycles. We show that an interface composed of multiple discrete asperities can have a macroscopic behavior that is distinct from that of its individual elements. The asperities present a diversity of slips at various speeds. We evidence the dependency of the interseismic coupling of the interface with the topographical map of the asperity summits and the normal load imposed on the system. We notably show that topographic variations of the asperity summits have a pronounced effect on this coupling. The slip intermittency of the activity of clustered asperities indicates that the interface undergoes local episodes of creep that ultimately lead to the global slip of the interface. The analysis of the evolution of the elastic energy along the interface helps to track the disordering of the asperities with respect to their initial position. We show that this energy is typically higher for large normal stress, which supports the conclusion that normal stress maintains a larger disorder in the system. It shows as well that the disorder increases during the strengthening phase and is only partially reduced during large slip events. Significant statistical features of slip widely observed in natural faults are reproduced by our experiments like the Gutenberg–Richter law, Omori’s law, and the moment–duration scaling, suggesting that the obtained results can be extrapolated to natural fault systems.

Open Research

All data obtained in our experiments are available at <https://seafire.unistra.fr/d/807cc92c4a42474797c2/>.

Acknowledgments

We thank Alain Steyer for the technical support. We thank Satoshi Ide for the discussion. This work of the Interdisciplinary Thematic Institute GeoT, as part of the ITI 2021–2028 program of the University of Strasbourg, CNRS and Inserm, was supported by IdEx Unistra (ANR-10-IDEX- 0002), and by SFRI-STRAT’US project (ANR ANR-20-SFRI-001) under the framework of the French Investments for the Future Program. This work was also supported by the China Scholarship Council (CSC) grant 201906370056.

References

Aharonov, E., & Sparks, D. (2004). Stick-slip motion in simulated granular layers.

- 828 *Journal of Geophysical Research*, 109(B09306).
- 829 Albertini, G., Karrer, S., Grigoriu, M. D., & Kammer, D. S. (2021). Stochastic prop-
 830 erties of static friction. *Journal of the Mechanics and Physics of Solids*, 147,
 831 104242.
- 832 Aubry, J., Passelègue, F., Escartín, J., Gasc, J., Deldicque, D., & Schubnel, A.
 833 (2020). Fault stability across the seismogenic zone. *Journal of Geophysical*
 834 *Research: Solid Earth*, 125(8), e2020JB019670.
- 835 Barbot, S., Lapusta, N., & Avouac, J.-P. (2012). Under the hood of the earthquake
 836 machine: Toward predictive modeling of the seismic cycle. *Science*, 336(6082),
 837 707–710.
- 838 Baumberger, T., & Caroli, C. (2006). Solid friction from stick–slip down to pinning
 839 and aging. *Advances in Physics*, 55(3-4), 279–348.
- 840 Ben-David, O., Cohen, G., & Fineberg, J. (2010). The dynamics of the onset of fric-
 841 tional slip. *Science*, 330(6001), 211–214.
- 842 Ben-Zion, Y., & Sammis, C. G. (2003). Characterization of fault zones. *Pure and*
 843 *Applied Geophysics*, 160(3), 677–715.
- 844 Bhushan, B. (1998). Contact mechanics of rough surfaces in tribology: multiple as-
 845 perity contact. *Tribology Letters*, 4(1), 1–35.
- 846 Bürgmann, R., Kogan, M. G., Steblov, G. M., Hilley, G., Levin, V. E., & Apel, E.
 847 (2005). Interseismic coupling and asperity distribution along the Kamchatka
 848 subduction zone. *Journal of Geophysical Research*, 110(B07405).
- 849 Candela, T., Renard, F., Bouchon, M., Brouste, A., Marsan, D., Schmittbuhl, J.,
 850 & Voisin, C. (2009). Characterization of fault roughness at various scales:
 851 Implications of three-dimensional high resolution topography measurements.
 852 *Pure and Applied Geophysics*, 1817–1851.
- 853 Candela, T., Renard, F., Klinger, Y., Mair, K., Schmittbuhl, J., & Brodsky, E. E.
 854 (2012). Roughness of fault surfaces over nine decades of length scales. *Journal*
 855 *of Geophysical Research*, 117(B8), B08409.
- 856 Cattania, C., & Segall, P. (2021). Precursory slow slip and foreshocks on rough
 857 faults. *Journal of Geophysical Research: Solid Earth*, 126(4), e2020JB020430.
- 858 Chester, F. M., & Chester, J. S. (1998). Ultracataclasite structure and friction pro-
 859 cesses of the Punchbowl fault, San Andreas system, California. *Tectonophysics*,
 860 295(1-2), 199–221.

- 861 Chester, F. M., Evans, J. P., & Biegel, R. L. (1993). Internal structure and weak-
 862 ening mechanisms of the San Andreas fault. *Journal of Geophysical Research*,
 863 98(B1), 771–786.
- 864 Davies, E. R. (2005). *Machine vision: theory, algorithms, practicalities*. Elsevier.
- 865 de Geus, T. W., Popović, M., Ji, W., Rosso, A., & Wyart, M. (2019). How collec-
 866 tive asperity detachments nucleate slip at frictional interfaces. *Proceedings of*
 867 *the National Academy of Sciences*, 116(48), 23977–23983.
- 868 Dieterich, J. H. (1979). Modeling of rock friction: 1. experimental results and consti-
 869 tutive equations. *Journal of Geophysical Research*, 84(B5), 2161–2168.
- 870 Dieterich, J. H., & Kilgore, B. D. (1994). Direct observation of frictional contacts:
 871 New insights for state-dependent properties. *Pure and Applied Geophysics*,
 872 143(1), 283–302.
- 873 Dublanchet, P., Bernard, P., & Favreau, P. (2013). Interactions and triggering in
 874 a 3-D rate-and-state asperity model. *Journal of Geophysical Research: Solid*
 875 *Earth*, 118(5), 2225–2245.
- 876 Faulkner, D., Lewis, A., & Rutter, E. (2003). On the internal structure and mechan-
 877 ics of large strike-slip fault zones: field observations of the Carboneras fault in
 878 southeastern Spain. *Tectonophysics*, 367(3-4), 235–251.
- 879 Fisher, D. S., Dahmen, K., Ramanathan, S., & Ben-Zion, Y. (1997). Statistics of
 880 earthquakes in simple models of heterogeneous faults. *Physical Review Letters*,
 881 78(25), 4885.
- 882 Fortune, S. (1995). Voronoi diagrams and delaunay triangulations. *Computing in*
 883 *Euclidean Geometry*, 225–265.
- 884 Frank, W. B. (2016). Slow slip hidden in the noise: The intermittence of tectonic re-
 885 lease. *Geophysical Research Letters*, 43(19), 10–125.
- 886 Frank, W. B., & Brodsky, E. E. (2019). Daily measurement of slow slip from low-
 887 frequency earthquakes is consistent with ordinary earthquake scaling. *Science*
 888 *Advances*, 5(10), eaaw9386.
- 889 Freymueller, J. T., Suleimani, E. N., & Nicolsky, D. J. (2021). Constraints on the
 890 slip distribution of the 1938 mw 8.3 alaska peninsula earthquake from tsunami
 891 modeling. *Geophysical Research Letters*, 48(9), e2021GL092812.
- 892 Gan, G., Ma, C., & Wu, J. (2020). *Data clustering: theory, algorithms, and applica-*
 893 *tions*. SIAM.

- 894 Gao, H., Schmidt, D. A., & Weldon, R. J. (2012). Scaling relationships of source pa-
 895 rameters for slow slip events. *Bulletin of the Seismological Society of America*,
 896 *102*(1), 352–360.
- 897 Gent, A. N. (1958). On the relation between indentation hardness and Young’s mod-
 898 ulus. *Rubber Chemistry and Technology*, *31*(4), 896–906.
- 899 Goebel, T. H., Kwiitek, G., Becker, T. W., Brodsky, E. E., & Dresen, G. (2017).
 900 What allows seismic events to grow big?: Insights from b-value and fault
 901 roughness analysis in laboratory stick-slip experiments. *Geology*, *45*(9), 815–
 902 818.
- 903 Gutenberg, B., & Richter, C. F. (1944). Frequency of earthquakes in California. *Bul-*
 904 *letin of the Seismological Society of America*, *34*(4), 185–188.
- 905 Gvirtzman, S., & Fineberg, J. (2021). Nucleation fronts ignite the interface rupture
 906 that initiates frictional motion. *Nature Physics*, *17*(9), 1037–1042.
- 907 Hanks, T. C., & Kanamori, H. (1979). A moment magnitude scale. *Journal of Geo-*
 908 *physical Research*, *84*(B5), 2348–2350.
- 909 Harbord, C. W., Nielsen, S. B., De Paola, N., & Holdsworth, R. E. (2017). Earth-
 910 quake nucleation on rough faults. *Geology*, *45*(10), 931–934.
- 911 Hyndman, R. D., Yamano, M., & Oleskevich, D. A. (1997). The seismogenic zone of
 912 subduction thrust faults. *Island Arc*, *6*(3), 244–260.
- 913 Ide, S. (2010). Striations, duration, migration and tidal response in deep tremor.
 914 *Nature*, *466*(7304), 356–359.
- 915 Ide, S., Beroza, G. C., Shelly, D. R., & Uchide, T. (2007). A scaling law for slow
 916 earthquakes. *Nature*, *447*(7140), 76–79.
- 917 Jestin, C., Lengliné, O., & Schmittbuhl, J. (2019). Energy partitioning during sub-
 918 critical mode i crack propagation through a heterogeneous interface. *Journal of*
 919 *Geophysical Research: Solid Earth*, *124*(1), 837–855.
- 920 Johnson, K. L. (1987). *Contact mechanics*. Cambridge university press.
- 921 Johnson, L. R. (2010). An earthquake model with interacting asperities. *Geophysical*
 922 *Journal International*, *182*(3), 1339–1373.
- 923 Jolivet, R., Candela, T., Lasserre, C., Renard, F., Klinger, Y., & Doin, M.-P. (2015).
 924 The Burst-Like Behavior of Aseismic Slip on a Rough Fault: The Creeping
 925 Section of the Haiyuan Fault, China. *Bulletin of the Seismological Society of*
 926 *America*, *105*(1), 480–488.

- 927 Jolivet, R., Lasserre, C., Doin, M.-P., Peltzer, G., Avouac, J.-P., Sun, J., & Dailu,
 928 R. (2013). Spatio-temporal evolution of aseismic slip along the Haiyuan fault,
 929 China: Implications for fault frictional properties. *Earth and Planetary Science*
 930 *Letters*, *377*, 23–33.
- 931 Kammer, D. S., Radiguet, M., Ampuero, J.-P., & Molinari, J.-F. (2015). Linear elas-
 932 tic fracture mechanics predicts the propagation distance of frictional slip. *Tri-*
 933 *bology Letters*, *57*(3), 1–10.
- 934 Kanamori, H., & Anderson, D. L. (1975). Theoretical basis of some empirical re-
 935 lations in seismology. *Bulletin of the Seismological Society of America*, *65*(5),
 936 1073–1095.
- 937 Khoshmanesh, M., & Shirzaei, M. (2018). Multiscale dynamics of aseismic slip on
 938 central san andreas fault. *Geophysical Research Letters*, *45*(5), 2274–2282.
- 939 Lay, T., & Kanamori, H. (1981). An asperity model of large earthquake sequences.
 940 *Earthquake Prediction: An International Review*, *4*, 579–592.
- 941 Lay, T., Kanamori, H., & Ruff, L. (1982). The asperity model and the nature of
 942 large subduction zone earthquakes. *Earthquake Prediction Research*, *1*, 3–71.
- 943 Lee, D.-T., & Schachter, B. J. (1980). Two algorithms for constructing a delaun-
 944 nay triangulation. *International Journal of Computer & Information Sciences*,
 945 *9*(3), 219–242.
- 946 Leeman, J., Saffer, D., Scuderi, M., & Marone, C. (2016). Laboratory observa-
 947 tions of slow earthquakes and the spectrum of tectonic fault slip modes. *Nature*
 948 *Communications*, *7*(1), 1–6.
- 949 Lengliné, O., Elkhoury, J., Daniel, G., Schmittbuhl, J., Toussaint, R., Ampuero,
 950 J.-P., & Bouchon, M. (2012). Interplay of seismic and aseismic deformations
 951 during earthquake swarms: An experimental approach. *Earth and Planetary*
 952 *Science Letters*, *331*, 215–223.
- 953 Lengliné, O., Frank, W. B., Marsan, D., & Ampuero, J.-P. (2017). Imbricated slip
 954 rate processes during slow slip transients imaged by low-frequency earthquakes.
 955 *Earth and Planetary Science Letters*, *476*, 122–131.
- 956 Li, T., & Rubin, A. M. (2017). A microscopic model of rate and state friction evolu-
 957 tion. *Journal of Geophysical Research: Solid Earth*, *122*(8), 6431–6453.
- 958 Luo, Y., & Ampuero, J.-P. (2018). Stability of faults with heterogeneous friction
 959 properties and effective normal stress. *Tectonophysics*, *733*, 257–272.

- 960 Marone, C. (1998). Laboratory-derived friction laws and their application to seismic
961 faulting. *Annual Review of Earth and Planetary Sciences*, 26(1), 643–696.
- 962 McLaskey, G. C., & Glaser, S. D. (2011). Micromechanics of asperity rupture dur-
963 ing laboratory stick slip experiments. *Geophysical Research Letters*, 38(12),
964 L12302.
- 965 McLaskey, G. C., Thomas, A. M., Glaser, S. D., & Nadeau, R. M. (2012). Fault
966 healing promotes high-frequency earthquakes in laboratory experiments and on
967 natural faults. *Nature*, 491, 101–104.
- 968 Mitchell, T., & Faulkner, D. (2009). The nature and origin of off-fault damage
969 surrounding strike-slip fault zones with a wide range of displacements: A field
970 study from the Atacama fault system, northern Chile. *Journal of Structural
971 Geology*, 31(8), 802–816.
- 972 Morad, D., Sagy, A., Tal, Y., & Hatzor, Y. H. (2022). Fault roughness controls slid-
973 ing instability. *Earth and Planetary Science Letters*, 579, 117365.
- 974 Moreno, M. S., Bolte, J., Klotz, J., & Melnick, D. (2009). Impact of megathrust
975 geometry on inversion of coseismic slip from geodetic data: Application to the
976 1960 Chile earthquake. *Geophysical Research Letters*, 36(L16310).
- 977 Nadeau, R. M., & Johnson, L. R. (1998). Seismological studies at Parkfield VI:
978 Moment release rates and estimates of source parameters for small repeating
979 earthquakes. *Bulletin of the Seismological Society of America*, 88(3), 790–814.
- 980 Nasuno, S., Kudrolli, A., Bak, A., & Gollub, J. P. (1998). Time-resolved studies of
981 stick-slip friction in sheared granular layers. *Physical Review E*, 58(2), 2161–
982 2171.
- 983 Perfettini, H., Avouac, J.-P., Tavera, H., Kositsky, A., Nocquet, J.-M., Bondoux, F.,
984 ... others (2010). Seismic and aseismic slip on the Central Peru megathrust.
985 *Nature*, 465(7294), 78–81.
- 986 Pohrt, R., & Popov, V. L. (2012). Normal contact stiffness of elastic solids with frac-
987 tal rough surfaces. *Physical Review Letters*, 108(10), 104301.
- 988 Power, W., Tullis, T., Brown, S., Boitnott, G., & Scholz, C. (1987). Roughness of
989 natural fault surfaces. *Geophysical Research Letters*, 14(1), 29–32.
- 990 Romanet, P., Bhat, H. S., Jolivet, R., & Madariaga, R. (2018). Fast and slow slip
991 events emerge due to fault geometrical complexity. *Geophysical Research Let-
992 ters*, 45(10), 4809–4819.

- 993 Rousset, B., Jolivet, R., Simons, M., Lasserre, C., Riel, B., Milillo, P., ... Renard,
 994 F. (2016). An aseismic slip transient on the north anatolian fault. *Geophysical*
 995 *Research Letters*, *43*(7), 3254–3262.
- 996 Ruff, L., & Kanamori, H. (1983). The rupture process and asperity distribution
 997 of three great earthquakes from long-period diffracted P-waves. *Physics of the*
 998 *Earth and Planetary Interiors*, *31*(3), 202–230.
- 999 Ruina, A. (1983). Slip instability and state variable friction laws. *Journal of Geo-*
 1000 *physical Research*, *88*(B12), 10359–10370.
- 1001 Schmittbuhl, J., Chambon, G., Hansen, A., & Bouchon, M. (2006). Are stress dis-
 1002 tributions along faults the signature of asperity squeeze? *Geophysical Research*
 1003 *Letters*, *33*(13).
- 1004 Schmittbuhl, J., Gentier, S., & Roux, S. (1993). Field measurements of the rough-
 1005 ness of fault surfaces. *Geophysical Research Letters*, *20*(8), 639–641.
- 1006 Schmittbuhl, J., & Måløy, K. J. (1997). Direct observation of a self-affine crack
 1007 propagation. *Physical Review Letters*, *78*(20), 3888–3891.
- 1008 Schmittbuhl, J., Schmitt, F., & Scholz, C. (1995). Scaling invariance of crack sur-
 1009 faces. *Journal of Geophysical Research*, *100*(B4), 5953–5973.
- 1010 Schmittbuhl, J., Vilotte, J.-P., & Roux, S. (1996). A dissipation-based analysis of
 1011 an earthquake fault model. *Journal of Geophysical Research*, *101*(B12), 27741–
 1012 27764.
- 1013 Scholz, C. (2019). *The mechanics of earthquakes and faulting*. Cambridge University
 1014 Press.
- 1015 Scholz, C., & Campos, J. (1995). On the mechanism of seismic decoupling and back
 1016 arc spreading at subduction zones. *Journal of Geophysical Research*, *100*(B11),
 1017 22103–22115.
- 1018 Scholz, C., & Campos, J. (2012). The seismic coupling of subduction zones revisited.
 1019 *Journal of Geophysical Research*, *117*(B05310).
- 1020 Schulz, S. E., & Evans, J. P. (2000). Mesoscopic structure of the Punchbowl Fault,
 1021 Southern California and the geologic and geophysical structure of active strike-
 1022 slip faults. *Journal of Structural Geology*, *22*(7), 913–930.
- 1023 Selvadurai, P. A., & Glaser, S. D. (2015). Laboratory-developed contact models con-
 1024 trolling instability on frictional faults. *Journal of Geophysical Research: Solid*
 1025 *Earth*, *120*(6), 4208–4236.

- 1026 Selvadurai, P. A., & Glaser, S. D. (2017). Asperity generation and its relationship to
 1027 seismicity on a planar fault: A laboratory simulation. *Geophysical Journal In-*
 1028 *ternational*, 208(2), 1009–1025.
- 1029 Stierman, D. J. (1984). Geophysical and geological evidence for fracturing, water cir-
 1030 culation and chemical alteration in granitic rocks adjacent to major strike-slip
 1031 faults. *Journal of Geophysical Research*, 89(B7), 5849–5857.
- 1032 Subarya, C., Chlieh, M., Prawirodirdjo, L., Avouac, J.-P., Bock, Y., Sieh, K., ...
 1033 McCaffrey, R. (2006). Plate-boundary deformation associated with the great
 1034 Sumatra–Andaman earthquake. *Nature*, 440(7080), 46–51.
- 1035 Sutton, M. A., Orteu, J. J., & Schreier, H. (2009). *Image correlation for shape, mo-*
 1036 *tion and deformation measurements: basic concepts, theory and applications*.
 1037 Springer Science & Business Media.
- 1038 Tanguy, A., Gounelle, M., & Roux, S. (1998). From individual to collective pinning:
 1039 Effect of long-range elastic interactions. *Physical Review E*, 58(2), 1577.
- 1040 Utsu, T., Ogata, Y., & S. Matsu’ura, R. (1995). The centenary of the Omori formula
 1041 for a decay law of aftershock activity. *Journal of Physics of the Earth*, 43(1),
 1042 1–33.
- 1043 Wu, B. S., & McLaskey, G. C. (2019). Contained laboratory earthquakes rang-
 1044 ing from slow to fast. *Journal of Geophysical Research: Solid Earth*, 124(10),
 1045 10270–10291.
- 1046 Yuen, H., Princen, J., Illingworth, J., & Kittler, J. (1990). Comparative study of
 1047 hough transform methods for circle finding. *Image and Vision Computing*,
 1048 8(1), 71–77.
- 1049 Zhou, X., He, Y., & Shou, Y. (2021). Experimental investigation of the effects of
 1050 loading rate, contact roughness, and normal stress on the stick-slip behavior of
 1051 faults. *Tectonophysics*, 816, 229027.

Supporting Information for ”Collective behavior of asperities before large stick-slip events”

Weiwei Shu¹, Olivier Lengliné¹, Jean Schmittbuhl¹

¹EOST/ITES, Université de Strasbourg/CNRS, France

Contents of this file

1. Figures S1
2. Tables S1 to S2

Corresponding author: W. Shu, EOST/ITES, Université de Strasbourg/CNRS, Strasbourg, 67084, France. (w.shu@unistra.fr)

March 8, 2023, 9:33pm

Figure S1. Natural earthquakes usually show the characteristic of the cluster of seismicity which actually implies that the isolated events are uncommon. In our experiments, we consider the percentage of isolated slip episodes as a function of different values of the coefficient of D_i^{med} . We find the percentage first decreases sharply and then keeps relatively constant. We, therefore, determine the value of 6 which controls the transition as the optimal coefficient of D_i^{med} .

Table S1. Details of the parameters for each experiment are listed in Table S1.

Table S2. We list the b value of each experiment with a specific normal load and displacement rate in Table S2. It shows that the b value has no clear dependence on the loading rate of the system. In addition, our experimental results show that the b value is insensitive as well to the imposed normal load.

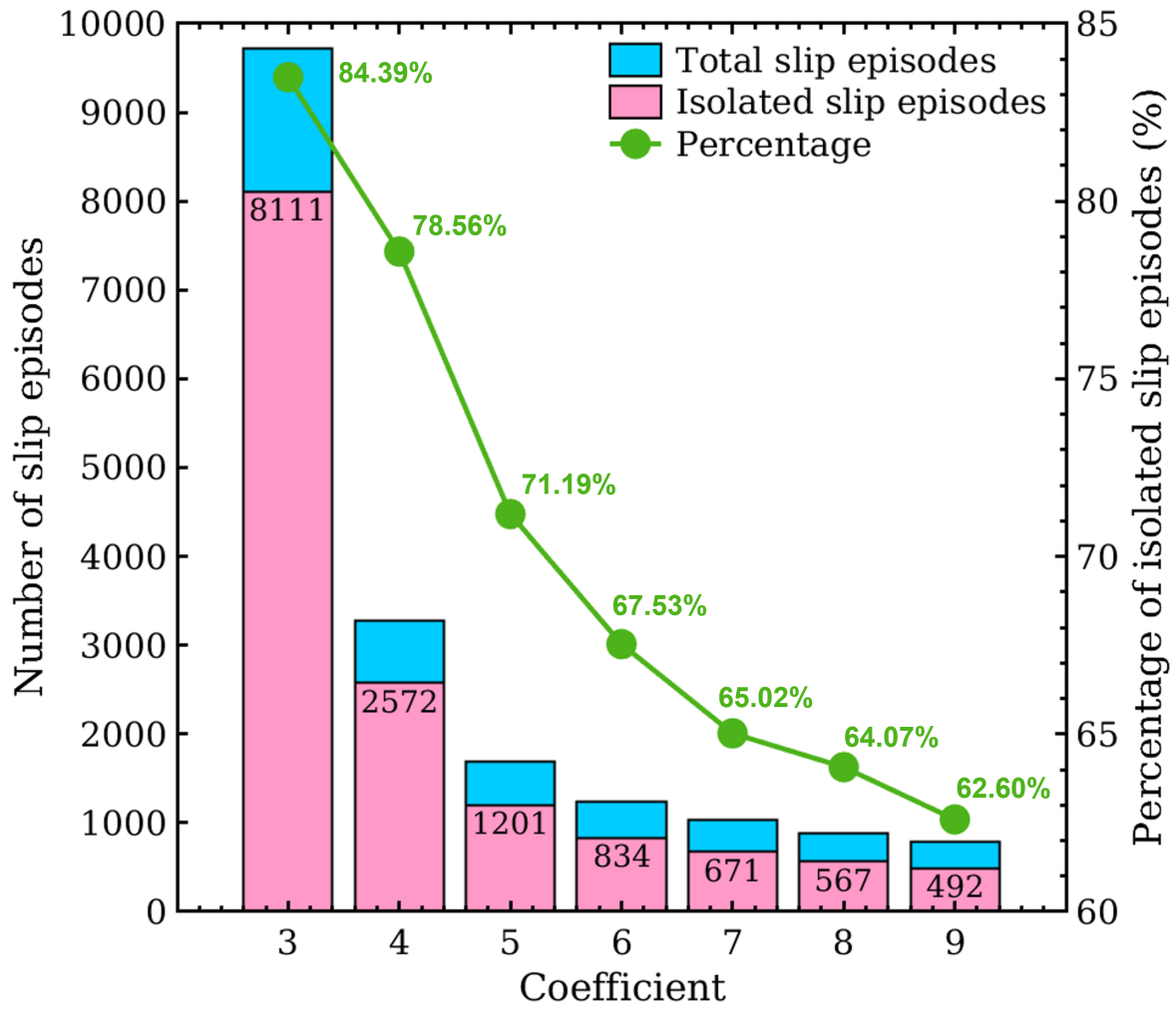


Figure S1. Quantitative comparison for determining the optimal value of the coefficient of D_i^{med} . With the increase of the value of the coefficient, the percentage of isolated slip episodes first decreases sharply and then keeps relatively stable. The value of 6 that controls the transition is determined as the optimal coefficient of D_i^{med} .

Table S1. Parameters of each experiment

Normal load (N)	Displacement rate ($\mu\text{m/s}$)		
	5.0	10.0	15.0
10	Exp.26		
25	Exp.25		
50	Exp.24		
100	Exp.6	Exp.7	Exp.8, Exp.27, Exp.28
200	Exp.1, Exp.9	Exp.10	Exp.11
400	Exp.2, Exp.12	Exp.13	Exp.14
600	Exp.15	Exp.3, Exp.16	Exp.17
700	Exp.18	Exp.19	Exp.20
800	Exp.21	Exp.4, Exp.22	Exp.23
1000			Exp.5

Table S2. Parameters and b value of each experiment

Experiment	Normal load (N)	Displacement rate ($\mu\text{m/s}$)	b value
1	200	5.0	1.08 ± 0.13
2	400	5.0	1.22 ± 0.08
3	600	10.0	1.16 ± 0.11
4	800	10.0	1.17 ± 0.13
5	1000	15.0	1.05 ± 0.14
6	100	5.0	1.25 ± 0.11
7	100	10.0	1.28 ± 0.11
8	100	15.0	1.08 ± 0.08
9	200	5.0	1.35 ± 0.11
10	200	10.0	1.49 ± 0.15
11	200	15.0	1.40 ± 0.15
12	400	5.0	1.21 ± 0.05
13	400	10.0	1.44 ± 0.10
14	400	15.0	1.35 ± 0.12
15	600	5.0	1.28 ± 0.12
16	600	10.0	1.19 ± 0.09
17	600	15.0	1.29 ± 0.10
18	700	5.0	1.17 ± 0.10
19	700	10.0	1.17 ± 0.10
20	700	15.0	1.45 ± 0.07
21	800	5.0	1.18 ± 0.15
22	800	10.0	1.13 ± 0.10
23	800	15.0	1.88 ± 0.16
24	50	5.0	1.58 ± 0.10
25	25	5.0	1.60 ± 0.09
26	10	5.0	2.04 ± 0.09
27	100	15.0	1.30 ± 0.08
28	100	15.0	1.11 ± 0.05